Design and fabrication of state of the art uncooled thermopile infrared detectors with cavity coupled absorption

A DISSERTATION
SUBMITTED TO THE FACULTY OF THE GRADUATE SCHOOL
OF THE UNIVERSITY OF MINNESOTA

by

Ryan P Shea

IN PARTIAL FULFILLMENT OF THE REQUIREMENTS
FOR THE DEGREE OF
DOCTOR OF PHILOSOPHY

Dr. Joseph Talghader, Adviser

June 2013

©Ryan P Shea 2013
ALL RIGHTS RESERVED

Acknowledgements

I would first and foremost like to acknowledge the guidance of my research adviser Joseph Talghader. Secondly I would like to acknowledge my research partner Anand Gawarikar. I must also acknowledge the assistance of the other members of the Optical MEMS research group past and present: Jan Makowski, Nick Gabriel, Sangho Kim, Phil Armstrong, Merlin Mah, Wing Chan, Luke Taylor, Kyle Olson,and Andrew Brown. I would also like to acknowledge the staff of the University of Minnesota Nanofabrication Center and Characterization Facility especially Tony Whipple and Mark Fisher.

Dedicated to my wife and my mother.

UNIVERSITY OF MINNESOTA

Abstract

Dr. Joseph Talghader, Adviser
Department of Electrical Engineering

Doctor of Philosophy

by Ryan P Shea

We present the design, fabrication, and characterization of uncooled thermopile infrared detectors with cavity coupled absorption in the long wave infrared with performance exceeding all published works. These detectors consist of a two die optical cavity which enhances absorption in the desired spectral range while rejecting unwanted noise off resonance. The electrical transduction mechanism is a thermopile consisting of four thermoelectric junctions of co-sputtered Bi_2Te_3 and Sb_2Te_3 having a room temperature unitless thermoelectric figure of merit of .43. Processing steps are described in detail for the fabrication of extremely thermally isolated structures necessary for highly sensitive detectors. Optical characterization of the devices reveals a responsivity of 4700 V/W, thermal time constant of 58 ms, and specific detectivity of at least 3.0x10^9 cm$\sqrt{Hz}$/W. Also presented are a theoretical proposal for a midwave infrared detector using semiconductor selective absorption to enhance detectivity beyond the blackbody radiation limit and a new method for the analysis of radiation thermal conduction in highly thermally isolated structures.

Contents

Acknowledgements **i**

Abstract **iii**

List of Figures **vii**

List of Tables **x**

Physical Constants **xi**

Symbols **xii**

Declaration of Authorship **xiv**

1 Introduction **1**
- 1.1 Introduction . . . 1
- 1.2 State of the Art . . . 4
- 1.3 Organization of Chapters . . . 5

2 Inroduction to Thermoelectrics **7**
- 2.1 Introduction . . . 7
- 2.2 The Seebeck Effect . . . 7
  - 2.2.1 Seebeck Coefficient . . . 8
- 2.3 Thermoelectric Cooling . . . 9
- 2.4 Thermoelectric Materials . . . 11
- 2.5 Selection of Thermoelectric Materials . . . 13
- 2.6 Engineering of Thermoelectric Materials . . . 14
- 2.7 Thermoelectric Materials for MEMS Devices . . . 15

3 Thermal Detector Background and Design **17**
- 3.1 Introduction . . . 17
- 3.2 Detector Response . . . 17
- 3.3 Noise in Thermal Infrared Detectors . . . 18
- 3.4 Detectivity . . . 19
- 3.5 Radiation Thermal Conductance Noise . . . 19

3.6 Device Design . . . 21
3.7 Device Layout . . . 21
3.8 Device Simulation . . . 23
3.9 Optical Design . . . 23
3.10 Device Simulation Continued . . . 25
3.11 Conclusion . . . 26

4 MWIR Detection Using Semiconductor Spectrally Selective Absorption 27
4.1 Introduction . . . 27
4.2 Theory . . . 28
4.3 Optical Simulation . . . 30
4.4 Practical Device Design . . . 31
4.5 Spectral Selectivity using Plasmonic Structures . . . 34

5 Analysis of radiation thermal conductance in microstructures. 36
5.1 Introduction . . . 36
5.2 Background . . . 37
5.3 Fabrication . . . 39
5.4 Experiment . . . 41
5.5 Conclusion . . . 46

6 Detector Fabrication 47
6.1 Introduction . . . 47
6.2 Standard Processes . . . 47
6.2.1 Solvent Clean . . . 47
6.2.2 1805 Lithography . . . 48
6.2.3 1813 Lithography . . . 48
6.2.4 Lift Off Lithography . . . 48
6.3 Detector Fabrication . . . 49
6.3.1 Electrical Insulation . . . 49
6.3.2 Aluminum Oxide Structural Layer . . . 50
6.3.3 Optical Film Deposition . . . 50
6.3.3.1 Ge damage from solvents . . . 51
6.3.3.2 Material Overhang . . . 52
6.3.4 Encapsulation . . . 52
6.3.5 Interconnect Layer . . . 53
6.3.6 Bond Pad and Wire Layer . . . 54
6.3.7 Thermoelectric Film Deposition . . . 55
6.3.7.1 Thermoelectric Material Overhang . . . 57
6.3.8 Encapsulation . . . 58
6.3.9 Backside Hard Mask Deposition . . . 58
6.3.10 BCl_3 Plasma Etch . . . 59
6.3.11 Backside Hard Mask Patterning . . . 60
6.3.12 Etch Release . . . 61
6.4 Micropillar Fabrication . . . 62
6.4.1 SOI Fabrication . . . 62

6.4.2 Pillar etching . . . 63
6.4.3 Micromirror Deposition . . . 63
6.5 Microaperature Fabrication . . . 64
6.6 Device Assembly . . . 64

7 Characterization 67
7.1 Introduction . . . 67
7.2 Thermoelectric Characterization . . . 67
7.2.1 Temperature Coefficient of Resistance . . . 67
7.2.2 Film Composition . . . 69
7.2.3 Carrier Concentration . . . 70
7.2.4 Intrinsic Stress . . . 71
7.2.5 Resistivity . . . 73
7.2.6 Contact Resistance . . . 74
7.2.7 Seebeck Coefficient . . . 74
7.3 Thermal Conductivity . . . 77
7.3.1 Figure of Merit . . . 77
7.4 Device Characterization . . . 78
7.4.1 Micropillar Reflectance . . . 78
7.4.2 Cavity Spacing . . . 79
7.4.3 Thermal Conductance . . . 79
7.4.4 Responsivity . . . 81
7.4.5 Thermal Time Constant . . . 84
7.4.6 Noise Measurement . . . 85
7.4.7 Detectivity . . . 86
7.5 Conclusion . . . 86

8 Conclusion and Future Work 89
8.1 Summary of Results . . . 89
8.2 Future Work . . . 91
8.2.1 Al_2O_3 Thickness . . . 91
8.2.2 Thermoelectric Film Thickness . . . 91
8.2.3 Thermoelectric Film Performance . . . 92
8.2.4 Three Die Cavity Coupling . . . 92
8.2.5 MWIR Spectrally Selective Absorption . . . 93
8.2.6 Optimized Design . . . 95

Bibliography 97

List of Figures

1.1 Spectral radiance of a 300K blackbody. 2
1.2 Simulated atmospheric infrared transmission spectrum. 2

2.1 Schematic of a semiconductor demonstrating the Seebeck effect. 8
2.2 Band structure of an n-type semicondcuctor under thermal equalibrium. . 9
2.3 Band structure of an n-type semicondcutor with applied temperature difference. 9
2.4 Layout of a generic thermoelectric junction. 9
2.5 Seebeck coefficient vs carrier concentration. 12
2.6 Electrical conductivity vs carrier concentration. 12
2.7 Thermoelectric power factor vs carrier concentration. 13
2.8 Thermoelectric figure of merit for all temperatures. 14

3.1 Mask layout of the '1B' device design. 22
3.2 Cross section of the thermoelectric leg of the '1B' device design. 22
3.3 Cross sectional schematic of the optical device design. 24
3.4 Simulated absorption spectrum of the optical device design. 24

4.1 Detectivity vs cutoff wavelength for a generic semiconductor infrared detector. 30
4.2 Absorption and radiation limited detectivity for a single 500nm thick layer of PbSe. 31
4.3 Absorption and radiation limited detectivity for the cavity coupled detector. 32
4.4 Detectivity vs wavelength of for the high detectivity and low thermal time constant device designs. 33
4.5 Absorption vs wavelength and structural layout for plasmonic selective absorption. 35

5.1 Simulation of temperature response to input power of a generic thermal isolation structure with varying thermal conductance source. 39
5.2 Simulation of thermal conductance vs input power of a generic thermal isolation structure with varying thermal conductance source. 40
5.3 Concept image of fabricated microcoolers showing film layout and materials used. 41
5.4 SEM micrograph of a released microcooler. 41
5.5 SEM micrographs of the two cooler geometries. 42
5.6 Input power vs temperature change data and fit for released microcoolers. 43
5.7 Thermal conductance vs temperature change contribution of each thermal conductance source. 44

5.8 Temperature change vs input power of microcoolers. 44
5.9 Microscope image of a radiation limited microcooler. 45
5.10 Input power vs temperature change data with purely fourth order fit. . . 45

6.1 Model including SiN_x layer. 50
6.2 Microscope image of a solvent damaged optical stack. 50
6.3 Microscope image and model of fabrication after optical stack deposition . 51
6.4 Microscope image of a solvent damaged optical stack. 52
6.5 Microscope image of the optical stack showing material overhang issues. . 52
6.6 Diagram of interconnect configurations 54
6.7 Microscope image and model of fabrication after Ti/Pt interconnect deposition. 54
6.8 Microscope image and model of fabrication after Cr/Au bond pad deposition. 55
6.9 Microscope image and model of fabrication after thermoelectric film deposition. 57
6.10 SEM image of thermoelectric film overhang 58
6.11 Image of hard mask breakdown during etch release. 59
6.12 Image of the typical effects of resist burn-on 59
6.13 Microscope image and model of fabrication after BCl_3 plasma etching. . . 60
6.14 Microscope image of thermoelectric films showing significant thermal damage. 61
6.15 Image of unknown particulates formed by releasing with SF_6. 61
6.16 SEM image and model of etch released detector. 62
6.17 Model images of micropillar fabrication flow. 63
6.18 SEM image of released and coated micropillars. 64
6.19 Image of micropillar model after etch and optical coating. 64
6.20 Model images of microaperture fabrication flow. 65
6.21 Model image of device assembly. 65
6.22 SEM images of micromirror and detector assembled into an optical cavity. 66
6.23 Confocal microscope image of device through aperture. 66
6.24 Optical microscope image of packaged die. 66

7.1 Image of the TCR measurement setup. 68
7.2 TCR data for three different measurement configurations. 69
7.3 Thermoelectric figure of merit vs Te composition plot for Bi_2Te_3. 69
7.4 EDS spectrum of Bi_2Te_3. 70
7.5 EDS spectrum of Sb_2Te_3. 71
7.6 Thermoelectric figure of merit vs carrier concentration plot for Sb_2Te_3. . . 72
7.7 Hall effect test structure for carrier concentration measurements. 72
7.8 Hall voltage vs magnetic field data. 73
7.9 Test structure for resistivity measurements. 74
7.10 Test structure for contact resistance measurements. 75
7.11 Contact resistance data for both materials. 75
7.12 Microscope image of Seebeck coefficient test structure 76
7.13 Seebeck voltage vs temperature change data for both materials 76
7.14 SEM images of the thermal conductivity test structures. 78
7.15 Micromirror reflectance spectrum measured with FTIR microscope. 79

7.16 Measured and simulated reflectance spectrum of a low order optical cavity. 80
7.17 Layer thickness and refractive index for cavity spacing simulation. 80
7.18 Electrical responsivity vs input power for a thermopile detector. 81
7.19 Thermal conductance vs input power for a thermopile detector. 81
7.20 Schematic of the measurement setup for responsivity measurements. . . . 82
7.21 SEM micrograph of 150μm device over large pillar. 83
7.22 Responsivity spectrum of 150μm device over large pillar. 83
7.23 Optical microscope image of 100μm device over 200μm pillar. 84
7.24 Responsivity spectrum of 100μm device over 200μm pillar. 84
7.25 Confocal microscope image of the 1B device through a 200μm microaperture. 84
7.26 Responsivity spectrum of the 1B device through a 200μm microaperture. 84
7.27 Thermal time constant measurement and fit. 85
7.28 Noise power spectral density and fit of 1B geometry device. 86
7.29 Detectivity spectrum of 150μm device over large pillar. 87
7.30 Detectivity spectrum of 100μm device over 200μm pillar. 87
7.31 Detectivity spectrum of the 1B device through a 200μm microaperture. . 87

8.1 Model of the three die configuration of the narrowband device. 93
8.2 Simulated absorption spectrum of the narrowband device. 94
8.3 Simulated absorption spectrum of the MWIR spectrally selective device. . 95

List of Tables

3.1 Device design parameters and calculated device resistance and film thermal conductance for two design scenarios. 23
3.2 Layer structure for the simulated optical device design. 25
3.3 Material constants and calculated device parameters. 26

4.1 Optical design parameters of an example device 32
4.2 Device design parameters, calculated thermal properties, and calculated noise levels for two example devices 34

7.1 Comparison of design parameters and actual results. 88

8.1 Layer structure for simulated narrowband device design. 93
8.2 Layer structure for simulated MWIR spectrally selective device design. . . 94
8.3 Design parameters for optimized device design. 96

Physical Constants

Planck's Constant	h	$=$	6.626×10^{-34} Js
Boltzmann Constant	k_b	$=$	1.381×10^{-23} J/K
Speed of Light	c	$=$	2.998×10^{8} m/s
Electron Charge	e	$=$	1.602×10^{-19} C
Lorentz Number	L_N	$=$	2.44×10^{-8} WΩ K^{-2}
Stefan-Boltzmann Constant	σ_b	$=$	5.670×10^{-8} Js^{-1}m^{-2}K^{-4}

Symbols

T	temperature	K
B_R	spectral radiant emittance	W/m^2-μm
S	Seebeck coefficient	V/K
N_c	density of states of carriers	cm^{-3}
n	carrier concentration	cm^{-3}
r	scattering parameter	none
I	current	A
A	area	m^2
L	length	m
Q	thermal power	W
G	thermal conductance	W/K
R	resistance	Ω
C	thermal capacity	J/K
P	power	W
t	thickness	m
w	width	m
V	voltage	V
N	number of thermocouples	none
$\Re$	responsivity	V/W
NEP	noise equivalent power	W
f	frequency	Hz
k_m	1/f noise parameter	none
D^*	detectivity	cm$\sqrt{Hz}$/W
n_p	number of photons	none
N_p	density of states of photons	Hz^2*s^3/m^3
B	magnetic field	T
E	Young's modulus	Pa
v	Poison's ratio	none
l	cavity spacing	m

λ	wavelength	m
κ	thermal conductivity	W/m-K
ρ	electrical resistivity	Ω-m
ϵ	emissivity	none
σ	electrical resistivity	Ω-m
η	absorption coefficient	none
ω	angular frequency	rad/s
τ	thermal time constant	s
ν	frequency	Hz
θ	tangential angle	radians
Φ	azimuthal angle	radians
α	temperature coefficient of resistivity	K^{-1}
Γ	radius	m

Declaration of Authorship

I, Ryan P Shea, declare that this thesis titled, 'Design and fabrication of state of the art uncooled thermopile infrared detectors with cavity coupled absorption.' and the work presented in it are my own. I confirm that:

- This work was done wholly or mainly while in candidature for a research degree at this University.
- Where any part of this thesis has previously been submitted for a degree or any other qualification at this University or any other institution, this has been clearly stated.
- Where I have consulted the published work of others, this is always clearly attributed.
- Where I have quoted from the work of others, the source is always given. With the exception of such quotations, this thesis is entirely my own work.
- I have acknowledged all main sources of help.
- Where the thesis is based on work done by myself jointly with others, I have made clear exactly what was done by others and what I have contributed myself.

Signed: _____________________________________

Date: _____________________________________

Chapter 1

Introduction

1.1 Introduction

All forms of matter emit and absorb infrared radiation according to Planck's law, and the radiated power emitted by a unit area within a spectral interval, $d\lambda$, in W/m^2-μm^2 is given in Equation 1.1,

$$B_R(\lambda, T) = \frac{2\pi hc^2}{\lambda^5} \frac{1}{e^{\frac{hc}{\lambda k_b T}} - 1} d\lambda \tag{1.1}$$

where $B_R(\lambda, T)$ spectral radiant emittance, h is Planck's constant, c is the speed of light, λ is the wavelength, k_b is the Boltzmann constant, and T is the absolute temperature. Since a majority of the matter on the earth's surface is near room temperature we simulate the radiance of a blackbody at 300K in Figure 1.1. Here we see that the peak spectral radiance of a 300K blackbody occurs within the 8-12μm range, the long wave infrared (LWIR). The LWIR also happens to be an atmospheric transmission window. Common molecules in the atmosphere, O_2, N_2, CO_2, and water vapor do not absorb significantly in the LWIR. Using spectral data from the HITRAN database [1] we simulate the transmission spectrum of the atmosphere at 1 atm as shown in Figure 1.2. Here we atmospheric transmission windows in the LWIR as well as the midwave infrared (MWIR), 5-8μm.

There are many reasons one would wish to detect infrared radiation. The most obvious is thermal imaging, a technology which has applications such as night vision, passive guidance, and industrial process controll. Infrared detectors are also used to study incoming cosmic radiation for astronomy studies [2, 3]. The application we are most focused on in this study is infrared spectroscopy, specifically long range infrared

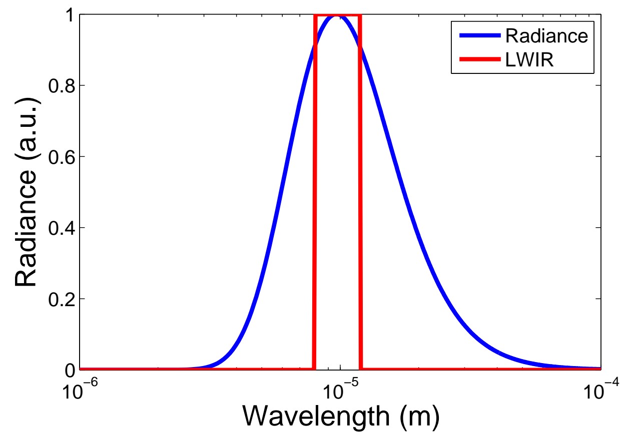

FIGURE 1.1: Spectral radiance of a 300K blackbody (blue) with the LWIR highlighted (red)

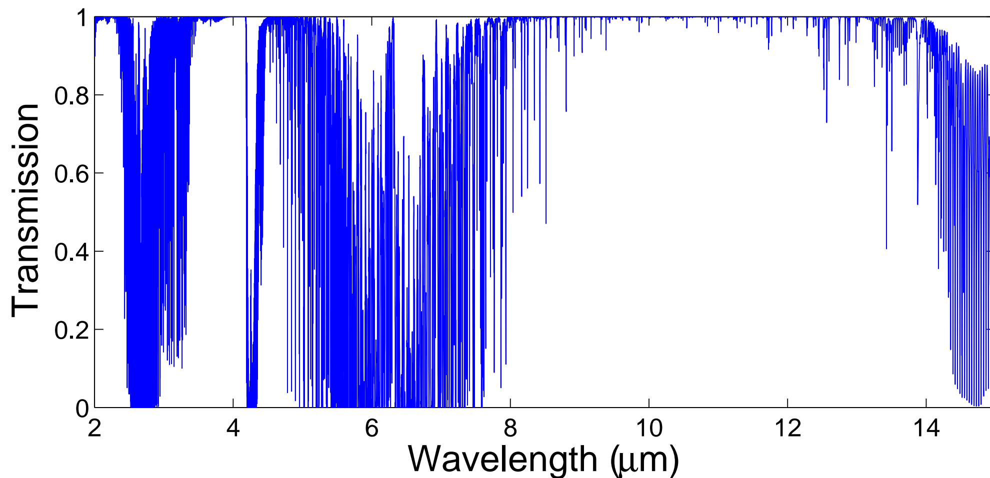

FIGURE 1.2: Simulated atmospheric infrared transmission spectrum from [1].

spectroscopy. As previously stated, the LWIR lies in an atmospheric transmission window so LWIR signals significant distances from the detector can be sensed. Also, as seen in Figure 1.1, the peak spectral radiance of a room temperature blackbody lies withing this range. These two factors make the LWIR the ideal wavelength range for long range infrared spectroscopy in which the terrestrial infrared radiation is the source, with the radiation passing through the gas being studied and on to the detector. If the detector is sufficiently sensitive, the difference of this signal from background can be sensed and the chemical composition can be deduced. Of course, increases in sensitivity allow for the detection of lower concentration of gases at greater range, so the focus of our work has been on maximizing device sensitivity.

There are many different technologies which have been used to detect LWIR radiation. Photon detectors measure infrared signals by measuring the creation of electron-hole

pairs in narrow bandgap semiconductors such as HgCdTe [4] from the absorption of radiation. Photon detectors offer natural spectral selectivity in their absorption due to the semiconductor bandgap but require cryogenic cooling to suppress the thermal excitation of carriers. Golay cells rely on the expansion of a small amount of trapped gas due to the heating of an infrared absorber. The expansion causes a deflection in a diaphragm which can be measured optically [5]. Golay cells demonstrate high sensitivity but have seen limited use due to their complexity of operation, requiring an independent optical readout system, and their sensitivity to vibrations.

Uncooled thermal infrared detectors have been the technology of choice for decades in the thermal imaging field. Specifically, vanadium oxide based resistive bolometers have seen extensive development since their inception in the 1980's. The technology was developed at Honeywell [6, 7], but has since been licensed to several other companies including DRS and Raytheon [8, 9]. Vanadium oxide is a preferred sensing material because of its high temperature coefficient of resistance and good 1/f noise characteristics. Other companies, such as L3 Communications have been developing infrared imaging arrays with amorphous Si sensing layers [10]. The basic design of uncooled microbolometers has changed very little in the past three decades with one main innovation being the shrinking of pixel size to reduce cost and improve resolution with more pixels on target. A major design change has been the umbrella designs patented by DRS and NEC [11, 12] which allow for the absorption of signal even in the areas of the support structure and circuitry which allows for a greater pixel density and fill factor.

Significant effort towards commercialization of uncooled thermoelectric infrared detectors has been done by NEC [13] and Heimann Sensor [14]. Thermoelectric detectors have lower responsivity than resistive bolometers but offer the advantage of reducing 1/f noise due to lack of current bias. In academia, high detectivity devices have been made using thermopile readouts in a bolometer-like configuration [15–17].

Cavity coupling has seen extensive use in the bolometer field, but typically in the antiresonant configuration in which a quarter wave cavity is used to improve the broadband coupling of radiation. The DRS umbrella design uses two independent optical cavities to improve broadband coupling. Resonant cavity coupling offers an advantage in the reduction of radiation noise and thermal conductivity, which can greatly boost the performance of the device. Theoretical work by Almasri [18] has shown how a tunable detector can be used to switch between antiresonant LWIR coupling and resonant MWIR coupling. Our work represents the first use of resonant cavity coupling in a state of the art detector.

1.2 State of the Art

Since our detector uses a thermoelectric readout, let us first look at the state of the art in this field. Haenschke et. al. [16] have reported the most sensitive thermopile infrared detectors prior to this work. Little detail was given about the thermoelectric films used, but they do reveal that a silver black absorption layer is used to obtain strong broadband infrared absorption. They measure a responsivity of 247 V/W and a specific detectivity of 1.86x10^{9}cm$\sqrt{Hz}$/W. Foote et. al.[15] have also reported a high-sensitivity thermopile infrared detector. Their work uses 11 sputtered Bi-Te/Bi-Sb-Te thermoelectric junctions suspended on a SiN_x membrane. The devices have a peak responsivity of 1100 V/W with a thermal time constant of 99ms. With Johnson noise limited performance, their devices have a total noise of 26 nV/$\sqrt{Hz}$ with a specific detectivity of 1.4x10^{9}cm$\sqrt{Hz}$/W.

Resistive microbolometers still tend to be the technology of choice for thermal infrared detection, and most of current academic and industrial research is devoted to this field. Tezcan et. al. [19] present the most sensitive complimentary metal-oxide-semiconductor (CMOS) processed thermal infrared detectors to date. The CMOS fabrication process is highly standardized and available in many industrial fabrication facilities so detector technologies compatible with this process are particularly interesting for commercialization. These devices use the n-well of a CMOS wafer as the infrared sensitive area. The electrical components of the device are fabricated in the CMOS process and then the devices are etch released post-CMOS using a selective tetramethylammonium hydroxide (TMAH) etch which requires no lithography. The n-well has a relatively poor TCR of .34%/K, but offers a significant reduction to 1/f noise since it is made from single crystal Si. Single pixel detectors demonstrate a responsivity of 9250 V/W with a thermal time constant of 21ms leading to a peak specific detectivity of 2.0x10^{9}cm$\sqrt{Hz}$/W.

The most sensitive uncooled infrared detectors in the standard configuration (non-nanowire) were reported by Sedky et. al. [20, 21]. These devices are chemical vapor deposition (CVD) SiGe based resistive bolometers fabricated using standard surface micromachining techniques. These devices use a 1/4 wavelength cavity to couple radiation into a thin NiCr absorber inducing broadband anti-resonant coupling greater than 90% from 8-14μm. This work describes the optimization of many device geometries, but the best devices have a responsivity of 139700 V/W, thermal time constant of 10.35 ms, and a peak specific detectivity of 2.3x10^{9}cm$\sqrt{Hz}$/W.

Before the publication of our work, the most sensitive infrared detectors were reported by Renoux et. al. [22] These detectors use platinum nanowires as their absorbing and detecting material. The fabrication process is straightforward with a single lithography step used to pattern the platinum in a four point probe configuration. With

these devices, they measure a responsivity of 31000 V/W and a specific detectivity of 2.7x10^{9}cm$\sqrt{Hz}$/W with a thermal time constant of 4ns. These detectivity values, however, are only achieved for exceedingly small devices 300nm x 300nm. Given the geometry of these detectors, the actual emissive area of the devices is unclear since the platinum in the source and sense probes will absorb equally to the absorber and a fraction of the heat absorbed in these areas will be sensed.

For comparison, the devices we present are thermopile infrared detectors made from four junctions of co-sputtered Bi_2Te_3/Sb_2Te_3 incorporated into an extreme thermal isolation structure made from a thin Al_2O_3 structural layer. The devices use a two die fabrication process to employ a half wave cavity coupling scheme to enhance absorption on resonance while rejecting unwanted radiation noise. Our thermoelectric films have Seebeck coefficients of -45μV/K and 105μV/K, resistivities of 7.6$\mu\Omega$-m and 17.4$\mu\Omega$-m, and thermal conductivities of .34 W/m-K and .3 W/m-K for Bi_2Te_3 and Sb_2Te_3 respectively. We measure a peak responsivity of 4700V/W in the LWIR with a thermal time constant of 59ms. The devices exhibit Johnson noise limited performance with a noise level of 16nV/$\sqrt{Hz}$ and a specific detectivity of at least 3.0x10^{9}cm$\sqrt{Hz}$/W. We have also used a microapperture to clearly define the emissive area of the detector for accurate detectivity calculations. These results will be discussed in detail in Chapter 7.

1.3 Organization of Chapters

The remaining chapters are organized into three main areas: background, new concepts, and device fabrication and characterization. Chapters 2 and 3 introduce the background knowledge necessary to understand device design and performance. Chapter 2 introduces the theory of thermoelectric devices from device performance and figure of merit estimates to the selection and engineering of materials. Chapter 3 describes the theory of thermal infrared detectors. The various performance metrics are described and device designs are presented which apply experimental and theoretical results to the design of a thermoelectric infrared detector.

Chapters 4 and 5 introduce two new concepts for the design and analysis of infrared detectors and thermoelectric microcoolers. Chapter 4 proposes the use of narrow bandgap semiconductors as spectrally selective absorbers for midwave infrared detection. This theoretical work shows how with proper optical engineering and device design, a PbSe based infrared detector can operate in the MWIR at detectivities beyond the black-body radiation limit. Chapter 5 introduces a method for the analysis of the radiation contribution to thermal conductance in highly thermally isolated microstructures. We describe a theory in which the non-linearity of the temperature response to input power

of a device can be measured and used to calculate the magnitude of the film and radiation thermal conductance at a given temperature. This theory is then demonstrated using released microcoolers.

Chapters 6 and 7 describe the fabrication and characterization of the state of the art uncooled thermal infrared detectors with cavity coupled absorption, which are the centerpiece of this work. Chapter 6 outlines the various engineering challenges faced when depositing co-sputtered Bi_2Te_3/Sb_2Te_3 thermoelectric junctions and incorporating them into highly thermally isolated microstructures. The fabrication process for the micropillar micromirrors and the microaperatures is also described, as well as the methods used to assemble these components into a working optical cavity. Chapter 7 outlines the characterization of the detectors described in the previous chapter. This includes optical characterization of the components and cavities, electrical characaterization of the thermoelectric thin films, and finally the measurement of device performance metrics such as responsivity, thermal time constant, and specific detectivity.

Finally, in Chapter 8 we draw conclusions based on the work and explore the various methods available to improve the performance of our devices, both by optimizing our existing technology and by redesigning or improving components of the device.

Chapter 2

Inroduction to Thermoelectrics

2.1 Introduction

This chapter is intended to give the reader an understanding of thermoelectric physics, materials, and derivations of device performance metrics. We will first introduce the Seebeck effect and then apply that knowledge to a generic thermoelectric junction to derive the equations for the temperature difference of the thermoelectric cooler in order to introduce the thermoelectric figure of merit. The state of the art for not only thermoelectric materials will be investigated with particular attention given to thermoelectric thin films.

2.2 The Seebeck Effect

The basic operation of thermoelectric infrared detectors relies on the Seebeck effect as an electrical transduction mechanism, converting temperature changes into voltage which can be measured to determine the amount of radiative power absorbed by the detector. The Seebeck effect occurs when a material, in our case a semiconductor, is contacted by metals at two ends and a temperature difference exists across the semiconductor as shown in Figure 2.1. Consider an n-type semiconductor such as Bi_2Te_3 contacted on both ends by a metal. Since semiconductors typically have Seebeck coefficients orders of magnitude higher than metals, we ignore the Seebeck effect in the metal. The band structure of such a setup in thermal equilibrium is seen in Figure 2.2. In this case there is no temperature difference and therefore no band bending or carrier excitation causing no voltage to be generated. If we apply a temperature difference, however, the band structure bends as seen in Figure 2.3. The Seebeck effect is actually

a summation of three different effects. The first relates to the thermal excitation of carriers. Carrier concentration increases exponentially with temperature so as we heat one side of the semiconductor an imbalance in carrier concentration develops between the hot and cold side of the semiconductor. This imbalance and the excess carrier energy on the hot side causes a diffusion current from the hot side to the cold side which causes the hot junction to have a positive potential, while the cold side has negative potential from the pileup of electrons. The second effect relates to thermal manipulation of the Fermi level of the hot junction. The magnitude of the Fermi level of the hot junction relative to the conduction band becomes larger than the cold junction as seen in Figure 2.3 which augments the previously described effect. The final effect relates to phonon diffusion from the hot to cold junction. The thermal imbalance causes phonon diffusion current to flow from hot to cold and the collisions between phonons and electrons augments the diffusion current of electrons [23].

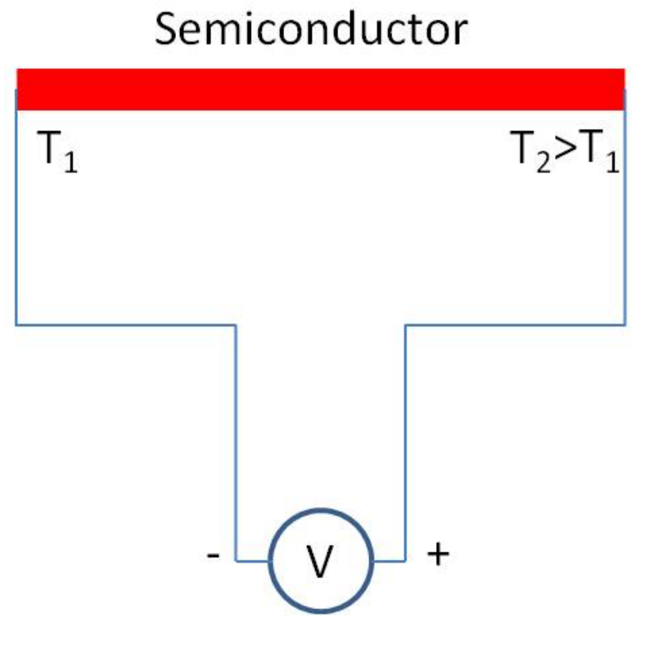

FIGURE 2.1: Schematic of a semiconductor demonstrating the Seebeck effect.

2.2.1 Seebeck Coefficient

The Seebeck effect is present in all materials, but the magnitude of the effect varies from material to material. The Seebeck coefficient quantifies the voltage response of a material to induced temperature difference. For a junction consisting of two materials, the voltage response is given by Equation 2.1,

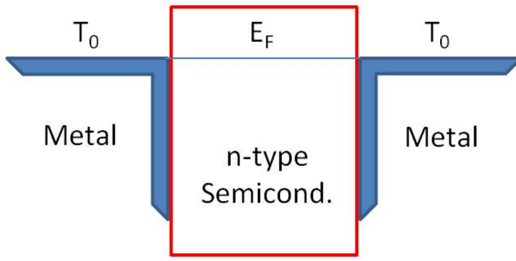

FIGURE 2.2: Band structure of an n-type semicondcuctor under thermal equalibrium.

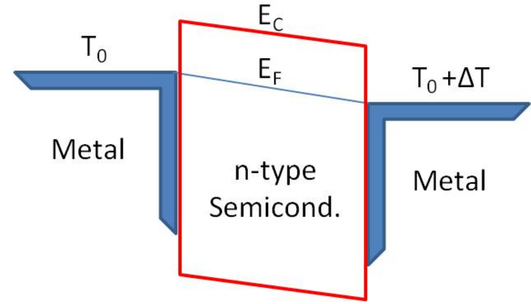

FIGURE 2.3: Band structure of an n-type semicondcutor with applied temperature difference.

$$V = \int_{T_1}^{T_2} (S_B(T) - S_A(T))dT \tag{2.1}$$

where S_B and S_A are the Seebeck coefficients of the two materials, and T_1 and T_2 are the temperatures of the two sides of the junction. In the case that the Seebeck coefficient is not dependent on temperature, the voltage response is simply $V{=}\Delta S \Delta T$.

2.3 Thermoelectric Cooling

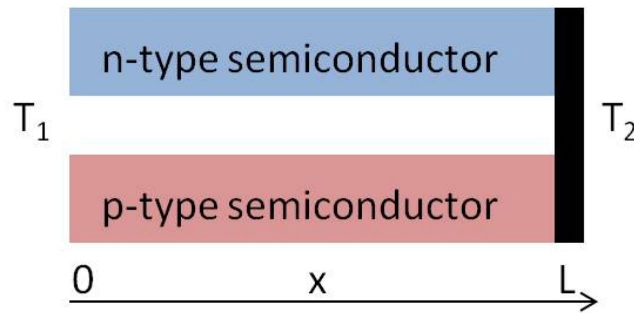

FIGURE 2.4: Layout of the generic thermoelectric junction used for performance derivation.

To analyze the performance of a generic semiconductor thermoelectric junction, consider the junction shown in Figure 2.4 with an n-type and p-type thermoelectric junction joined at $x = L$ by a metallic contact. If we apply a current, I, in the correct direction, Peltier cooling will occur. This cooling will be counteracted by thermal conduction back through the films, which for the n-type semiconductor is described in Equation 2.2 [24],

$$Q = -SIT - \kappa A \frac{dT}{dx} \tag{2.2}$$

where Q is the heat transported from $x = L$ to x=0, S is the Seebeck coefficient, I is the current, T is the absolute temperature, and A is the cross sectional area of the film. Since we are sourcing a current, the junction will also be impacted by Joule heating. The Joule heating per unit length is given by Equation 2.3 [24],

$$-\kappa A \frac{d^2T}{dx^2} = \frac{I^2\rho}{A} \tag{2.3}$$

where ρ is the resistivity of the material and all other variables have been defined following Equation 2.2. We then apply the boundary conditions that $T = T_1$ at x=0 and $T = T_2$ at $x = L$ solve Equation 2.3 to find Equation 2.4.

$$\kappa A \frac{dT}{dx} = \frac{-I^2\rho(x - L/2)}{A} + \frac{kA(T_2 - T_1)}{L} \tag{2.4}$$

We can then evaluate Equation 2.4 at x=0 to find the rate of heat flow to the heat sink and then add the result for the n-type and p-type semiconductor to find the total heat flow of a junction to the heat sink in Equation 2.5,

$$Q = S_T I T_1 - G(T_2 - T_1) - \frac{I^2R}{2} \tag{2.5}$$

where S_T is the total Seebeck coefficient difference of the two materials S_T=S_p-S_n, G is the total thermal conductance of the two materials in parallel $G = (\kappa A/L)_p + (\kappa A/L)_n$ and R is the total resistance of the two materials $R = (\rho L/A)_p + (\rho L/A)_n$.

If we wish to evaluate the maximum cooling of a thermoelectric device, we need only to take the derivative of Equation 2.5 with respect to I, set it equal to zero, and solve for I, to find $I_{max} = ST_1/R$. If we plug this value back in to Equation 2.5 and set $Q = 0$ we can obtain the expression for maximum cooling seen in Equation 2.6. The maximum cooling occurs when $Q = 0$ because at this point the thermoelectric power is exactly being dissipated by the thermal conduction through and Joule heating in the thermoelectric films.

$$(T_2 - T_1)_{max} = \frac{S^2T_1^2}{2GR} \tag{2.6}$$

From Equation 2.6 it is clear to see the origins of the thermoelectric figure of merit, Z, shown in Equation 2.7.

$$Z = \frac{S^2}{GR} = \frac{2(T_2 - T_1)_{max}}{T_1^2} \tag{2.7}$$

While Equation 2.7 describes the figure of merit for thermoelectric cooling, it also serves as a reasonable metric for thermoelectric detector applications. Consider the detectivity of a Johnson noise limited detector like those which will be described in Chapter 7 expressed in Equation 2.8,

$$D^* = \frac{\epsilon S\sqrt{A}}{G\sqrt{4k_bTR}} \propto \frac{S}{G\sqrt{R}} \tag{2.8}$$

where ϵ is the emissivity of the device, A is its area, R its resistance, T its absolute temperature, and the remaining thermoelectric terms have previously been defined in this chapter. For this analysis, only the proportionality between specific detectivity and the three controllable parameters of thermoelectric materials is important. We see comparing Equations 2.7 and 2.8 that many of the factors present in the thermoelectric figure of merit are also vital in infrared detector performance.

2.4 Thermoelectric Materials

From Equation 2.7 it is plain to see that desirable properties for thermoelectric materials include high Seebeck coefficient, low thermal conductivity, and low electrical resistivity. However, the fact that these parameters are to some extent coupled makes the selection and engineering of materials much more difficult. For the moment we will ignore the thermal conductivity and consider the thermoelectric power factor, P_f=S^2/ρ. Using the relaxation time approximation for scattering and assuming open circuit conditions, the theoretical Seebeck coefficient is defined in Equation 2.9 [25],

$$S = -\frac{k_b}{e}[ln(\frac{N_c}{n}) + \frac{5}{2} + r] \tag{2.9}$$

where S is the Seebeck coefficient, k_b is the Boltzmann constant, e is the elementary charge, N_c is the density of states of carriers, n is the number of electrons, and r is the a loosely defined parameter which varies based on the dominant type of scattering, from r=-3/2 for lattice scattering and r=1/2 for ionized impurity scattering [25]. For this analysis we assume ionized impurity scattering is dominant. Using effective mass and effective density of states values for electrons in Si from [26], we are able to calculate the Seebeck coefficient as a function of carrier concentration, n, as shown in Figure 2.5.

To calculate the power factor we must also consider the electrical conductivity, σ, which is defined as σ=$en\mu$, where the carrier mobility, μ, is calculated for phosphorous doped Si using constants from Van Zeghbroek [27]. We can then calculate the electrical

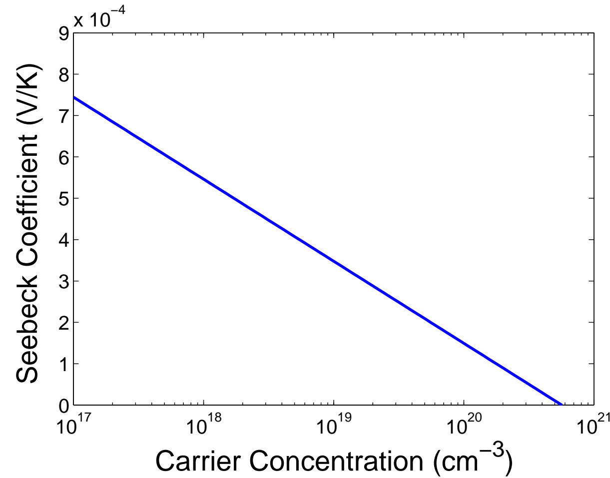

FIGURE 2.5: Seebeck coefficient vs carrier concentration for Si.

conductivity as a function of doping for P doped Si as shown in Figure 2.6. We can see in this image that on the semi-logarithmic scale the electrical conductivity has an exponential dependence on carrier concentration.

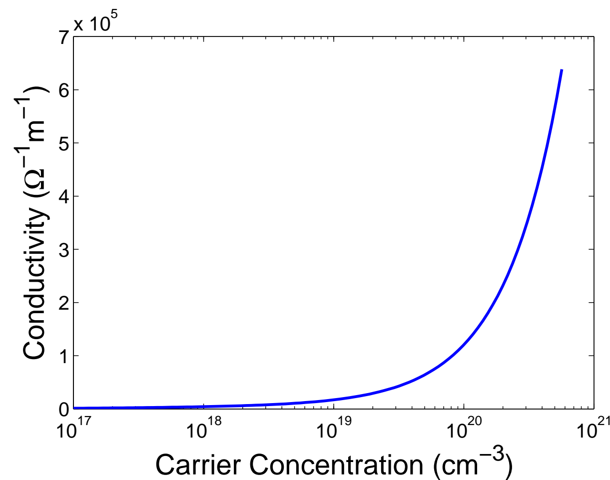

FIGURE 2.6: Electrical conductivity vs carrier concentration for P doped Si.

From Figure 2.5 we see that on the semi-logarithmic scale the Seebeck coefficient has a linear dependence on carrier concentration, while Figure 2.6 shows that on the same scale, the electrical conductivity has an exponential dependence on carrier concentration. If we combine the equations for thermoelectric power factor, electrical conductivity, and Seebeck coefficient shown in Equation 2.9 we can calculate the the dependence of the thermoelectric power factor on carrier concentration shown in Figure 2.7.

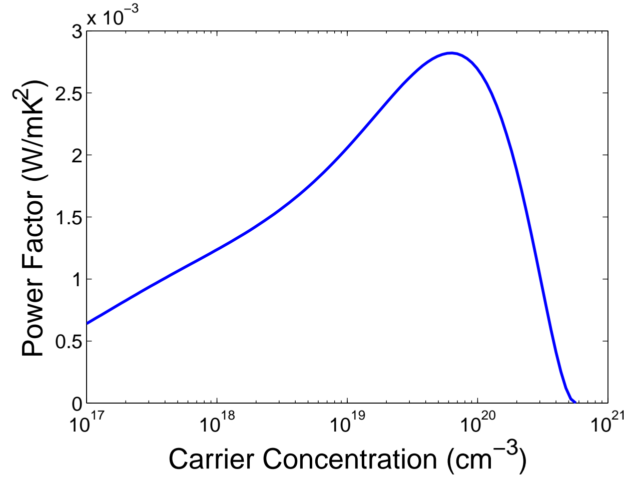

FIGURE 2.7: Thermoelectric power factor vs carrier concentration.

2.5 Selection of Thermoelectric Materials

It is clear to see from Figure 2.7 that the thermoelectric power factor is optimized for degenerately doped semiconductors. At low doping, a semiconductor will have a high Seebeck coefficient, but the electrical conductivity will be too low for device application. On the contrary, metals have very high conductivity, but their Seebeck coefficients are extremely low. We also know that the electronic component of the thermal conductivity κ_e is coupled to the electrical conductivity by the Wiedemann-Franz law shown in Equation 2.10,

$$\frac{\kappa_e}{\sigma} = L_N T \tag{2.10}$$

where κ_e is the electrical component of the thermal conductivity, σ is the electrical conductivity, L_N is the Lorentz number which is equal to or near 2.44x10^{-8} WΩK^{-2}, and T is the absolute temperature. This leaves all components of the thermoelectric figure of merit optimized for degenerately doped semiconductors besides the phonon contribution to the thermal conductivity, κ_p. For this reason, the selection and engineering of thermoelectric materials revolves around the reduction of κ_p.

The phonon contribution to thermal conductivity is minimized in materials with low Debye temperatures. Debye temperature decreases as atomic mass increases so materials with high atomic mass are preferable [28]. To reduce lattice thermal conductivity, we look towards semiconductor compounds made from heavy elements such as Pb, Bi, Sb, and Te. For this reason, Bi_2Te_3 demonstrates some of the best thermoelectric properties at room temperature and has been the material of choice for over half a

century [29, 30]. Bi_2Te_3 also has some process integration advantages in that its doping and therefore carrier concentration is controlled by the relative concentration of Bi and Te in the material so the material can be changed from n-type to p-type simply by changing deposition conditions. It was later found that the mobility of holes in Sb_2Te_3 is significantly higher than Bi_2Te_3 [31] so state of the art thermoelectric devices often consist of n-type Bi_2Te_3 and p-type Sb_2Te_3 thermoelectric junctions. However, these materials have a low melting point and low band gap energy, .15V in Bi_2Te_3 [32] so other materials must be used at higher temperatures. The best thermoelectric materials at each temperature are shown in Figure 2.8 taken from [33].

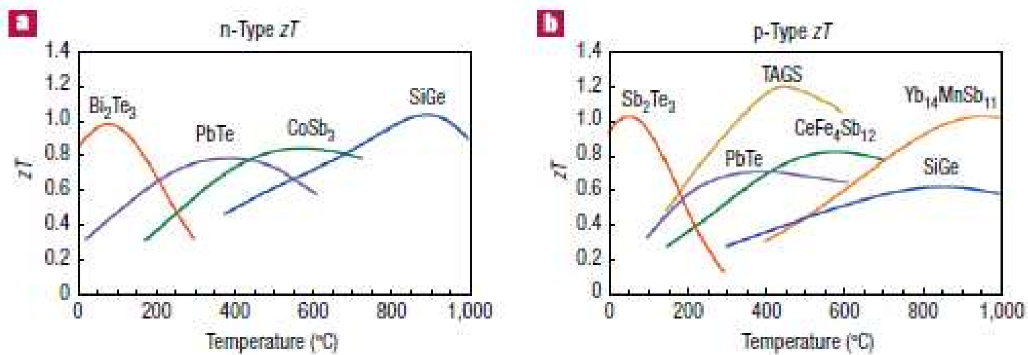

FIGURE 2.8: Thermoelectric figure of merit for all temperatures for n-type (a) and p-type (b) semiconductors from Snyder [33].

Solid solutions of materials such as Bi_2Te_3 and Sb_2Te_3 offer significant advantages over their pure counterparts. The addition of a minority element, say the addition of Sb to Bi_2Te_3 creates point defects in the crystal without comprising the crystal lattice. Since electrons in these crystals have wavelengths on the order of tens of atomic spacings and phonons have much shorter wavelengths, the point defects scatter phonons much more efficiently than they do electrons. This acts to decouple the electrical and thermal conductivity. The idea was first proposed by Ioffe in 1956 [34] and expanded upon by Wright in 1958 [35] and Goldsmid in 1968 [36] with significant modern research into the optimization of these materials [37, 38].

2.6 Engineering of Thermoelectric Materials

N-type Bi_2Te_3, p-type Sb_2Te_3, and their solid solutions offer the best thermoelectric properties for naturally occurring materials near room temperature. Their unitless thermoelectric figure of merit, ZT, has remained near unity since the 1950's with minimal hope for the significant improvement required for thermoelectric cooling and generation to become a disruptive technology. However, improvements can be made by engineering

materials which further enhances the decoupling of electrical and thermal conductivity. One such innovation is the use of Skutterudites as thermoelectric materials. Skutterudites are compounds with octahedral lattice structures with large voids in the center of the unit cell. These voids serve as natural doping sites, and, when doped, the trapped dopant atom can serve as a phonon trap. The most common Skutterudite thermoelectric material is filled CoSb, a material with fairly high thermal conductivity. A bulk of the research on this material has been focused on the reduction of thermal conductivity through engineering of the dopant composition [39–41]. However, improvements over standard materials have only been made using Skutterudites at high temperatures, and have failed to unseat Bi/Sb/Te compounds at room temperature.

A very promising field of engineered thermoelectric materials is the use of nanostructured materials. Perhaps the most famous example is that of Venkatasubramanian [42] in which superlatices of Bi_2Te_3 and Sb_2Te_3 have been demonstrated to have a dimensionless thermoelectric figure of merit of up to 2.4. When a current flows in the direction perpendicular to the thermoelectric films there are two distinct advantages. First, both electrons and phonons will encounter many interfaces between Bi_2Te_3 and Sb_2Te_3 which more strongly suppresses phonon transfer than electron transfer. Secondly, with Bi_2Te_3 having a narrower bandgap than Sb_2Te_3, the superlattice forms a series of quantum wells, which act to trap cold electrons. Quantum confinement has also been used to increase the power factor of PbTe films by a factor of four in by Hicks [43]. Theoretical work by Dragoman [44] has demonstrated that quantum confinement in graphene could produce a Seebeck coefficient of .03 V/K with a dimensionless figure of merit of up to 20 using the so called giant thermoelectric effect. Currently, however, most of these engineered materials are in their infancy, so Bi_2Te_3, Sb_2Te_3, and their solid solutions remain the materials of choice at room temperature.

2.7 Thermoelectric Materials for MEMS Devices

Since the focus of this work is microelectromechanical (MEMS) devices, it is important to consider the state of the art for thermoelectric materials with a focus on those incorporated into MEMS devices. Much like bulk materials, the focus of room temperature thermoelectric thin film materials have been based on Bi_2Te_3, Sb_2Te_3, and their solid solutions. A wide variety of deposition methods are currently in use for film studies of thermoelectric materials. Materials studies have been conducted on these films deposited using electrodeposition [45], MOCVD [46], sputtering of custom targets [47], and co-evaporation [48], but many of these studies entail the use of unprocessed and uncontacted films on glass. A majority of the thermoelectric films incorporated into

devices have been used in microcooler fabrication. To date, the best microcooler performance has been achieved by Gross [49], who used co-evaporated Bi_2Te_3 and Sb_2Te_3 with Seebeck coefficients of -210μV/K and 160μV/K and electrical resistivities of 20.2$\mu\Omega$-m and 12.9$\mu\Omega$-m respectively. Using these films and a multistage cooler design, a maximum cooling of 22.3°C is achieved.

Of specific interest to our work are infrared detectors with thermoelectric readout. Thermoelectric readouts offer the advantage of reduction of 1/f noise due to operation in the absence of electrical bias. High performance thermopile infrared detectors have been reported by Foote who fabricated thermopile detectors consisting of sputtered Bi-Te, Bi-Sb-Te films with Seebeck coefficients of -136μV/K and 153μV/K and resistivities of 13$\mu\Omega$-m and 22$\mu\Omega$-m for Bi-Te and Bi-Sb-Te respectively. These thermopile detectors had a specific detectivity of 1.4x10^9 cm$\sqrt{Hz}$/W [15]. Before this work, the best thermopile detector performance was reported by Volklein who deposited p-type $(Bi_{1-x}Sb_x)_2Te_3$ and n-type $Bi_{1-x}Sb_x$ deposited via flash evaporation [17]. These devices had relatively low responsivity due to high thermal conductance but a specific detectivity of 7.7x10^8 cm$\sqrt{Hz}$/W. A study by Kim in electrodeposition of n-type Bi_2Te_3 and p-type Sb_2Te_3 for thermopile detectors yielded films with Seebeck coefficients of -51.6μV/K and 52.1μV/K respectively. With a 196 junction detector, they measured a responsivity of 7300 V/K [50]. Though their devices were far from the state of the art, this deposition method is promising for future work.

Chapter 3

Thermal Detector Background and Design

3.1 Introduction

This chapter is intended to provide the reader with a solid background in the operation of thermopile infrared detectors. Starting from the heat balance equation of a thermal isolation structure, we outline the performance metrics of thermal infrared detectors and their relationship to material properties and design parameters. Special attention is paid to the calculation of radiation thermal conductance noise since the reduction of this noise source is one of the significant contributions of our work. After the performance calculations have been outlined, the design of our uncooled thermopile infrared detectors is outlined with both layout and optical design. Using this design, and previously measured material properties we are able to theoretically analyze the proposed device.

3.2 Detector Response

The analysis of the voltage response of a thermal infrared detector with frequency modulated input signal begins with the analysis of the power balance seen in Equation 3.1,

$$C\frac{d(\Delta T)}{dt} + G(\Delta T) = \eta P_0 e^{i\omega t} \tag{3.1}$$

where ΔT is the temperature change of the device, C is the thermal capacitance, G is the thermal conductance, t is time, η is percentage of the of incident power absorbed related to emissivity and geometric effects, P_0 is the magnitude of the incident radiation power, and ω is the angular frequency of the frequency modulated signal. If we solve Equation 3.1 for ΔT we arrive at Equation 3.2,

$$\Delta T = \frac{\epsilon P_0}{G(1+\omega^2\tau^2)^{1/2}} \tag{3.2}$$

where τ is the thermal time constant τ=C/G. In the case of a DC or near DC input signal Equation 3.2 simplifies to ΔT=$\epsilon P_0/G$.

The analysis thus far has been independent of readout mechanism, but in order to describe the responsivity we must factor in the response of a thermoelectric element described in Equation 3.3,

$$\Delta V = NS\Delta T \tag{3.3}$$

where ΔV is the voltage response of a thermoelectric element due to the temperature difference ΔT, N is the number of thermoelectric elements, and S is the Seebeck coefficient difference of the two materials in the junctions. If we combine Equations 3.2 and 3.3 we can calculate the responsivity as shown in Equation 3.4.

$$\Re = \frac{\Delta V}{P_0} = \frac{\eta NS}{G(1+\omega^2\tau^2)^{1/2}} \tag{3.4}$$

Under DC or near-DC illumination Equation 3.4 simplifies to $\Re$=$\eta NS/$G.

3.3 Noise in Thermal Infrared Detectors

Uncooled infrared detector performance is impacted by three major noise sources, thermal conductance noise, Johnson noise, and 1/f noise. The noise equivalent power (NEP) of an infrared detector is defined as "the radiation power capable of producing a signal voltage equal to the noise voltage, that is, a signal-to-noise ratio of unity." [51] The total NEP of an infrared detector is given by Equation 3.5 [51, 52],

$$(NEP)^2 = G^2\frac{k_bT^2}{C} + \frac{1}{\Re^2}\left(4k_bTR(f_2-f_1) + (I_bR)^2k_m\ln\frac{f_2}{f_1}\right) \tag{3.5}$$

where G is the thermal conductance, k_b is the Boltzmann constant, T is the absolute temperature of the device, C is the thermal capacitance, $\Re$ is the responsivity, R is the device resistance, f_2 and f_1 are the upper and lower measurement cutoff frequencies determined by the readout system of the device, I_b is the applied bias current, and k_m is the 1/f noise parameter of a resistive readout. The first term of Equation 3.5 represents the thermal conductance noise of the device which is caused by phonon fluctuations between the device and the heat sink through the support structure and photon fluctuations into and out of the plate. The impact of phonon fluctuations through thin films can be calculated as a function of device geometry and material parameters specific heat and thermal conductivity, but the photon fluctuations become significantly more difficult to calculate, especially in a spectrally selective device as will be discussed in Section 3.5. The second term of Equation 3.5 represents the Johnson noise, a thermal fluctuation in carrier energy present in all resistors. In the case of a DC illuminated room temperature detector, like those which will be characterized in Chapter 7, the Johnson voltage noise is dependent solely on the total resistance of the device. The final noise source is the 1/f noise. In a resistive microbolometer the 1/f noise is dependent on the measurement bandwidth, the bias current, resistance, and the 1/f noise parameter of the resistor. However, in a thermoelectric readout scheme, there is no need for current biased operation and therefore and this term should go to zero.

3.4 Detectivity

Specific detectivity is the figure of merit for thermal infrared detector sensitivity. Specific detectivity is defined in Equation 3.6,

$$D^* = \frac{\Re\sqrt{A}}{\sqrt{\overline{V^2}}} \tag{3.6}$$

where D^* is the specific detectivity in cm$\sqrt{Hz}$/W, $\Re$ is the responsivity in V/W, A is the detector area in cm^2, and $\sqrt{\overline{V^2}}$ is the RMS voltage noise in V/$\sqrt{Hz}$.

3.5 Radiation Thermal Conductance Noise

Since our device designs will rely on cavity coupling to reduce radiation thermal conductance noise we must derive a method to analyze the radiation noise of a device for which the emissivity depends on wavelength and solid angle. This derivation is available in some form in a variety of sources [51, 53, 54] but will also be outlined here. We

start by examining the average number of photons per mode in a box, n_p, at a given temperature, T, given by Equation 3.7,

$$\overline{n_p} = \frac{1}{e^{(h\nu/kT)} - 1} \tag{3.7}$$

where h is Planck's constant, ν is frequency, and k is the Boltzman constant. Assuming that the photons obey Bose-Einstein statistics we know that the average deviation in the number of photons per mode is then defined by Equation 3.8.

$$\langle(\Delta n_p)^2\rangle = \overline{n_p} + \overline{n_p^2} = \frac{e^{(h\nu/kT)}}{(e^{(h\nu/kT)} - 1)^2} \tag{3.8}$$

Knowing the average deviation in the number of photons per mode, we must now calculate the density of modes. We look at the volume of a spherical shell in k-space dν=4πk^{2}dk, where k=2$\pi\nu$/c. We must divide this by eight since each only one octant has independent modes as well as multiply by two to account for polarization. Finally we must divide by π^3/L^3 as modes occur at each point mπ/L, where m is an integer. This gives us the density of states given in Equation 3.9.

$$N_p = \frac{8\pi\nu^2 d\nu}{c^3} \tag{3.9}$$

If we combine Equations 3.8 and 3.9 arrive at an expression for the numerical photon fluctuations in a thermal detector at a specific frequency, but since thermal detectors absorb radiation power, we must account for energy fluctuations by multiplying by $(h\nu)^2$. We also factor out a factor of 4π since we are dealing with a detector for which the emissivity depends on not only wavelength but solid angle, $\epsilon(\nu,\theta,\phi)$ where ν is the frequency, θ is the tangential angle, and ϕ is the azimuthal angle to arrive at Equation 3.10.

$$\overline{\Delta E^2} = \int\limits_{\nu,\theta,\phi} \frac{2h^2\nu^4}{c^3} \frac{e^{(h\nu/kT)}}{(e^{(h\nu/kT)} - 1)^2} \epsilon(\nu,\theta,\phi) sin(\theta) d\phi d\theta d\nu \tag{3.10}$$

However, our simulations use wavelength depended emissivity, $\epsilon(\lambda,\theta,\phi)$ so Equation 3.10 becomes Equation 3.11.

$$\overline{\Delta E^2} = \int\limits_{\lambda,\theta,\phi} \frac{2h^2c^2}{\lambda^6} \frac{e^{(hc/\lambda kT)}}{(e^{(hc/\lambda kT)} - 1)^2} \epsilon(\lambda,\theta,\phi) sin(\theta) d\phi d\theta d\lambda \tag{3.11}$$

These energy fluctuations occur both for emission and absorption, so for a complete analysis of radiation noise, we must integrate Equation 3.11 at both the detector and the background temperature, or in the case where both are at the same temperature, simply multiply by two if the detector and background are at the same temperature.

3.6 Device Design

There are many engineering challenges to be faced when designing uncooled thermoelectric infrared detectors for maximum performance. As previously shown, many design parameters must be considered to maximize the detectivity of the device within the scope of realistic material parameters given our fabrication facilities and knowledge base. We will look to minimize the thermal conductance noise by reducing both thermal conductance through the support structure and thermoelectric films, as well as minimize thermal conductance due to radiation using a cavity coupling scheme. Reductions in thermal conductance must be accompanied by reductions in thermal capacitance so that the thermal time constant is kept at a reasonable level. We will minimize Johnson noise by reducing the resistance of the device with high quality thermoelectric materials. The effects of 1/f noise should be negated through the use of a thermoelectric readout. To maximize responsivity we must maximize the Seebeck coefficient difference between the two semiconductors and use multiple junctions to increase voltage signal. All these design parameters must be balanced in order to produce a high detectivity detector and the layout and optical design will be addressed.

3.7 Device Layout

An example of a uncooled thermopile detector mask design for the '1B' device geometry is shown in Figure 3.1. In this image we see the layout of the thermopile detectors with Ge/Ni optical absorber (purple) in the center, thermoelectric elements consisting of Bi_2Te_3 (green) and Sb_2Te_3 (tan) on the four support legs connected electrically both near the junction and around the outside of the etch pit by a Ti/Pt interconnect layer (gray). The Cr/Au bond pad layer (spotted green) forms not only the bond pads but an electrical connection layer on top of the interconnect layer to reduce resistance around the outside. The Al_2O_3 support and encapsulation layer (pink) forms the thermal isolation structure. The etch pit (white) is defined by a backside mask which is not shown.

The overall size of the etch pit is 1mm with the optically absorbing center plate is 100μm by 100μm. A cross section of the thermoelectric legs can be seen in Figure

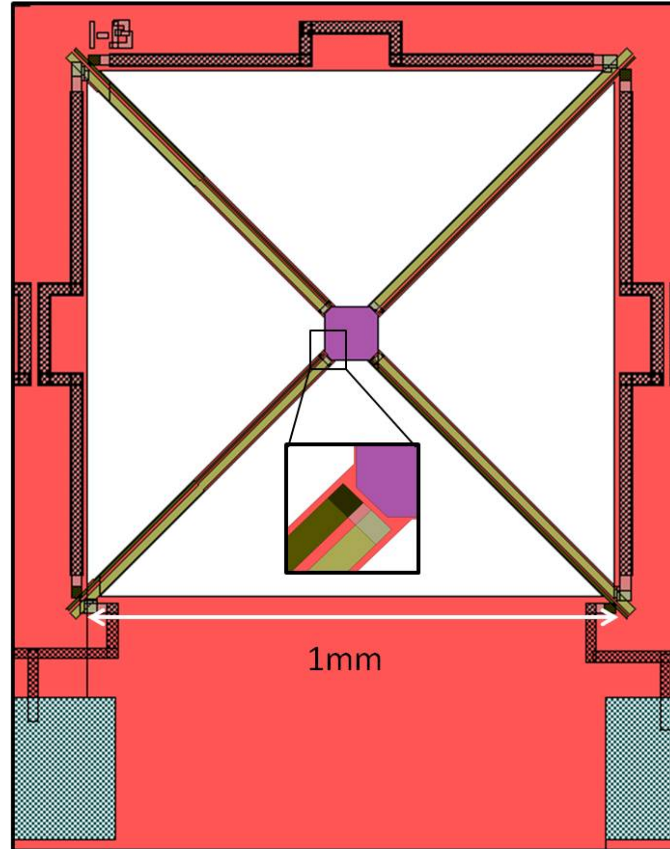

FIGURE 3.1: Mask layout of the '1B' device design.

3.2. The thickness of the thermoelectric materials is 550nm, while the total thickness of the structural and encapsulating Al_2O_3 is 50nm, 30nm on the bottom and 20nm on the top. The width of Bi_2Te_3 film is 5μm while the width of the Sb_2Te_3 film is 15μm. This inequality is intended to minimize the total resistance of the device since the resistivity of the Sb_2Te_3 film was at least three times that of Bi_2Te_3 in initial testing [55]. The total width of the structural Al_2O_3 is 31μm to allow for alignment tolerances.

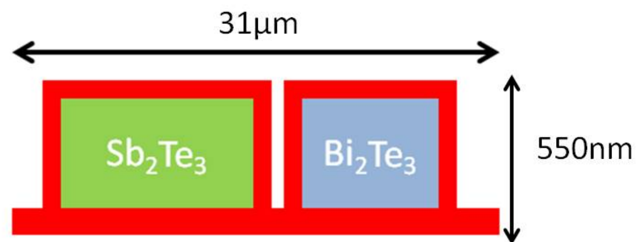

FIGURE 3.2: Cross section of the thermoelectric leg of the '1B' device design.

TABLE 3.1: Device design parameters and calculated device resistance and film thermal conductance for the device design using conservative estimates (column 2) and values published in the Hilton Head conference [55].

Parameter	Design	Hilton Head
$\rho_{Sb_2Te_3}$	30$\mu\Omega$-m	26.2$\mu\Omega$-m
$\rho_{Bi_2Te_3}$	10$\mu\Omega$-m	6.15$\mu\Omega$-m
Device Resistance	20400Ω	15200Ω
Seebeck Difference	170μV/K	183μV/K
$\kappa_{Sb_2Te_3}$	1 W/mK	1.02 W/mK
$\kappa_{Bi_2Te_3}$	1 W/mK	.88 W/mK
$\kappa_{Al_2O_3}$	2.6 W/mK	2.6 W/mK
G_{Film}	8.82x10^{-8} W/K	8.73x10^{-8} W/K

3.8 Device Simulation

Preliminary testing of the thermoelectric thin films was presented at the Hilton Head conference in 2012 [55]. Using the parameters measured for these films we can perform a preliminary analysis of the device performance. Actual device design was done with more conservative estimates for thermoelectric parameters to ensure that the devices were designed for a worst case scenario where properties reported in [55] were not repeatable. Design parameters for both scenarios are shown in Table 3.1. Where ρ is the resistivity, κ is the thermal conductivity, and G is the thermal conductance. The $\kappa_{Al_2O_3}$ value was taken from Gabriel [56].

3.9 Optical Design

In order to fully analyze device design parameters we must also consider the optical design of the device. A cross sectional schematic of the basic optical design can be seen in Figure 3.3. Here we see what is essentially a Gires-Tournois interferometer consisting of a a highly reflecting (R$\sim$100%) bottom mirror (M_1) with a second mirror (M_2) with significantly lower reflectance. The mirrors are separated by a $\lambda/2$ vacuum gap which creates a resonance at the desired wavelength, λ. M_1 consists of a distributed Bragg reflector (DBR) made from 2 alternating pairs of Ge and NaF. These materials have a large index mismatch in the long wave infrared (LWIR) so just two pairs produce near 100% reflectance. This mirror is also backed with an optically thick Cr layer to increase reflectance. M_2 is formed with a single Ge layer. Since Ge has a high index in the LWIR

a single layer has approximately a 70% reflectance in the LWIR. M_2 also includes a thin metallic absorber which will absorb radiation at the resonant wavelength.

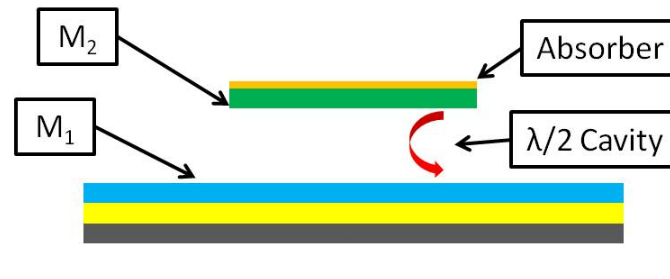

FIGURE 3.3: Cross sectional schematic of the optical device design.

Optical simulations in this section are done using the optical transfer matrix method described by Yeh [57]. This method simplifies Maxwell's equations for electromagnetic wave propagation through multilayer optical structures into a series of 2x2 matrices. Each layer simplifies to a single propagation matrix representing the wave traveling though each layer and two interface matrices representing the Snell's law interference as the wave enters and exits each layer. By multiplying the propagation and interface matrices of each layer in a multilayer stack we can calculate the transmission, reflectance, and absorption of the structure for each wavelength and angle. The simulations use optical constants from [58, 59]. The layer structure simulated can be seen in Table 3.2 and the simulated absorption spectra of this design can be seen in Figure 3.4. Here we see strong absorption peak centered at 10μm with a full width half maximum (FWHM) of 2.1μm with greatly suppressed aborption off resonance. The sharper absorption peaks at shorter wavelengths are due to secondary resonances in the cavity as well as resonsnce within the Ge mirror layer. Optical constants for these simulations were taken from [58, 59].

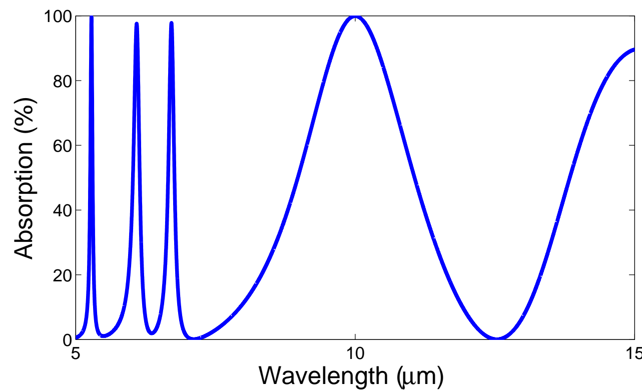

FIGURE 3.4: Simulated absorption spectrum of the layer structure of Table 3.2.

Table 3.2: Layer structure for the simulated optical device design.

Material	Thickness (nm)	Index (10μm)
Vacuum		1
Al_2O_3	20	.88
Ni	2.7	8.5+36.67i
Ge	300	4
Al_2O_3	30	.88
Vacuum	6200	1
Ge	625	4
NaF	2016	1.24
Ge	625	4
NaF	2016	1.24
Cr	2000	7.5+32.8i

3.10 Device Simulation Continued

Using the previously described optical design we can now complete the theoretical device analysis. The thickness and composition of the films in M_2 determines the thermal capacitance of the device, which allows for the calculation of the thermal time constant and thermal conductance noise. The absorption spectrum seen in Figure 3.4 can be integrated over all wavelengths and angles to evaluate the thermal conductance of the device due to radiation. We find that the radiation thermal conductance of this optical design is 3.27x10^{-8} W/K for a 100μm x 100μm detector, which is approximately 25% of the value of a blackbody detector with the same area. We can then calculate the total thermal conductance noise as well as the Johnson noise to calculate the total noise and therefore detectivity using the methods previously described in this chapter. The results of these calculations can be seen in Table 3.3, where s is the specific heat, C is the thermal capacitance, G is the thermal conductance, τ is the thermal time constant, $\Re$ is the responsivity, and D^* is the specific detectivity. Specific heat values were taken from [60]. Of note in these calculations is the fact that the total thermal conductance is lower than the radiation thermal conductance of a blackbody detector of the same dimensions, a crucial feature for future designs of detectors beyond the blackbody radiation limit. Also we see that the simulated detectivity exceeds all other published devices [15, 16, 19, 20]. We have assumed that the 1/f noise of the device is zero due to the thermoelectric readout, and we see Johnson noise limited device performance.

TABLE 3.3: Material constants and calculated device parameters.

Parameter	Design	Hilton Head
$s_{Sb_2Te_3}$	1.65 J/ccK	1.65 J/ccK
$s_{Al_2O_3}$	3.42 J/ccK	3.42 J/ccK
C	6.93x10^{-9} J/W	6.93x10^{-9} J/W
G_{Rad}	3.27x10^{-8} W/K	3.27x10^{-8} W/K
G_{Total}	1.21x10^{-7} W/K	1.20x10^{-7} W/K
τ	56.5ms	56.9ms
$\Re$	5620 V/W	6100 V/W
Johnson Noise	1.83x10^{-8} V/$\sqrt{Hz}$	1.58x10^{-8} V/$\sqrt{Hz}$
TC Noise	9.17x10^{-9} V/$\sqrt{Hz}$	9.87x10^{-9} V/$\sqrt{Hz}$
1/f	0	0
D*	2.74x10^{9}cm$\sqrt{Hz}$/W	3.27x10^{9}cm$\sqrt{Hz}$/W

3.11 Conclusion

Presented in this section is a device design to produce thermopile infrared detectors with performance exceeding all other published works. This design includes a photolithography mask design which is compliant with the fabrication techniques available to us. An optical design has been presented which offers resonant absorption centered at 10μm with a FWHM of 2.1μm which suppressed 75% of the radiation thermal conductance noise and brings the total thermal conductance noise below that of a blackbody detector of the same dimensions. The simulated device shows Johnson noise limited performance with detectivity up to 3.27x10^{9}cm$\sqrt{Hz}$/W.

Chapter 4

MWIR Detection Using Semiconductor Spectrally Selective Absorption

Author's note: This chapter is based largely on the work published in Optics Express [61].

4.1 Introduction

For many decades, the performance limit of thermal infrared detectors has been referenced as the blackbody radiation limit [51, 62, 63]. The objective in uncooled thermal detector design, particularly for imaging, has been to create devices with high absorption in the primary thermal radiation band to maximize sensitivity, without excessively degrading other properties such as the time constant. For example, early thermal detectors were fabricated with high absorption materials to achieve good signals in all spectral ranges, while many modern microbolometers are designed with optical cavity coupling to enhance their signal in the long wave infrared (LWIR) ($\lambda \sim$ 8-12μm) and/or mid wave infrared (MWIR) ($\lambda \sim$ 3-5μm) [64, 65]. Both approaches are focused on optical signal enhancement, which involves normal or nearly-normal incidence light, rather than radiation noise reduction, which involves light incident at all angles.

However, there are many detector applications where the signal of interest either does not lie within the primary thermal emission band or covers only a part of it. For example, any room temperature signal in the MWIR or the 5-8μm water absorption band will lie outside the LWIR primary emission band. A detector designed solely

for high absorption will collect not only the desired signal but also irrelevant signals. Even if there is a hemispherical optical filter to cut out most of the unwanted light, the radiation emission from the detector itself will add greatly to the photon noise in undesired spectral regions.

In this chapter, we describe performance limits for thermal detectors that measure signals that do not include the primary thermal emission band or contain only a part of that band. These devices are composed of materials that do not absorb in the primary emission region, such as semiconductors with bandgap energy greater than the photon energies of the thermal IR. Thermal detectors do not operate based on electron-hole generation and recombination as do photon detectors; therefore, non-crystalline or low-quality semiconductors could be used as well as crystalline ones. To maximize the performance of such detectors, any optical cavity coupling must not only increase absorption of the desired signal but also minimize radiation noise at all angles to the optical axis. For uncooled devices operating at room temperature, the ultimate detectivity in the design band easily exceeds 1.40x10^{10}cmHz$^{1/2}$W^{-1}, which is the traditional blackbody radiation limit for a device with a spherical field of view.

4.2 Theory

Radiation noise serves as the fundamental limit for thermal detector performance. While all other noise sources could potentially be negated by technological and material advancements, the photon fluctuations within the detector due to Planck's law radiation will always be present. Broadband thermal detectors absorb and emit all wavelengths of thermal radiation, leading to a maximum photon noise. Current state-of-the-art thermal detectors operate near this maximum noise either by having high absorption in the peak thermal emission regions or by failing to design the optical properties and cavities of the detector to have very low absorption in this region, particularly off the optical axis, where most radiation interactions occur. For many applications, broadband absorption is not necessary, and a sensor which absorbs outside the primary thermal band is sufficient. These devices will often work with low signals. In order to minimize the photon noise and maximize performance under such conditions, the detector can be composed of materials that do not absorb at the maximum of thermal emission.

Using Planck's radiation formula and assuming that the photons obey Bose-Einstein statistics and the device is acting as a Lambertian emitter, the mean square noise power per unit area per unit noise bandwidth can be written is seen in Equation 4.1,

$$\overline{p_p^2} = 4h^2c^3A \int\limits_{\lambda,\theta,\phi} \frac{\epsilon(\lambda,\theta,\phi)e^{hc/\lambda kT}}{\lambda^6\left[e^{hc/\lambda kT}-1\right]^2} \cos\theta \sin\theta \; d\theta \; d\phi \; d\lambda \tag{4.1}$$

where h is Planck's constant, c is the speed of light, A is the detector area, k is Boltzmann's constant, T is the temperature of the emitting body, and ϵ is the angular and spectral emissivity of the body, with λ being the wavelength of incident photons, θ the polar angle, and ϕ the azimuthal angle. Equation 4.1 is a generalized form of equation 9.107 from [51] to allow for variations in emissivity with angle and wavelength and details on its derivation can be found in Chapter 3. In the case of a radiation noise limited detector, the relationship between noise power and detectivity is given by Equation 4.2.

$$D^*(\lambda) = \frac{\sqrt{A}\epsilon(\lambda)}{\sqrt{2p_p^2}} \tag{4.2}$$

The factor of two in this equation arises from the equivalent photon fluctuations from emission and absorption when the detector is in thermal equilibrium with its surroundings. If we integrate Equation 4.1 over all wavelengths and angles we obtain a blackbody radiation limit of D*=1.98x10^{10}cmHz$^{1/2}$W^{-1} for a hemispherical field of view or D*=1.40x10^{10}cmHz$^{1/2}$W^{-1} over a full sphere at 290K. These values are have traditionally been considered the fundamental limit for thermal detector performance commonly refered to as the blackbody radiation limit [51].

The blackbody radiation limit serves as a fundamental limit only for broadband detectors. The use of spectrally selective materials enables the reduction of photon noise below the blackbody radiation limit. Of great interest for this purpose are semiconductors which primarily absorb photons at energies above their bandgap energy which serves as an absorption cutoff. Figure 4.1 demonstrates this concept by showing the radiation-limited detectivity as a function of cutoff wavelength for an ideal semiconductor. In this approximation the emissivity of the detector is assumed to be unity below the cutoff wavelength and zero above it as shown in the inset of Figure 4.1. We can see in Figure 4.1 that the radiation-limited detectivity for a detector with cutoff wavelength 5μm is 8.26x10^{10}cmHz$^{1/2}$W^{-1}, nearly 6 times the blackbody radiation limit. A device with this cutoff wavelength could be applicable for both MWIR imaging and chemical sensing, particularly for sensing hydrocarbons which have a 3.4μm emission line at room temperature. We can also see that as the cutoff wavelength goes to infinity, the radiation-limited detectivity approaches the blackbody radiation limit. This plot is very similar to that which is used to describe the performance of photon detectors [66], but differs quantitatively in that power fluctuations are being calculated rather than photon number fluctuations.

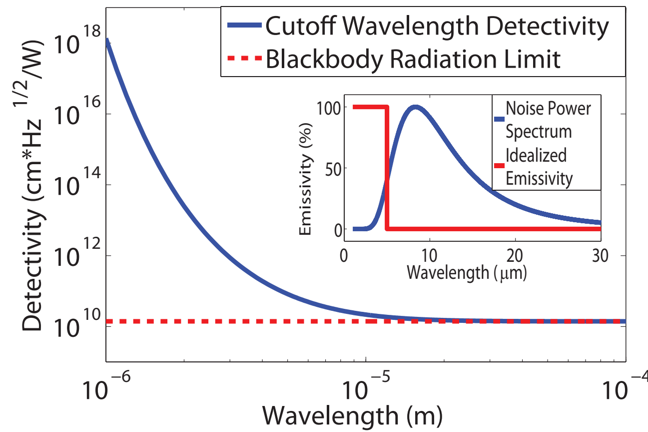

FIGURE 4.1: Detectivity vs cutoff wavelength for a generic semiconductor infrared detector with idealized emissivity shown in the inset.

4.3 Optical Simulation

Optical simulations in this section are done using the optical transfer matrix method described in Section 3.9 of Chapter 3. While there are a variety of narrow bandgap semiconductors which could be used, we have chosen to use PbSe for our simulations. Other options include HgCdTe and InSb based systems, but the higher extinction coefficient of PbSe makes it favorable for thin detectors. PbSe and other lead salts have been used in photoconductive MWIR detectors since World War II. The technology has also been revisited in depth recently [67, 68]. The bandgap energy of .27eV is ideal for our application as it corresponds to a cutoff wavelength of approximately 5μm. The absorption and radiation-limited detectivity at normal incidence of a detector comprised of a single 500nm layer of PbSe can be seen in Figure 4.2. We can see in this figure that the absorption of the detector is around 60% in the MWIR and drops off abruptly at 5μm. The radiation-limited detectivity peaks at 4.84x10^{10} cmHz$^{1/2}$W^{-1} which is hindered significantly by the low absorption of the film due to surface reflection from the high index PbSe detector. While this type of detector is theoretically interesting, it is most likely too thick to be used in a practical device due to large thermal mass. Excess thermal mass in a real detector would lead to either a high thermal time constant or high thermal conductance noise depending on the support structure, which would greatly limit the utility of the detector.

Further optical engineering is necessary to both increase the absorption of the detector and decrease the thermal mass in order to optimize performance. To reduce thermal mass, a much thinner detector must be used. In order to maximize the amount of radiation coupled into a thin detector, optical cavity coupling can be used. The detector itself is highly reflective with PbSe having an index of refraction of 4.52 at 4μm and

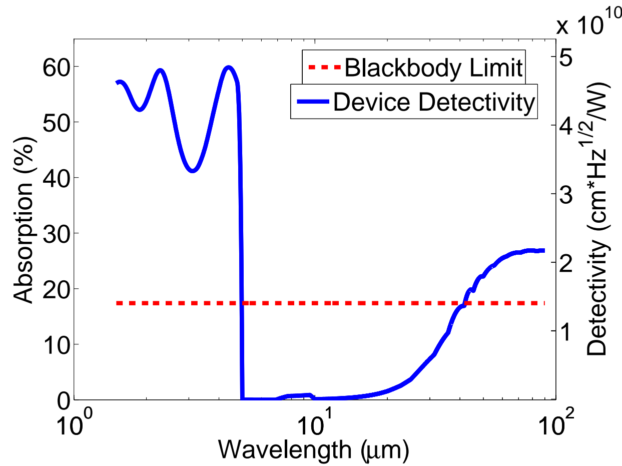

FIGURE 4.2: Absorption (left axis) and radiation limited detectivity (right axis) for a single 500nm thick layer of PbSe.

can be used as a semi-transparent mirror. With a distributed Bragg reflector (DBR) acting as the second mirror, an optical cavity can be formed. We have found that a 1/8th wave cavity offers the best broadband coupling over the full range of the MWIR. The absorption and radiation-limited detectivity of an example device can be seen in Figure 4.3 with the optical layer structure of the device shown in Table 4.1. The mirrors and cavity spacing in Table 4.1 are designed for a center wavelength of 4μm to maximize MWIR coupling. Figure 4.3 shows a peak absorption of 87% corresponding to a radiation-limited detectivity of 1.25×10^{11} cm Hz$^{1/2}$ W^{-1} at 4.3 μm. The average absorption over the MWIR is 64% and the average radiation-limited detectivity is 9.30×10^{10} cm Hz$^{1/2}$ W^{-1} in the MWIR. One simplification should be noted for this calculation. Since our simulations do not allow for the decoupling of absorption within the detector from absorption within the mirrors, the extinction coefficient was assumed to be zero for the mirror materials. This assumption is generally accurate for the DBR materials chosen, but begins to break down around 40μm. However, at this point the photon noise power is about two orders of magnitude below the peak power, so this has little effect on the final simulation result.

4.4 Practical Device Design

The above devices have not assumed any sort of read-out mechanism. Since the vast majority of thermal detectors today are uncooled microbolometers, we will base practical discussion on bolometers. Fortunately PbSe has a favorable temperature coefficient of resistance of -3.45%/K [69] and will be assumed as the temperature sensing material as well as the absorber, with characteristics described later.

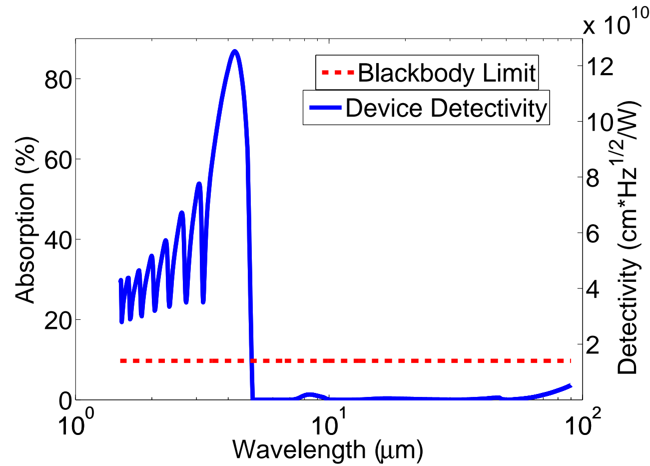

FIGURE 4.3: Absorption (left axis) and radiation limited detectivity (right axis) for the cavity coupled detector described in Table 4.1.

TABLE 4.1: Optical design parameters for an example device.

Material	Index at 4 μm	Thickness (nm)
PbSe	4.52+.8i	45
Vacuum	1	500
Ge	4.03	250
ZnSe	2.43	411
5 more alternating Ge/ZnSe layers		

A single, biased bolometer is susceptible to three significant noise sources, Johnson noise from the thermal excitation of carriers, 1/f noise resulting from a variety of effects in DC biased resistors, and thermal conductance noise resulting from the random fluctuations of energy quanta between the detector plate and its surroundings. This can include both phonon fluctuations through the support structure and photon fluctuations through emission and absorption in the plate. While historically, thermal conductance noise has been dominated by conduction through the legs, recent work has shown that with proper engineering, bolometers can be fabricated for which radiation is the principal thermal conductance path [70]. Though the majority of the calculations are equivalent, there are a few key difference between the noise analysis of thermoelectric detectors presented in Chapter 3 and the resistive bolometers discussed in this chapter. The first is the responsivity is defined as $\Re = \alpha V_b/G$ where α is the temperature coefficient of resistance (TCR) of the readout resistor and V_b is the bias voltage applied to the resistor and bias resistance is ignored. The other difference is that since a resistive bolometer requires bias voltage, 1/f noise cannot be ignored, and more attention must be paid to

the measurement scheme as our device noise will be frequency dependent.

In order to demonstrate the utility of this technology for various applications, two device designs will be presented. One focuses on maximizing detectivity at the expense of increased thermal time constant, the other focuses on low thermal time constant, therefore increasing the thermal conductance noise and decreasing detectivity. Necessary material parameters for these calculations were found in [60]. Both devices use the same layer structure as shown in Table 4.1. However, the 1/f noise parameter of PbSe was not found in literature, so the k_m of vanadium oxide of 10^{-13} [52], a common microbolometer resistor material is used. If 1/f noise in PbSe proves to be an issue in processing, a small, electrically isolated vanadium oxide resistor could be placed on the peripheral regions of the detector plate without significant effects on the optical properties of the device. Equivalently, a thin vanadium oxide layer could be placed uniformly over the entire detector with only minor modifications to the bottom mirror. Other assumptions include a bias voltage of .1V, a device resistance of 100kΩ, and a device and heat sink temperature of 290K, all of which agree with our preliminary testing. Both devices are designed with legs 500μm in length, made of nickel iron and alumina with thicknesses of 200$\AA$ and 100$\AA$ respectively. The devices are assumed to be operated in chopping mode and measured every frame such that the bias is applied during one half of the frame, where $f_1=1/2\pi\tau$ and $f_2=1/\pi\tau$. All other design parameters as well as noise calculation results can be seen in Table 4.2. The detectivity as a function of wavelength can be seen in Figure 4.4. Note that Figure 4.4 is a close up view of the detectivity in the MWIR as this is our region of interest. The devices are optically identical to those modeled in Figure 4.3 so the spectrum applies to these devices as well, with the only change being the scaling of the y-axis due to the addition of other noise terms.

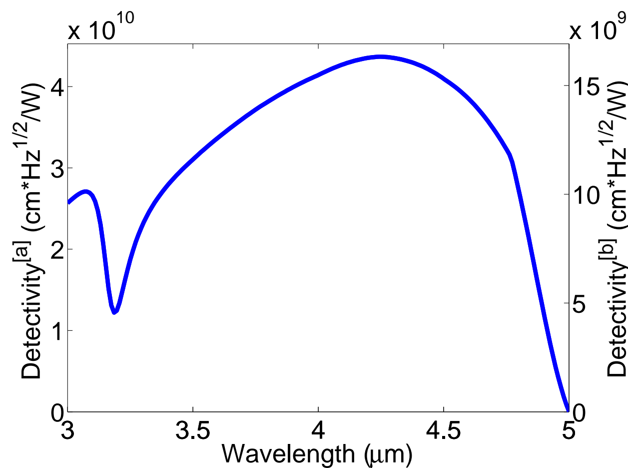

FIGURE 4.4: Detectivity vs wavelength of for the high detectivity [a] and low thermal time constant [b] device designs.

Table 4.2: Device design parameters, calculated thermal properties, and calculated noise levels for two example devices

Parameter	Low τ Device	High D* Device
Plate Area	$(30\mu m)^2$	$(175\mu m)^2$
Leg Al_2O_3 Width	$1.5\mu m$	$5\mu m$
Leg NiFe Width	$1\mu m$	$3\mu m$
G (W/K)	3.11×10^9	1.25×10^8
C (J/K)	5.75×10^{11}	1.96×10^9
τ (ms)	18.5	157
NEP Johnson (W)	1.06×10^{-13}	1.46×10^{-13}
NEP 1/f (W)	2.37×10^{-14}	9.53×10^{-14}
NEP Thermal Conductance (W)	4.42×10^{-13}	3.04×10^{-13}
D* (cm*Hz$^{1/2}$/W)	1.68×10^{10}	4.37×10^{10}

We can see in Table 4.2 that the performance of the low τ device is limited by thermal conductance noise, primarily from thermal conductance through the legs, but it still demonstrates peak detectivity higher than the blackbody radiation limit of a detector with spherical field of view, which is the basis for all current thermal detector theory. The thermal time constant of this device τ=18.5ms is sufficient for video frame rate operation which is required for many applications [52]. The high detectivity device exhibits much better performance and could be used in many non-video applications such as chemical sensing. Through proper optical design, support structure engineering, and fabrication methods, devices of this nature can be tailored to fit specific applications with performance equal to or greater than that presented above.

4.5 Spectral Selectivity using Plasmonic Structures

Plasmonic structures offer an alternative means of achieving the spectral selectivity necessary to produce MWIR detectors operating beyond the blackbody radiation limit. Enhanced transmission through arrays of subwavelength metal nanoslits has been experimentally demonstrated [71]. In order to exploit this phenomenon, the radiation transmitted through the array must be coupled into an absorbing material forming a spectrally selective bolometer. Consider an array of nanoslits patterned as seen in the

inset of Figure 4.5. The nanoslits are patterned in a 100nm thick silver layer on a 400nm thick polyethylene microbolometer which is then suspended over a gold mirror by a 1μm air gap. Using standard FDTD simulation methods, and optical constants from [58, 72] we can simulate the absorption spectrum of p polarized radiation for this structure as seen in Figure 4.5. This figure shows two narrowly spaced absorption peaks, one at 3.5μm which corresponds to the peak plasmon resonance, and one at 3.4μm corresponding to the absorption peak of polyethylene which falls within the plasmon resonance. While this simulation method does not lend itself to full device performance analysis, we can clearly see that this type of plasmonic structure could also be used to produce MWIR microbolometers whose radiation noise properties have been manipulated in either wavelength and/or polarization.

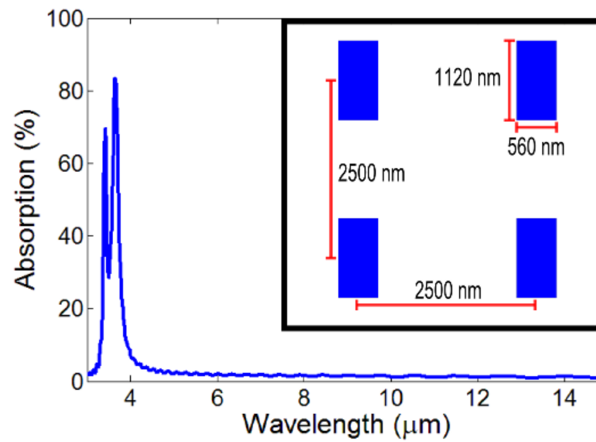

Figure 4.5: Absorption vs wavelength and structural layout (inset) for plasmonic selective absorption.

Chapter 5

Analysis of radiation thermal conductance in microstructures.

Author's note: This chapter is based largely on the work presented at the International Conference of Thermoelectrics in 2012 and published in the Journal of Electronic Materials [73].

5.1 Introduction

As the scaling of thermoelectric coolers progresses from the cooling of entire modules to individual electronic devices, the surface-area-to-volume ratio of the thermoelectric and supporting films increases drastically. In addition, the allowable power draw for micro-coolers will drop rapidly with size. In order to minimize power consumption, film thicknesses must be reduced and thermal isolation increased to maximize cooling. Microcoolers are affected by four main thermal transport mechanisms: material thermal conduction through the thermoelectric films and support structure, thermal conduction through air, the convection of air near the cooler, and radiation. Material thermal conduction is a fundamental loss source for thermoelectric coolers. This source can be minimized by material advancements and is vital to the figure of merit of thermoelectric materials. Conduction through air is not a fundamental process because it can be eliminated through vacuum packaging, a common technique used in infrared imaging and some other electronic technologies. Convection plays a very minor role on the micro scale and can also be eliminated using vacuum packaging. Radiation is a fundamental thermal conductance path for all devices, but in the analysis of current state-of-the-art microcoolers it has been ignored as the surface-area-to-volume-ratio of the devices is not high enough for radiation to be significant. In very small micro-coolers that are

designed to minimize power consumption, radiation thermal transport becomes a source of loss that must be addressed. We first present a theoretical analysis of micro-cooler performance including radiation transport. An analysis of the power transfer mechanisms of a thermally isolated device allows for the fitting of separate coefficients related to film and radiation power transfer. From these coefficients we are able to calculate the contributions of both radiation and film thermal conduction of a device at a given temperature. This leads to a modified temperature dependence in the thermoelectric figure of merit, Z, and therefore an added temperature dependence in the analysis of the maximum cooling of a microcooler. To verify our theory, we have fabricated microcoolers on a scale where radiation thermal conductance is significant. These devices are then characterized using a microheater integrated into the same thermal isolation structure and fit to our theoretical model. From this fit we are able to estimate both the radiation contribution to thermal conductance of the devices and their emissivity. While the focus of this chapter is the application of this theory to microcoolers, it is applicable to any thermal isolation structure with an integrated microheater as will be demonstrated in the thermal conductivity measurements in Chapter 7.

5.2 Background

Thermal radiation theory and thermal transport due to radiation has been widely studied and well described by those in the thermal detector field [51, 52] and described in the theoretical analysis of device performance limits of micro-coolers [74–77]. However, in the analysis of fabricated coolers, the effects of radiation thermal transport have been dismissed as insignificant due to device geometry [49, 78, 79]. The radiated power of a blackbody flat plate is given by the Stephan-Boltzman Law in Equation 5.1,

$$P = A\epsilon\sigma_b T^4 \tag{5.1}$$

where P is the emitted power, A is the emitting area, ϵ is the emissivity, σ_b is the Stephan-Boltzman constant, and T is the absolute temperature of the device. In the case of a thin membrane micro-cooler, it is more convenient to treat the surface area as approximately $2A$, where A is the area of only one side of the plate.

The ultimate performance of thermoelectric coolers, the maximum temperature difference between the cooled plate and the heat sink, is defined in Equation 5.2,

$$(T_2 - T_1)_{max} = \frac{(S_p - S_n)^2 T_1^2}{2GR} \tag{5.2}$$

where T_2 and T_1 are the hot junction and cold junction temperatures respectively, S_n and S_p are the Seebeck coefficients of the n-type and p-type semiconductors, G is the total thermal conductance of the thermoelectric and structural thin films including radiation, and R is the total device resistance [24]. The factor of two in the denominator stems from the assumption that half of the Joule heating in the thermoelectric legs ends up in the thermal isolation structure and half in the substrate, which is a common assumption in microcooler theory [24]. It is plain from Equation 5.2 that radiation thermal conduction directly contributes to cooler loss and reduces maximum cooling. In this treatment, radiation effects are lumped into an effective thermal conductance term that combines both traditional thermal conductance and radiation effects.

To create a model for microcoolers with significant radiation contributions, we first look to the power balance equation of a released microstructure in vacuum in Equation 5.3,

$$P_{in} = G_0 \Delta T + 2A\epsilon\sigma_b(T_0 + \Delta T)^4 - 2A\epsilon\sigma_b T_0^4 \tag{5.3}$$

where G_0 is the thermal conductance of the support structure and thermoelectric films, ΔT is the temperature change of the thermal isolation structure, T_0 is the base temperature (assumed to be 300K), and the remaining symbols are defined following Equation 5.1. The $K_0\Delta T$ term represents the power flow via the thermoelectric films and support structure, the $2A\epsilon\sigma(T_0 + \Delta T)^4$ term represents power emitted via radiation thermal conduction, and the $2A\epsilon\sigma T_0^4$ term represents the power absorbed by the device that is being emitted by its surroundings, which are assumed to be at T_0. We can see from this equation that the response of a device to induced power will be linear if dominated by thermal conduction through the material, have a T^4 dependence if dominated by radiation thermal conductance, and have a combination of T and T^4 terms if both contribute significantly. A plot of these three scenarios can be seen in Figure 5.1. This plot shows the calculated P vs ΔT response of a generic device having a total thermal conductance of 5x10^{-7} W/K at room temperature with no radiation contribution, a 50/50 split of radiation and film thermal conductance, and purely radiation limited heat transfer. From this Figure 5.1 we can see that the shape of the response of a device to input power indicates which thermal conduction mechanisms are present.

By introducing power onto the thermal isolation structure of a device, in our case by sourcing a current through a resistor on the device, one can estimate the contributions of both radiation and material thermal conduction using a polynomial fit of the P=I^2R vs ΔT plot using only the fourth-order and linear terms to obtain fitting coefficients B and C, where B=K_0 and C=$2A\epsilon\sigma$ so Equation 5.3 becomes Equation 5.4.

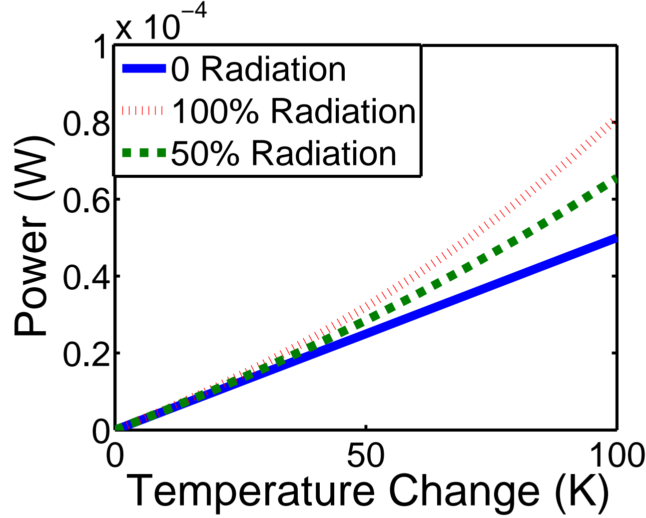

FIGURE 5.1: Simulation of temperature response to input power of a generic thermal isolation structure with thermal conductance having no radiation contribution, 50% radiation contribution, and 100% radiation contribution.

$$P = B\Delta T + C(T_0 + \Delta T)^4 - C\Delta T_0^4. \tag{5.4}$$

To calculate the contribution of each conduction path to overall thermal conduction, we take the derivative of Equation 5.4 to obtain Equation 5.5,

$$\frac{dP}{d\Delta T} = B + 4C(T_0 + \Delta T)^3 \tag{5.5}$$

where $dP/d\Delta T$ is the total thermal conductance, B and C are the fitting parameters previously described, and T_0 and ΔT are the equilibrium temperature and change in temperature respectively. Equation 5.5 describes a device with thermal conduction consisting of a term that is constant with temperature resulting from the thermal conductance through the thermoelectric films and support structure and a term that increases cubically with temperature change from radiation thermal conduction. An example of this behavior using the same theoretical device and scenarios used in Figure 5.1 can be seen in Figure 5.2.

5.3 Fabrication

To investigate our theory, ultra-small micro coolers have been fabricated with a micro-heater on the thermally isolated plate connected to the cold side of the thermoelectric junction as shown in Figure 5.3. The fabrication process consists of a variety

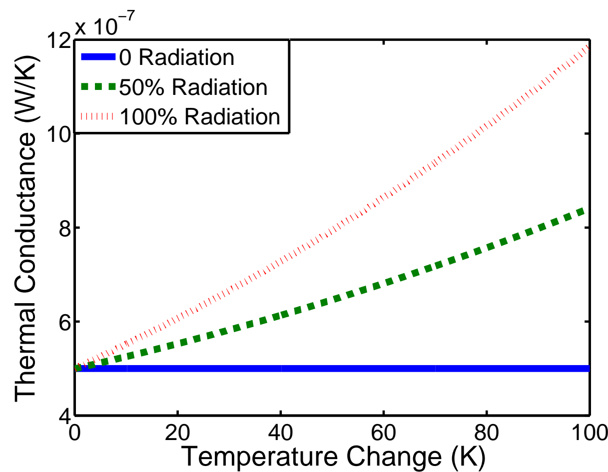

FIGURE 5.2: Simulation of thermal conductance vs input power of a generic thermal isolation structure with thermal conductance having no radiation contribution, 50% radiation contribution, and 100% radiation contribution.

of surface and bulk micromachining techniques. A silicon wafer is coated on both sides with a 200nm film of Low Pressure Chemical Vapor Deposited (LPCVD) low-stress silicon nitride to provide electrical insulation between device and substrate. The film is removed from the back side of the wafer using a CF_4/O_2 plasma etch. The wafer is then coated on both sides with a 25nm film of Atomic Layer Deposited (ALD) Al_2O_3 which acts as a structural layer and etch stop for the released devices. Next a 15nm electron beam evaporated Ni film is deposited to form the micro-heater and a 5nm/10nm Ti/Pt layer is deposited to form the interconnects between the thermoelectric materials. A 15nm/185nm Cr/Au layer is deposited to form bond pads for wire bonding. The thermoelectric materials are deposited via RF magnetron co-sputtering from targets consisting of the pure base elements. The thermoelectric films used are n-type Bi_2Te_3 and p-type Sb_2Te_3. They are sputtered onto substrates heated to 260°C for Bi_2Te_3 and 230°C for Sb_2Te_3. Further details on the deposition and thermoelectric properties of these films can be found in [55]. All of the metal and thermoelectric films are patterned using a lift-off technique. The devices are then encapsulated with a 25nm thick layer of ALD Al_2O_3 which is patterned using a BCl_3 plasma etch. The front side of the wafer is patterned to form the thermal isolation structure of the device, while the back side is patterned to define the etch pits for backside etching. Finally, the devices are released using a through-wafer Bosch etch to remove all of the Si and LPCVD Silicon Nitride underneath the device. The result is a free standing structure composed of a thermoelectric junction with the cold junction lying on the same thermally isolated plate as a micro-heater. A SEM micrograph of one of the released devices can be seen in Figure 5.4.

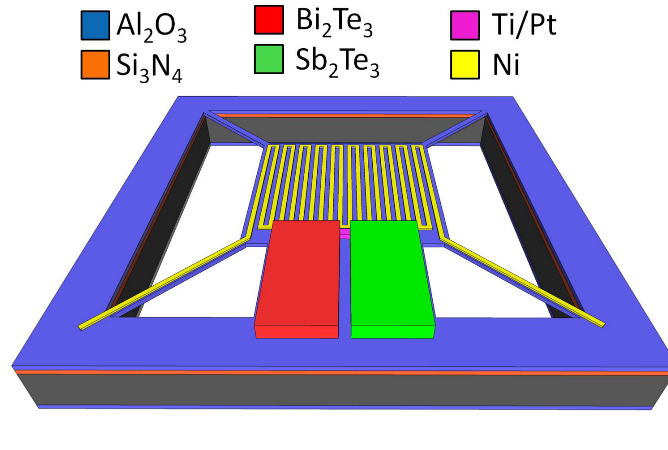

FIGURE 5.3: Concept image of fabricated microcoolers showing film layout and materials used.

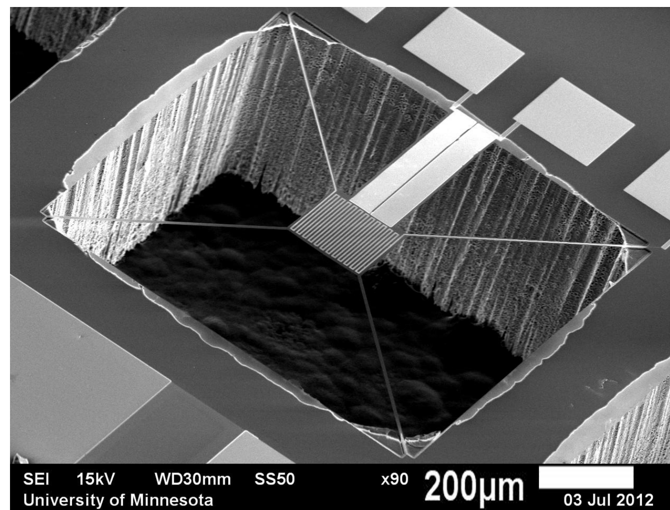

FIGURE 5.4: SEM micrograph of a released microcooler.

5.4 Experiment

Before the released devices can be characterized, the temperature coefficient of resistance of the Ni film in the microheater must be characterized. This is done by placing an unreleased device on a macro-scale thermoelectric heater/cooler and contacting the bond pads of the resistor using probe tips. The temperature of the device is then cycled between 20°C and 60°C while the resistance is measured, leaving ample time for thermal equilibrium to be reached at each measurement point. The average Ni TCR value over several devices was .31%/K. The experimental technique is described in full in Section 7.2.1.

Two different device geometries were tested. Both had 200μm x 200μm center plates with different sized etch pits. The short legged devices have 600μm x 600μm

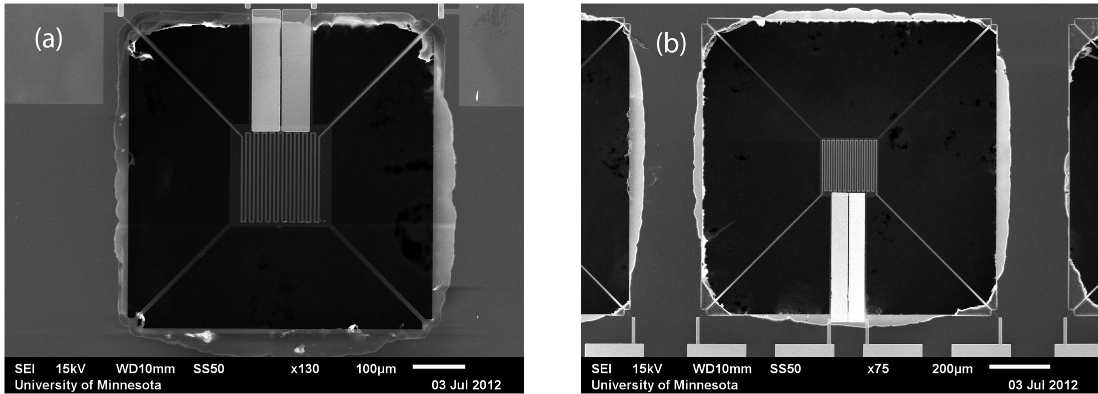

FIGURE 5.5: SEM micrograph of the 'small hole' microcooler (a) and the 'large hole' microcooler (b).

etch pits resulting in a thermoelectric leg length of 200μm and the long legged devices have etch pits of 1000μm x 1000μm resulting in a thermoelectric leg length of 400μm. Figure 5.5 shows an SEM micrograph of both geometries. The devices are packaged and wire bonded to be tested in vacuum to eliminate thermal conduction and convection through air. A varying current is sourced through the micro-heater while its resistance is monitored. From the resistance values and the measured TCR we can calculate the temperature change, ΔT, of the device at a given sourced power. We can then plot I^2R vs. ΔT and fit the curve using the fourth-order and linear terms described in Equation 5.4. From this fit we are able to obtain fitting coefficients B and C as described in the theory section. The calculated values for B and C were 4.2x10^{-7} W/K and 6.6x10^{-16} W/K^4 respectively for the short legged geometry, and 3.3x10^{-7} W/K and 1.05x10^{-15} W/K^4 for the long legged geometry. The I^2R vs. ΔT data and polynomial fits for both geometries can be seen in Figure 5.6. In this figure we can see a stronger T^4 contribution in the longer legged devices. This is expected since these devices have a larger emitting area and lower film thermal conductance due to longer legs, as the film thermal conductance is inversely related to leg length.

Using the calculated fitting coefficients B and C and Equation 5.5, we are able to calculate the contribution of radiation thermal conductance to the total thermal conductance of each device geometry. The results are shown in Figure 5.7. Here we see the total thermal conductance, as well as the contributions of radiation and film thermal conductance for both device geometries. The short legged devices show a 15% radiation contribution to total thermal conductance at room temperature while the long leg devices show a 26% radiation contribution at room temperature.

The maximum cooling of the devices is measured by sourcing a varying current through the thermoelectric films while measuring the resistance of the Ni resistor. This test is again done on wire bonded samples in vacuum to eliminate losses from air. The

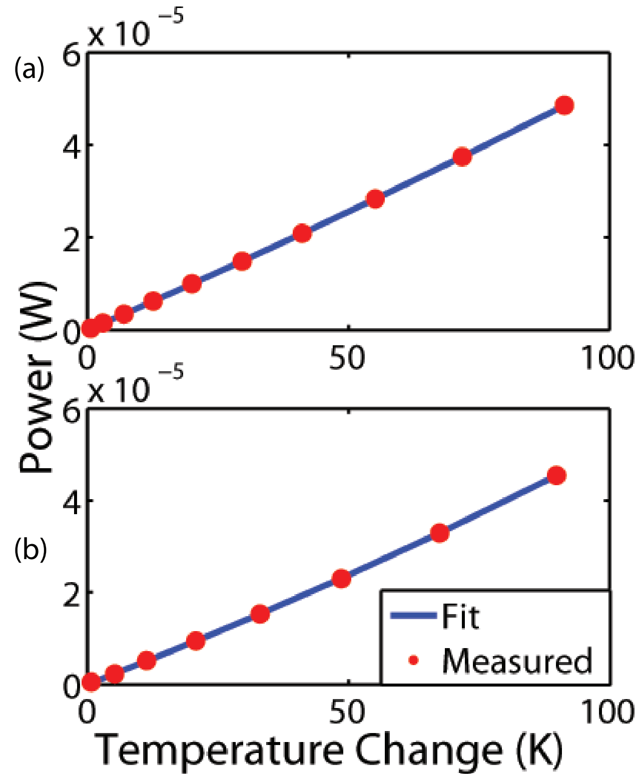

FIGURE 5.6: Input power vs temperature change data and fit for 'small hole' micro-cooler (a) and the 'large hole" microcooler (b).

cooling is then easily calculated using the previously measured TCR of the Ni films. The total cooling vs. input current of both geometries can be seen in Figure 5.8. We see a maximum cooling of 3.1K in the short legged devices and 2.6K in the long legged devices. Due to various complications, the resistance of the thermoelectric films in the specific devices from this test was not measured but numerous devices from the same wafer using the same process and geometry were measured all having resistance below 1500Ω for the long legged devices and 1000Ω for the short legged devices so we can estimate that the power consumption at maximum cooling of these devices is below 5μW in both cases.

To provide an extreme example of radiation thermal conduction in a micro-cooler, we have analyzed a test structure like that seen in Figure 5.9. This device has a much larger emissive area than the previously described devices and will therefore have a much larger radiation contribution to thermal conduction. The device was characterized as previously described and the best fit obtained for the I^2R vs. ΔT data is a purely fourth-order fit with fitting coefficients B=0 W/K and C=9.7x10-15 W/K^4, which is plotted in Figure 5.10. This indicates that radiation is the dominant thermal conduction path in such a device.

Using the fitting coefficients obtained earlier we can estimate the emissivity values of

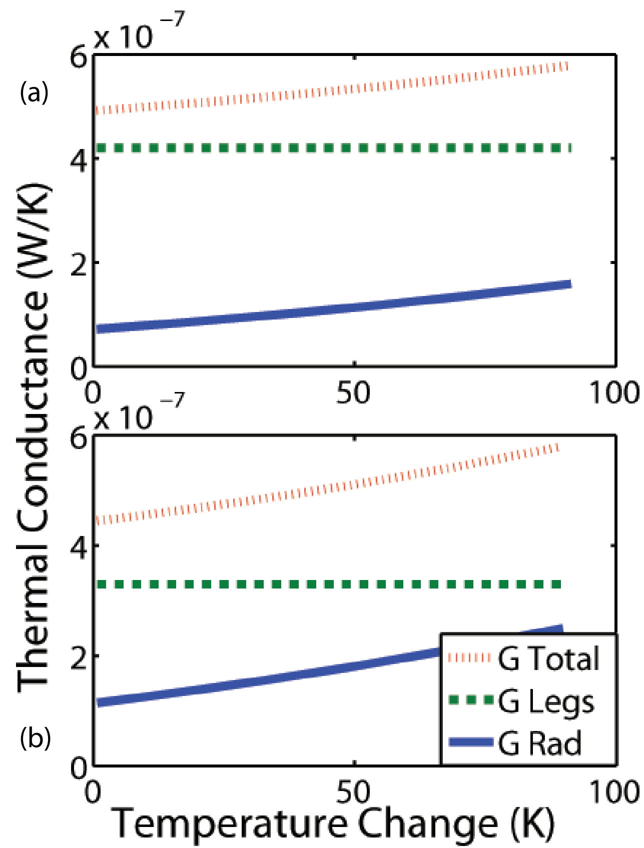

FIGURE 5.7: Thermal conductance vs temperature change contribution of each thermal conductance source for 'small hole' microcooler (a) and the 'large hole' microcooler (b).

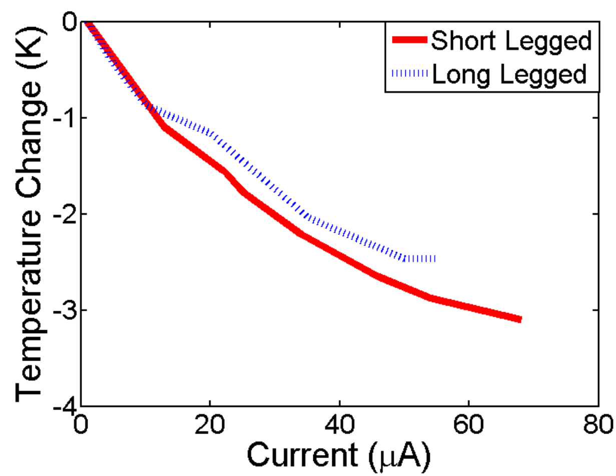

FIGURE 5.8: Temperature change vs input power of microcoolers.

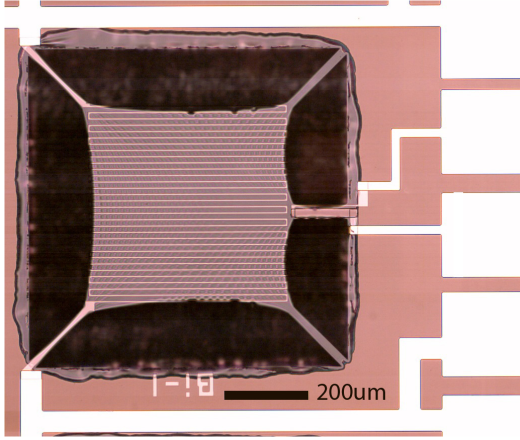

FIGURE 5.9: Microscope image of a radiation limited microcooler..

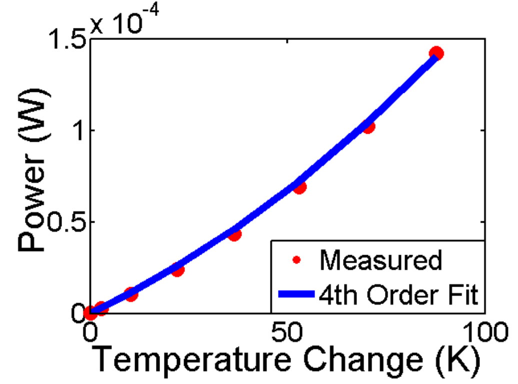

FIGURE 5.10: Input power vs temperature change data (red) with purely fourth order fit (blue).

the device by taking advantage of the two different geometries and emissive areas. The plate consists of a 50nm thick layer of Al_2O_3 encapsulating a 15nm Ni layer patterned in periodic 3μm wide lines with 3μm spacing. We expect this to have a much different emissivity than the thermoelectric films which consist of approximately 250nm thick Bi_2Te_3 and Sb_2Te_3 films encapsulated with 50nm of Al_2O_3. We have assumed that half of the area of the thermoelectric films contributes to radiation thermal conduction. This is much like the assumption made in calculating the Joule heating of a thermoelectric cooler, where half of the Joule heating power is assumed to affect the cold junction, while the other half flows to the heat sink. This is perhaps an oversimplification since radiation thermal conduction is temperature dependent and a more thurough analysis would consider the temperature gradient across this film, but we feel this assumption allows for a reasonable estimate of emissivity. We then have the pair of Equations 5.6 and 5.7,

$$A_1\epsilon_1 + A_2\epsilon_2 = C_1/2\sigma_b \tag{5.6}$$

$$A_1\epsilon_1 + A_3\epsilon_2 = C_2/2\sigma_b \tag{5.7}$$

where A_1 is the plate area, A_2 and A_3 are the areas of the thermoelectric films in the short and long legged devices respectively, ϵ_1 and ϵ_2 are the emissivities of the corresponding areas, and C_1 and C_2 are the fitting coefficients previously described in Equation 5.4. Solving this set of equations for the two unknowns, ϵ_1 and ϵ_2, we obtain values of ϵ=.06 for the plate and ϵ=.32 for the thermoelectric films. These values are lower than the emissivity measured using Fourier Transform Infrared (FTIR)

microscopy, but emissivity obtained using this technique are limited to normal incidence, which will not reveal variable emissivity with angle due to interference effects in the grating-like center structure and cannot distinguish absorption from scattering, leading to significant error. The FTIR measurement did however reveal a higher emissivity in the thermoelectric films, which agrees with the calculation. It should be noted that the long and short legged devices come from two different wafers using the same fabrication method but with slightly different sputtering power, less than 5% difference, for the thermoelectric films. This will lead to slightly different film thickness and composition so the assumption that ϵ_2 is equivalent on both devices may not be ideal, but still serves to provide a reasonable estimate of emissivity.

The reader will notice that we have assumed that the film thermal conductivity (κ) is constant with temperature in the temperature range of interest. While it is difficult to measure the dependence of our film thermal conductivity on temperature using the techniques of this chapter, we were able to estimate the dependence using a few sources which have studied similar materials. We take a linear fit of published data on sputtered Al_2O_3 on Si [80] and hot pressed nano-powders of BiSbTe [81] to obtain a slope of -.0016 W/m-K^2 for the thermoelectric films and .0024 W/m-K^2 for Al_2O_3 over the 25-100°C range. We use measured room temperature thermal conductivity values of κ=2.6 W/m-K for Al_2O_3 [56] and κ=1 W/m-K for Bi_2Te_3 and Sb_2Te_3 [55] as well as our device geometry to estimate a 60% contribution for Bi_2Te_3 and Sb_2Te_3 and a 40% contribution from Al_2O_3 to total film thermal conductivity in our device. With these estimates the temperature dependence of the film thermal conductivities cancels (.6*-.0016+.4*.0024=0) which leads us to believe that the assumption of temperature-independent thermal conductivity is reasonable for our devices. If a $\kappa(T)$ is known, the model can easily be amended by replacing K_0 with $\kappa(T)A/L$ and taking the derivative accordingly.

5.5 Conclusion

A theoretical analysis of microcoolers having significant radiation thermal conductance has been provided. We have shown how such devices can be characterized in order to analyze the effects of radiation thermal conduction. We have fabricated devices on a scale where radiation thermal conduction contributes 15%, 26%, and 100% of the total thermal conduction of the device depending on geometry.

Chapter 6

Detector Fabrication

6.1 Introduction

This section is intended to give step by step instructions on how to fabricate spectrally selective uncooled infrared thermopile detectors. Many difficult engineering challenges have been addressed and many of the potential pitfalls of the fabrication process are covered. The process involves three dies, the detector itself, the micropillar with micromirror, and the microaperture. Detector die fabrication involves a series of surface micromachining steps before patterning a backside hard mask and removing the underlying silicon with a through wafer etch. The micropillars are formed by fabricating silicon on insulator (SOI) wafers in house with the device wafer being of the same thickness as the detector wafer. The SOI wafer is then patterned and the device wafer etch, stopping on the buried oxide to form micropillars which are then coated with a highly reflective layer. Microapertures are fabricated by patterning an Al_2O_3 hard mask on a thin Si wafer before etching through the wafer to form an aperture.

6.2 Standard Processes

This section is intended to outline some of the standard steps that are repeated throughout the process so that they may be easily referenced in future sections. These are typically photolithography and clean steps.

6.2.1 Solvent Clean

At many times throughout the process the wafer will need to be cleaned in order remove residue from previous processing steps. This involves subsequent 5 minute soaks

in acetone, methanol, and isopropyl alcohol (IPA) followed by a water rinse and nitrogen dry. This is most easily accomplished using the solvent tanks located in Bay 2.

6.2.2 1805 Lithography

Shipley Microposit S1805 photo resist (1805) is used as a soft mask in wet etch processes. It is also used as the patterning resist for lift off processes, but this will be discussed in Section 6.2.4. Wafers are pre-baked for at least one minute on a hot plate at 120°C. To promote adhesion, a coating of hexamethyldisilazane (HMDS) is necessary. This coating can either be applied by spinning on liquid HMDS at 3000rpm for 30s or by vapor coating for one minute in the vapor tank provided in the Bay 2 wet bench. The 1805 resist is then spun on at 3000rpm for 30s. The resist is then soft baked at 105°C for 60s. The wafer can then be aligned and exposed in a Karl Suss contact aligner. An exposure time of 2.5s has produced the best results. The resist is developed in 5:1 mixture of water and Shipley Microposit 351 (351) developer for 12s. After rinsing in water for 60s and drying with a nitrogen gun the resist is hard baked at 120°C for 60s. After processing is finished the resist is stripped with a solvent clean followed by a spin rinse and dry.

6.2.3 1813 Lithography

Shipley Microposit S1813 photo resist (1813) is used as a soft mask for front side plasma etching. The additional thickness of this resist compared to 1805 provide for better step coverage when using thicker features like those on the front side of the wafer. The process is identical to that outlined in Section 6.2.2 but with an exposure time of 6s and a develop time of 30s.

6.2.4 Lift Off Lithography

Lift off lithography is used to pattern many of the metalization steps throughout the process. Lift off lithography is often preferable to etching because it produces clean, well-defined lines without the need for selective etching. The resist of choice is MicroChem lift-off resist 3A (LOR 3A) because it patterns easily and holds up well at high substrate temperatures. Since the film thickness of many of the metalization steps is on the same order of the thickness of this resist (300nm), a multi-layer lift-off structure may be necessary. It is vital that the wafer be both clean and dry before lift-off lithography to ensure adhesion, so lift-off lithography should be preceded by a solvent clean and pre-bake at 170°C for 300s. After allowing the wafer to cool for 60s, the resist is spun

on for 30s at 3000rpm. The resist is soft baked at 170°C for 60 seconds. In the case of multi-layer lift-off processing, the cool, spin-on, and soft-bake are repeated. We use 1805 as the patterning resist for LOR 3A. It is spun on and patterned almost identically to the process described in Section 6.2.2 with the exception being a soft bake temperature of 90°C. After the 1805 is developed, the LOR 3A is etched using Shipley Microposit MF CD-26 Developer (CD-26). This is most easily done with a spin developer. The wafer is spun at 500rpm while CD-26 is sprayed on. The development time varies with thickness, but a 15s development has been used for a single 300nm layer. As a general rule 15s of development is required per layer of LOR. The wafer is then water rinsed and dried, no hard bake is needed. After film deposition the lift-off is completed using Shipley Microposit Remover 1165 (1165) heated to 60°C. The time for lift-off to complete varies greatly with film thickness and composition. After lift-off, the wafer should be soaked in IPA for at least 300s and then rinsed in water.

6.3 Detector Fabrication

Fabrication of the thermopile detector die is by far the most complex and challenging portion of the process. It involves a seven mask process with ten deposition steps and two etch steps in a surface micromachining process before the final, bulk micromachining, etch release which removes the silicon beneath the detector. This section will give step by step instructions on the fabrication of the detector die with the hopes that future researchers will be able use it as a guide to fabricate these or similar structures.

6.3.1 Electrical Insulation

Device processing starts with thin (250μm) double-side-polished silicon wafers. These wafers are coated with low pressure chemical vapor deposition (LPCVD) low stress silicon nitride. The thickness of this layer has previously been varied between 100nm and 270nm over various process runs and the thickness of this layer does not seem to have any impact on device fabrication or performance. The purpose of this layer is both electrical insulation, to insulate the devices from the substrate, as well as to prevent electrical shorting during wire bonding. Early process runs done without this layer showed a large fraction (>50%) of wire bonded devices shorted to the substrate. This problem can also be avoided by tack bonding the devices. Tack bonding involves physically pressing the bond wire into the bond pad to create electrical contact. This avoids the ultrasonic agitation of standard wire bonding and in practice has prevented the shorting issue. This fabrication step is shown in Figure 6.1

6.3.2 Aluminum Oxide Structural Layer

The wafer is then coated on both sides with a layer of atomic layer deposition (ALD) Al_2O_3. The wafer should be propped up with glass slides along the edges in order to promote uniform coating of the back side. Using the standard recipe at 250°C, 200 cycles produces a film that is about 22nm thick. This film serves multiple purposes, electrical insulation, structural layer, etch stop, and backside hard mask. The 22nm film serves as a sufficient insulator between devices and substrate, but as mentioned previously, is susceptible to shorting to substrate during wire bonding. This film also makes an excellent structural layer because it is highly tensile stressed. Tensile stress is vital to ensuring that the device is sufficiently flat for integration into an optical cavity. It is also extremely resistant to plasma etches, specifically the deep reactive ion etch (DRIE) Bosch process etch, O_2 plasma, and SF_6 plasma, which are the three etches used in the process not intended to etch Al_2O_3. In preliminary testing the etch rate of ALD Al_2O_3 in the DRIE Bosch process etch was measured to be 1.7nm/hr. Finally, because of its resistance to the DRIE Bosch process etch, the ALD Al_2O_3 layer also serves as a hard mask on the back side of the wafer for the final etch release process. A model of the wafer after SiN_x and ALD Al_2O_3 deposition can be seen in Figure 6.2.

FIGURE 6.1: Model of wafer coated with LPCVD SiN_x (pink).

FIGURE 6.2: Model of wafer after ALD Al_2O_3 deposition (tan).

6.3.3 Optical Film Deposition

The optical thin film stack is deposited using DC magnetron sputtering. The stack includes a 300nm thick Ge mirror layer and a 3nm thick Ni absorber layer. These films are patterned using lift off lithography. Since the film thickness is on the order of a single layer of LOR 3A, the lift off resist must be thickened either by using a dual layer LOR 3A process or by reducing the spin speed to 1500rpm during LOR 3A spin on. The substrate is heated to 200°C during deposition to promote adhesion. The Ge films are deposited at a pressure of 5mT in Ar with a sputtering power of 150W. The deposition rate was measured in previous process runs at this power and found to be 15nm/min so a 300nm film is deposited in 20 minutes. The 3nm thick Ni layer is deposited at a

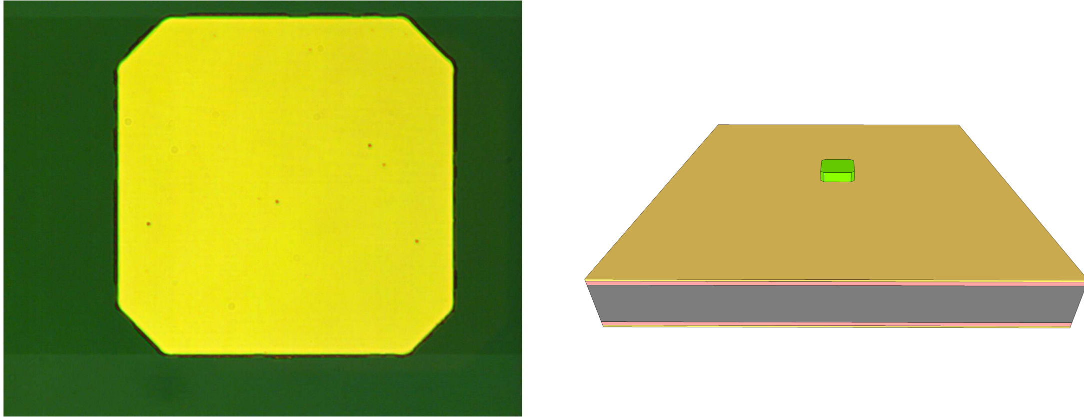

FIGURE 6.3: Optical microscope image and model image of fabrication progress after optical stack deposition (green).

pressure of 5mT in Ar with a sputtering power of 175W. A 25s deposition run yields a film that is approximately 3nm thick. It is very difficult to measure films this thin, so this film thickness is estimated from previous calibration runs of thicker films. The Ge films are fairly brittle so lift off occurs in around 10 minutes. An optical microscope image and model image of the released optical absorber/reflector layer can be seen in Figure 6.3. Because this is a fairly thick layer of sputtered material that is susceptible to many processing techniques, there are some potential pitfalls that can occur with this process which will be discussed next.

6.3.3.1 Ge damage from solvents

Over the course of our fabrication runs, it was found that Ge is very susceptible to damage from solvents and even water. Because of this, exposure of the optical stack to liquids should be minimized before encapsulation. An example of the damage caused to the Ge films by prolonged exposure to 1165 can be seen in Figure 6.4. If we compare this to Figure 6.3 we see that the film no longer looks metallic, but dulled with a concentration of damage near the thermoelectric junctions. In order to prevent this, the films should be exposed to only a short lift-off and rinse before encapsulation. To ensure fast lift-off, a LOR 3A layer much thicker than the Ge layer should be used and unlike most LOR steps, only a short spray rinse with IPA and water should be used after lift-off.

6.3.3.2 Material Overhang

When using a multilayer LOR 3A process with the optical stack, a material overhang layer can develop as seen in Figure 6.5. Since these structures extend beyond the dimensions defined by lithography. This layer has a very tight alignment tolerance with the final Al_2O_3 encapsulation layer so this cannot be allowed to persist through to the end of the process. A simple way to remove this feature is to immerse the wafer in 1165 and subject it to ultrasonic agitation. However, since the film has very poor adhesion, too much time or too high of power during agitation will cause the film to become damaged. This damage is evident as notches missing from the edge of the patterned features. To prevent this, the ultrasonic agitation is done at minimum powers in 60s intervals, inspecting every minute to note the progress of the overhang removal and check for signs of damage.

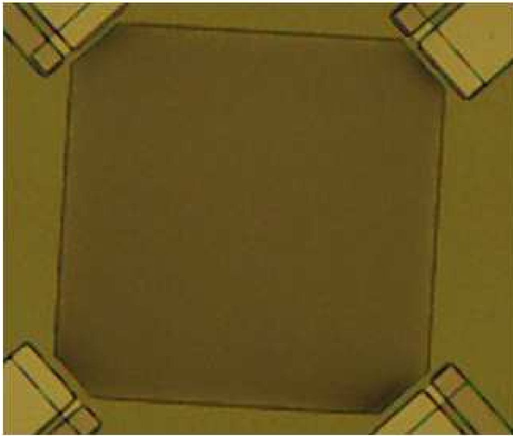

Figure 6.4: Optical microscope image of the optical stack after prolonged exposure to 1165.

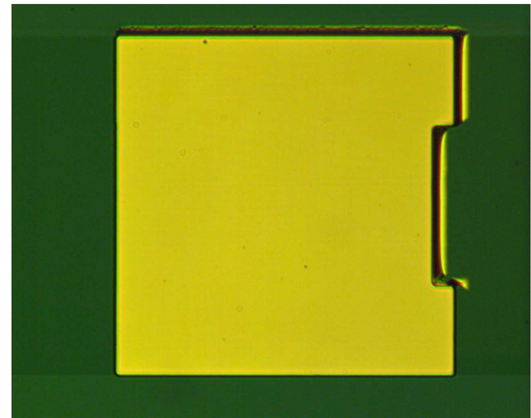

Figure 6.5: Optical microscope image of the Ge/Ni optical stack showing evidence of material overhang most prevalent on the top and right edge of the patterned structure.

6.3.4 Encapsulation

After the optical stack has been deposited and lifted off and any material overhang issues have been addressed the optical stack is encapsulated to prevent the film damage issues discussed in Section 6.3.3.2. This is most easily accomplished using ALD Al_2O_3. Using the standard recipe at a substrate temperature of 250°C, 100 cycles yields a film thickness of approximately 11nm which is sufficient for encapsulation.

6.3.5 Interconnect Layer

A metallic interconnect layer must be deposited to electrically connect the p-type and n-type semiconductors to form thermoelectric junctions as well as connect junctions to each other and the bond pads. Many metals were tested for this purpose, Pt, W, Sn, Ni, Cu, Ti, Cr, and Ag. Pt was found to have the lowest contact resistance. Two different interconnect configurations were tested throughout processing, each with their own distinct advantages and disadvantages. As seen in Figure 6.6 the interconnect metal can either be deposited before the thermoelectric films (parts a and b) or after the thermoelectric films (parts c and d). Two major disadvantages to depositing the interconnect metal first is the potential for film fracture in the thermoelectric films and the potential for surface oxidation or contamination in the processing steps between the deposition of the interconnects and the thermoelectric films. The first concern can be minimized by making the interconnect layer very thin, at least an order of magnitude thinner than the thermoelectric films, so the step height is minimized. The second concern can also be minimized by using interconnects made from noble metals such as Pt. Depositing the interconnect layer after the thermoelectric films has many disadvantages. Since the thermoelectric films are fairly thick, the interconnect films must be made even thicker to prevent film fracture. This leads to increased processing time and expense, especially with high-cost materials like Pt, increased device thermal capacitance and time constant, and a need to develop photolithography recipes for very thick lift-off. There is also the concern that the surface of the thermoelectric films could become oxidized or contaminated between their deposition and the interconnect deposition, which is much more of a concern with unstable semiconductors like Bi_2Te_3 and Sb_2Te_3 than a noble metal like Pt. Because of these disadvantages we have chosen to deposit a thin interconnect before the thermoelectric films.

The Pt interconnect layer is deposited using electron beam evaporation. Since Pt has poor adhesion a 5nm layer of Ti is deposited before the 10nm layer of Pt. Since the films are very thin, a deposition rate of .1nm/s is used to ensure process controllability. The film is patterned using the standard single layer lift-off lithography described in 6.2.4 and due to thinness of the films, lift-off should occur in around 10 minutes. An optical microscope image and a layout model of fabrication progress after interconnect layer deposition and patterning can be seen in Figure 6.7. Note that the interconnect layer consists of four small pads to form the thermoelectric junctions near the optical stack and wires running around the outside of the devices to connect the four junctions in series.

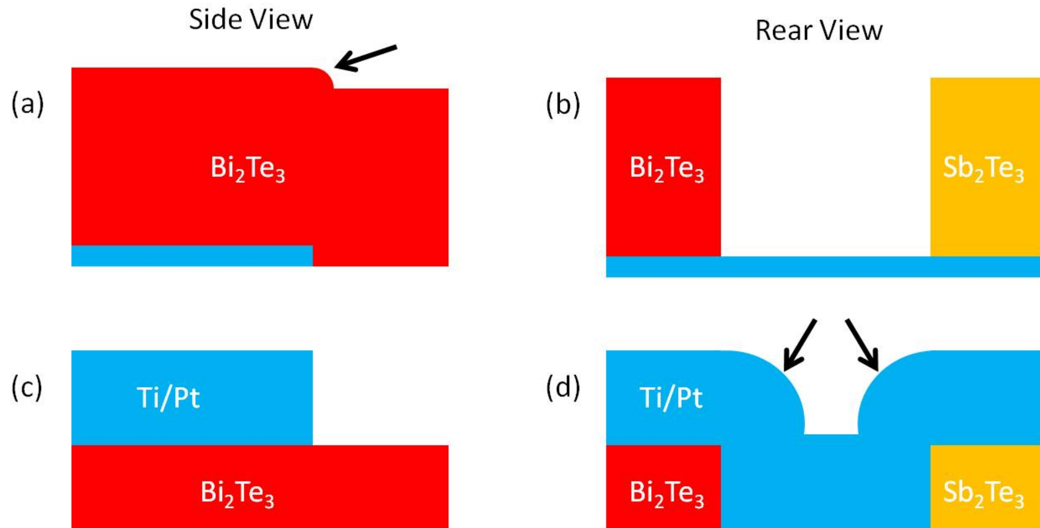

FIGURE 6.6: Diagram of possible interconnect configurations with the interconnect metal running underneath the thermoelectric films from the side view (a) and rear view (b) and the interconnect metal running on top of the thermoelectric films from the side view (c) and rear view(d). The arrows indicate the areas most at risk of film fracture.

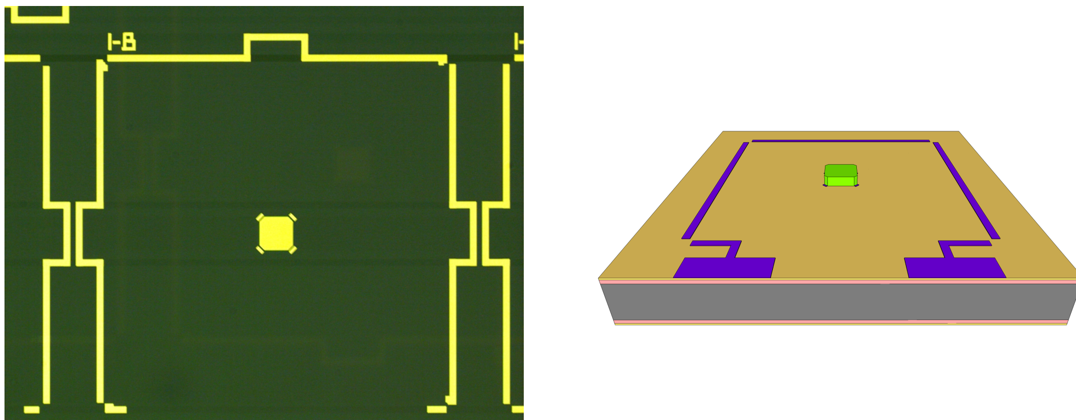

FIGURE 6.7: Optical microscope image and model image of fabrication progress after Ti/Pt interconnect deposition (purple).

6.3.6 Bond Pad and Wire Layer

In order to package devices for vacuum testing they must be wire bonded. A thick metallic layer, preferably gold, must be deposited to form the bond pads. This thick metallic layer can also be used to reduce the resistance of the Ti/Pt wire layers connecting the four thermoelectric junctions. Gold is the preferred metal for bond pads since it is relatively soft and is resistant to oxidation.

The films are deposited using electron beam evaporation. Since Au has poor adhesion the stack consists of a 15nm Cr adhesion layer topped with a 185nm Au bond pad layer.

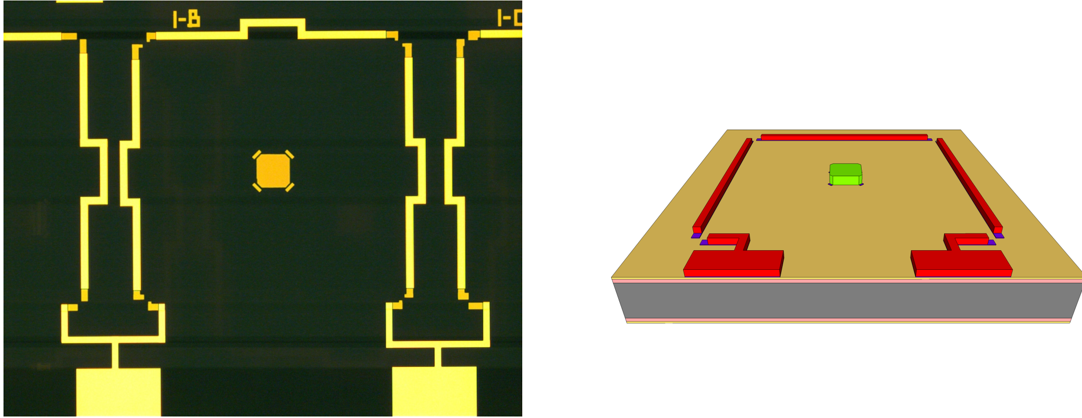

FIGURE 6.8: Optical microscope image and model image of fabrication progress after Cr/Au deposition (red).

These films are deposited with standard recipes with an evaporation rate of .1nm/s for Cr to ensure thickness control while a rate of .3nm/s is used for Au. The thickness of this film is on the same order as the standard LOR 3A recipe so steps must be taken to ensure proper lift-off. This can be done either by slowing the spin speed to 1500rpm or more reliably by using a double layer lift off resist as described in Section 6.2.4. After deposition the lift-off can take hours in hot 1165 but can also be left over night in room temperature 1165 since all volatile films are properly encapsulated at this point in the process. An optical microscope image and a layout model of the wafer after bond pad deposition and patterning can be seen in Figure 6.8. Note that the Cr/Au layer almost entire covers the Ti/Pt layer besides in the area that the Ti/Pt must contact the thermoelectric films.

6.3.7 Thermoelectric Film Deposition

Deposition and patterning of co-sputtered Bi_2Te_3/Sb_2Te_3 thermoelectric thin film junctions presents many difficult engineering challenges which have not been addressed in previous literature. In thermoelectric MEMS device research, co-evaporation [47, 82, 83] is typically the prefered deposition method. MEMS devices have also been fabricated using electrodeposited Bi_2Te_3/Sb_2Te_3 junctions [50]. Neither of these deposition methods are available in the University of Minnesota Nanofabrication Center. Thin film research has also been conducted on co-sputtered Bi_2Te_3 [84] and Sb_2Te_3 [85] but these studies involve unpatterned and uncontacted films on glass. Still, the techniques outlined in these references could prove illuminating for future film improvements.

Sputtering parameters were optimized over many iterations of the process but there is still an element of trial and error. The targets elements, Bi, Sb, and Te, all have low

melting points and low thermal conductance so they must be sputtered at abnormally low powers to prevent damage to the target. At very low powers, any run to run variation in the RF matching circuitry will manifest itself as a significant change in stoichiometry. Small changes in stoichiometry can lead to large changes in the thermoelectric properties of the film [86]. In practice, the resistivity of the Sb_2Te_3 is the most volatile property, varying by a factor of two from run to run using the same recipe. For this reason, the recipe given is meant as a starting point, with some re-optimization required for future work.

Lift-off of thick sputtered films is challenging on its own, but patterning thick co-sputtered Bi_2Te_3 and Sb_2Te_3 adds the additional challenge of very poor film adhesion. Using an adhesion layer such as Ti or Cr is not an option since conduction through these films would significantly degrade the thermoelectric performance of the devices. The films are also susceptible to damage with prolonged exposure to 1165 so the lift-off soak must be quick. In order to meet these challenges, the lift-off resist must be much thicker than the thermoelectric films. Further complicating this issue is the fact that these films are deposited at substrate temperatures up to 260°C. At this temperature the standard thick lift-off resist, Microposit LOR 20B, breaks down and reflows, causing significant film damage during lift-off. To remedy this issue a multilayer film of LOR 3A is used for lift off. The lithography recipe is outlined in 6.2.4 but four layers of LOR 3A are used with a spin speed of 1500rpm. This is sufficient for a target thickness of 500nm, or 90 minutes of deposition at the powers given. The amount of cycles and spin speed can obviously be adjusted for thicker and thinner films.

Bi_2Te_3 is deposited a substrate temperature of 260°C while Sb_2Te_3 is deposited at 230°C as suggested by Zou [82]. Because of this, Bi_2Te_3 should always be deposited first to avoid exposing Sb_2Te_3 to temperatures higher than its deposition temperature. To prevent contamination the chamber should be pumped down to 2x10^{-6} Torr before turning on the heater and once again after the heater is on as the substrate heating will cause much outgassing. For both deposition steps, it is vital to ramp the substrate heater very slowly to prevent temperature overshoot by the proportional-integral-derivative (PID) controller. Fast ramp rates and/or substrate temperatures above 260°C can lead to a permanent bake-on of the lift-off resist. All materials are sputtered using RF magnetron sputtering and as such require a strike layer before deposition to ignite a plasma. The strike layer for each material should be done at a pressure of 35mT in Ar. To protect the targets, a ramp rate of 300s should be used. Once at full power, the chamber pressure should be reduced to the deposition pressure of 5mT of Ar and the targets should be pre-sputtered for 300s in order to remove any contaminants and oxidation. Sputtering powers of 27W (5.92mW/mm^2), 22W(4.82mW/mm^2), and 26W(5.70mW/mm^2) are used for Te, Bi, and Sb respectively. A 90 minute deposition run yields an approximate

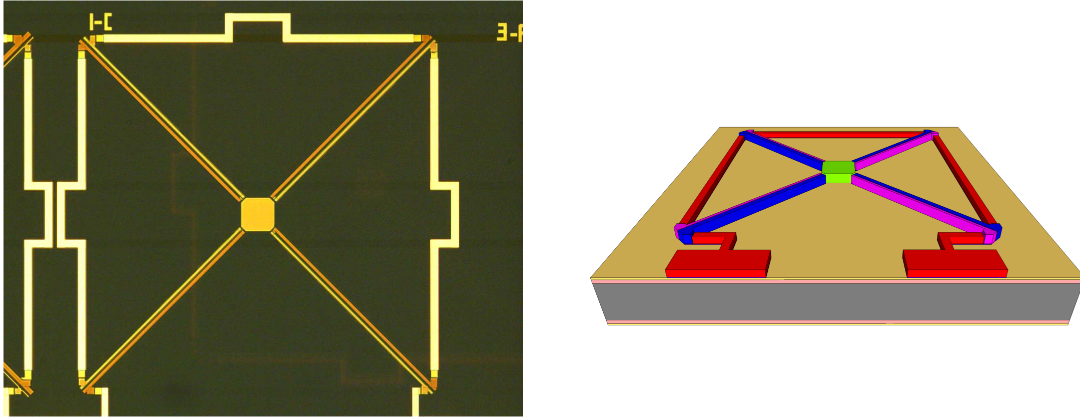

FIGURE 6.9: Optical microscope image and model image of fabrication progress after Bi_2Te_3 and Sb_2Te_3 deposition (blue and purple).

film thickness of 540nm for Bi_2Te_3 and 425nm for Sb_2Te_3. After deposition is complete, the power should be ramped down slowly for 300s and the substrate should be allowed to cool below 100°C before venting to prevent film contamination. The film is very brittle so lift-off occurs in a matter of minutes in heated 1165. Small particles are common after this lift-off step so thorough rinsing is needed. A microscope image and a layout model of the device after thermoelectric film deposition can be seen in Figure 6.9. Note that we now have four thermoelectric junctions in close proximity to the optical stack connected in series by the interconnect layer.

6.3.7.1 Thermoelectric Material Overhang

Much like the optical film stack lift-off process, a common issue with the patterning of the thermoelectric film is material overhang. As seen in Figure 6.10, this problem is widespread with many pieces of thermoelectric materials hanging off the lithographically defined area. While the alignment tolerance of these layers is much greater than that of the optical stack, this issue could present problems if pieces of material fracture and fall off the thermoelectric legs after encapsulation as this would leave the thermoelectric films exposed to the DRIE Bosch etch causing device failure. Attempts were made to remove these structures with SF_6 and O_2 plasma etches but both significantly increased the resistance of the films, disproportionately to the thickness reduction of the film, and left particles throughout the wafer. Ultrasonic agitation is not an option because of the poor adhesion of the films. In the end it was found that there was little that can be done about these structures. So, while this does lead to lower process yield, it is not catastrophic.

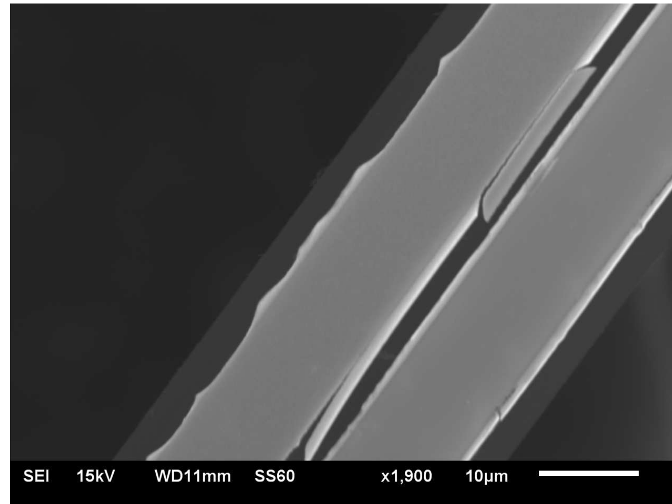

FIGURE 6.10: SEM image of the thermoelectric film showing signs of material overhang fracturing off the lithographically defined area.

6.3.8 Encapsulation

In order to protect the thermoelectric materials from subsequent etch steps the wafer must be encapsulated with a layer of ALD Al_2O_3. Since Sb_2Te_3 is deposited at 230°C we chose to avoid exposing it to a higher temperature in the standard 250°C ALD Al_2O_3. Instead, the final encapsulation layer is deposited at a substrate temperature of 180°C. This recipe produces a slightly lower quality film as evidenced by a higher etch rate in the DRIE Bosch process, but since the top side of the wafer is not directly exposed to this etch, the film is sufficient for encapsulation. Using the standard recipe, 200 cycles yield a film thickness of approximately 22nm.

6.3.9 Backside Hard Mask Deposition

Though the 55nm backside ALD Al_2O_3 should theoretically be sufficient as a hard mask during etch release, the film is weakened by repeated exposure to CD-26 and 351, both of which etch Al_2O_3. Though many processing runs have successfully been completed without reinforcing the backside etch mask, it is best not to skip this step to avoid wafer loss. Mid-release photographs of a wafer without a reinforced hard mask after 100 (left) and 200 (right) cycles of the DRIE Bosch process can be seen in Figure 6.11. Note the arc shape to the damaged area, we believe this occurs due to CD-26 damage to the Al_2O_3 during spin development of LOR 3A. The Al_2O_3 hard mask reinforcement layer is deposited using electron beam evaporation. An evaporation rate of .2nm/s is used to minimize substrate heating and a total film thickness of 100nm is sufficient.

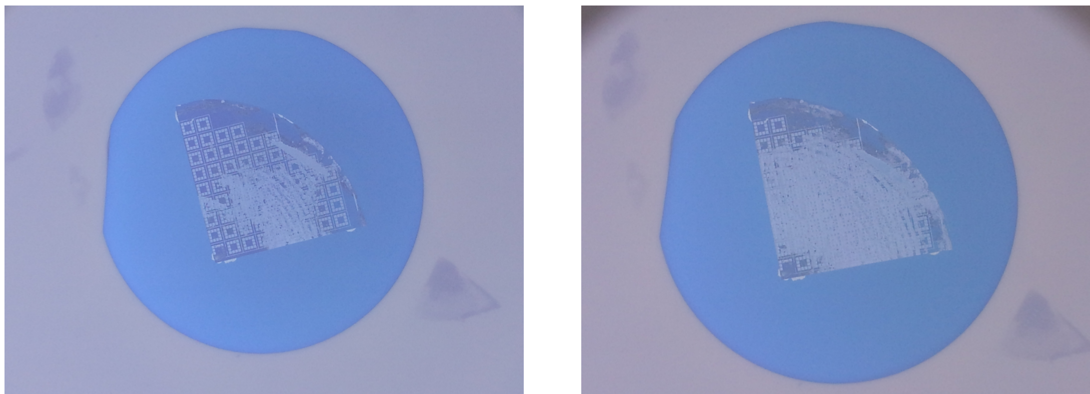

FIGURE 6.11: Image of the wafer during etch release showing significant hard mask breakdown after 100 cycles (left) and 200 cycles (right) of the DRIE Bosch Process.

6.3.10 BCl_3 Plasma Etch

In order to form the thermal isolation structure of the device and to form vias to the bond pads which are covered in insulating ALD Al_2O_3 at this point in the process, the film must be patterned using a BCl_3 plasma etch. Buffered Oxide Etch (BOE) is not an option because of the tight alignment tolerances around the optical stack and thermoelectric films. To protect the films on the back side of the wafer, the back side is first coated with 1813 using the process described in 6.2.3 but skipping from spin-on directly to hard bake. Next, front side 1813 patterning is done using the standard recipe in 6.2.3. The wafer is then bonded to a thick carrier wafer using a bead of 1813 around the edge which is hard baked a second time.

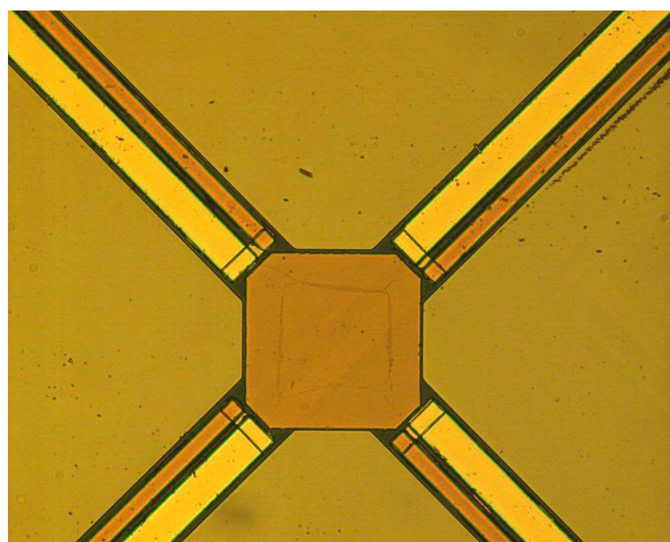

FIGURE 6.12: Microscope image of the device after BCl_3 plasma etching showing evidence of resist burn-on in the optical stack area.

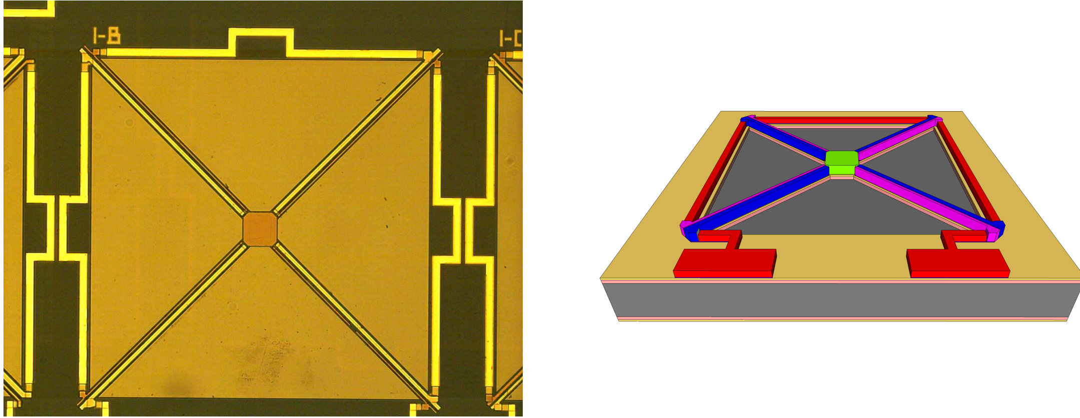

FIGURE 6.13: Optical microscope image and model image of fabrication progress BCl_3 plasma etching.

Resist burn-on can be a significant issue during this plasma etch step. The power coming into the wafer due to incident plasma cannot be dissipated enough by the cooling system of the etcher and the resist becomes thermally damaged. Many steps have been taken to minimize this effect but it is still an issue in most processing runs as can be seen in the optical stack of Figure 6.12. The power of the etcher is reduced to the minimum level that still produces a stable plasma, 625W in the Inductively Coupled Plasma (ICP) generator and 12W in the Reactive Ion Etch (RIE) generator. The plasma is also cycled, 15s on, 60s off to minimize the heating of the wafer. Using this recipe, the etch rate ALD Al_2O_3 is approximately 35nm per minute of plasma on-time. The total thickness of the ALD Al_2O_3 is 55nm, so an etch time of at least two minutes is typically used to ensure that the film is completely etched. This can be verified by etching the wafer in a CF_4/O_2 plasma etch, which attacks the underlying SiN_x. When the etch is complete the resist can be stripped using acetone, but due to resist burn on, typically requires a 10 min O_2 plasma clean to fully remove the resist. An optical microscope image and a layout model of the etched device can be seen in Figure 6.13.

6.3.11 Backside Hard Mask Patterning

Backside hard mask patterning is similar to front side Al_2O_3 patterning as described in Section 6.3.10. However, after coating the front side of the wafer with 1813 to protect it during etch steps, the back side of the wafer is patterned using the 1805 lithography process described in Section 6.2.2. The wafer is patterned using front-to-back alignment. Since the feature size of the backside hard mask is not critical, BOE is used to remove the bulk of the Al_2O_3. The BOE etch should be done in 1 minute increments, rinsing and inspecting for evidence of significant undercut after each minute with a total etch time around 6 mins. If necessary the etch can be finished using the BCl_3 plasma etch

described in Section 6.3.10. The resist strips easily in acetone if the plasma etch is not used.

6.3.12 Etch Release

The DRIE Bosch Process is used to remove the Si below the device to leave a released microstructure. This is a highly anisotropic plasma etch that uses a polymer side-wall coating to prevent undercutting. The devices are released a quarter wafer, or less, at a time to avoid the non-uniformity of the etch outside the center two inches of the chuck. The etch begins on the back side of the wafer, and bores completely through the wafer to release the devices so the quarter being released must be bonded upside-down to a carrier wafer using AI Technology 7016 Cool Grease (cool grease) to thermally contact the quarter wafer being released to a carrier wafer, typically a thick Si wafer coated with a 100nm coating of ALD Al_2O_3. The cool grease is applied by first heating a small amount to 65°C on a glass slide to make it less viscous, then it is applied liberally to the outside edge of the front side of the quarter wafer. The quarter is then mounted to the carrier wafer face down and heated to 65°C to reflow the cool grease. The proper mounting position of a quarter wafer on the carrier wafer can be seen in Figure 6.11 It is important to use enough thermal grease and to ensure that the grease is not expired to prevent thermal damage to the thermoelectric films like that seen in Figure 6.14.

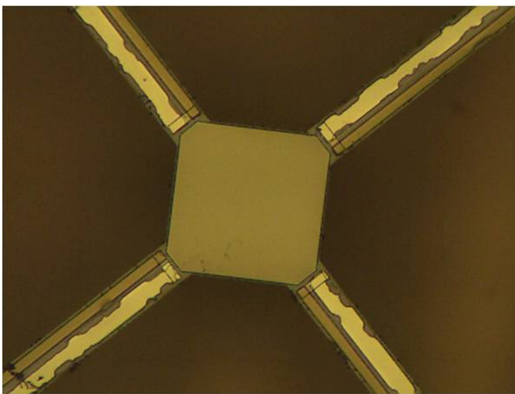

FIGURE 6.14: Microscope image of thermoelectric films showing significant thermal damage due to poor thermal contact during etch release.

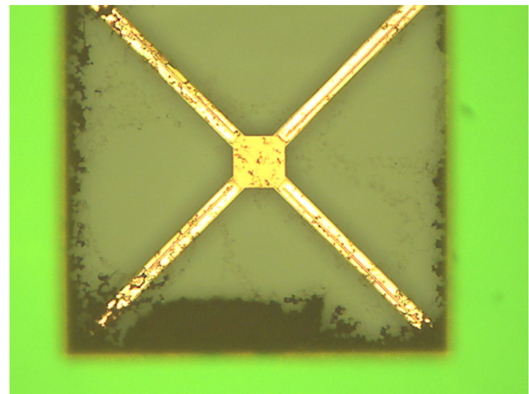

FIGURE 6.15: Microscope image of a device after the final 5-10μ was removed using SF_6 plasma showing unknown particulates.

Using the standard Bosch recipe in the DRIE, the etch rate of Si is approximately 1μm/cycle but depends greatly on the amount of exposed silicon. Etch progress can be monitored by viewing the wafer from the window on the top of the DRIE chamber. When the etch has completed, the larger devices can be viewed in the etch pits. After the majority of the Si below the device is removed, the etch can be finished using a

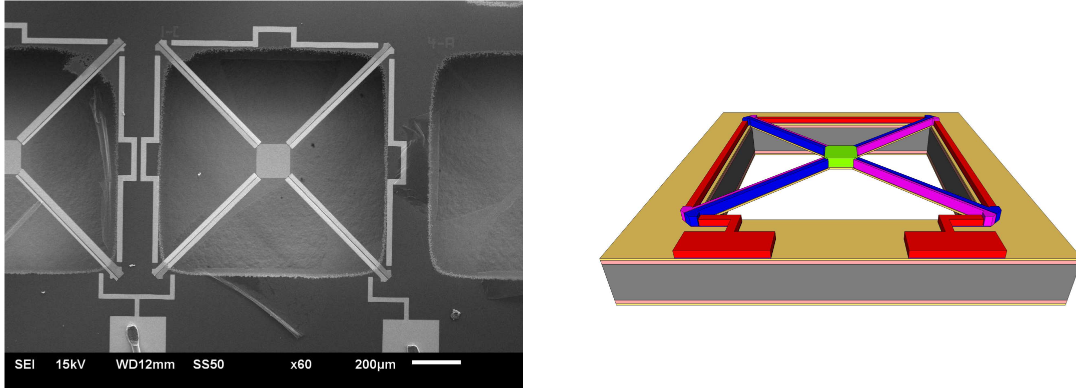

FIGURE 6.16: SEM micrograph and model image etch released detector.

standard SF_6 plasma etch on low power. It is important, however, that a majority of the etch release is done by the DRIE Bosch process, otherwise and unknown substance like that seen in Figure 6.15 tends to develop on the detectors. An optical microscope image and layout model of the released detector can be seen in Figure 6.16.

6.4 Micropillar Fabrication

Fabrication of micropillars for use in micromirrors for cavity coupling involves the in-house fabrication of Silicon on Insulator (SOI) wafers, a single-mask patterning step, and a DRIE Bosch Process etch to form the pillar structure. The micromirror reflective films are then deposited on top of the pillars. The majority of the process development and fabrication work on these structures was performed by Anand Gawarikar, and further details of this process are available in his thesis [87]. Model images of the basic fabrication flow for this process can be seen in Figure 6.17.

6.4.1 SOI Fabrication

In order to reliably control height of the micropillars we fabricate SOI wafers in house from a thick handle wafer and a thin device wafer of the same thickness as that used for the detector dies. This ensures that the micropillar height is approximately equal to device die thickness which is vital for proper cavity spacing. Both wafers are thermally oxidized and then fusion bonded to form an SOI wafer as shown in Figure 6.17 (a). The SOI wafer is then coated with ALD Al_2O_3 which will serve as the hard mask during etch release as seen in Figure 6.17 (b).

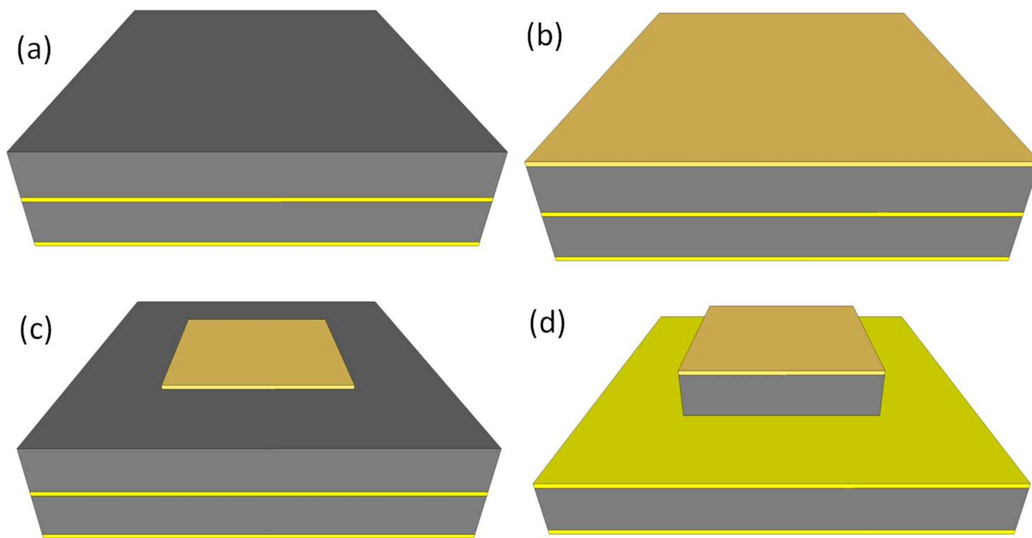

FIGURE 6.17: Model images of micropillar fabrication flow including SOI Fabrication (a), SOI wafer coating (b), hard mask patterning (c), and etch release (d).

6.4.2 Pillar etching

Before the pillar itself can be etched, the Al_2O_3 hard mask must be patterned. It is patterned with 1805 lithography using a transparency mask and BOE wet etch to form square structures in the hard mask as seen in Figure 6.17 (c). The pillars can then be formed by etching away the device wafer stopping on the buried oxide using the DRIE Bosch process as seen in Figure 6.17 (d).

6.4.3 Micromirror Deposition

In order to serve as micromirrors in an optical cavity scheme the micropillars must be coated with infrared reflecting layers. Before micromirror deposition the Al_2O_3 hard mask is stripped using BOE. The micromirror consists of an optically thick Cr base mirror which acts as both an adhesion layer and reflector which is then topped with quarter wave layers of NaF and Ge to form a distributed Bragg reflector. All films are deposited using thermal evaporation at elevated a substrate temperature of 200°C which is set and controlled using a home built heating element and commercial PID controller. An SEM image of the fabricated and coated micropillar can be seen in Figure 6.18 and a model image of this stage can be seen in Figure 6.19.

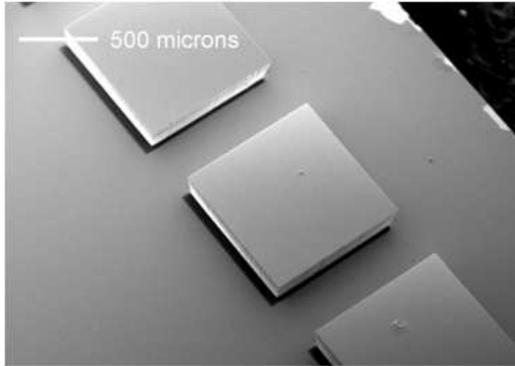

FIGURE 6.18: SEM micrograph of released and coated micropillars.

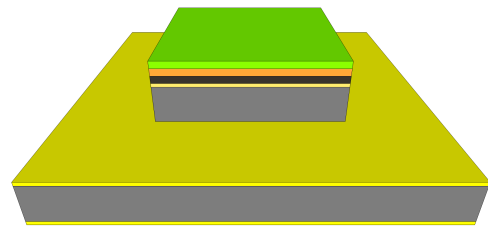

FIGURE 6.19: Image of micropillar model after etch and optical coating with Cr (black), NaF (orange), and Ge (green).

6.5 Microaperature Fabrication

In order to most accurately define the area of the detector, a microaperture must be used. Fabrication consists of a single mask process that follows a similar process flow to the previous steps. The basic process flow can be seen in Figure 6.20. A thin (250μm) Si wafer is coated with a 1000 cycle (110nm) coating of ALD Al_2O_3 which will serve as a hard mask. The back side of the wafer is coated with 1805 to protect it during BOE etching before the front side hard mask is patterned using 1805 lithography and an eight minute BOE etch. After stripping the resist, the wafer is bonded to a carrier wafer using cool grease and DRIE Bosch etched through the wafer to create the aperture. In order to prevent infrared transmission through the wafer, it is the coated with a 250nm thick layer of electron beam evaporated Al. Since the Al_2O_3 hard mask was only patterned on one side of the wafer, this process creates Al_2O_3 membranes instead of apertures, but these membranes can be broken using a probe tip. In future work, it would be simpler either to pattern the hard mask on both sides of the wafer or to strip the Al_2O_3 on the unpatterned side by not coating it with 1805 before BOE etching.

6.6 Device Assembly

With the detector, micromirror, and microaperture dies fabricated, we must still assemble these into a low order optical cavity in order to make a functional device as seen in Figure 6.21. A majority of the process development and fabrication in this step of the process was done by Anand Gawarikar and further details are available in his thesis [87]. The dies are aligned and assembled using a flip-chip bonder. Room temperature epoxy acts as both a bonding and spacing material. SEM images of the micromirror

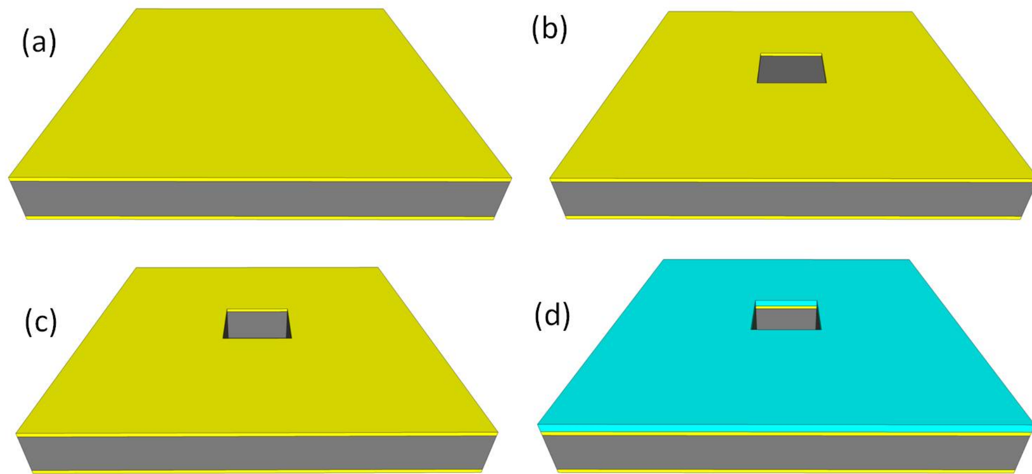

Figure 6.20: Model images of microaperture fabrication flow including ALD Al_2O_3 coating (a), Al_2O_3 hard mask coating (b), DRIE Bosch process etch (c), and Al reflective layer coating (d).

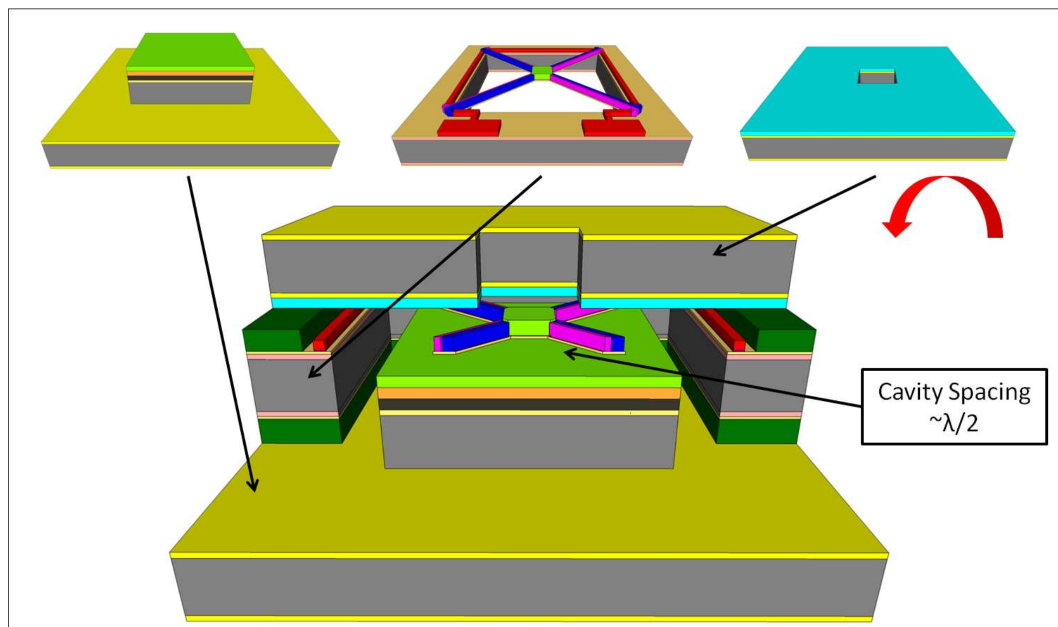

Figure 6.21: Model images of the assembly of the final device with the micropillar and detector dies assembled into a $\lambda/2$ cavity with the microapperature opening over the detector.

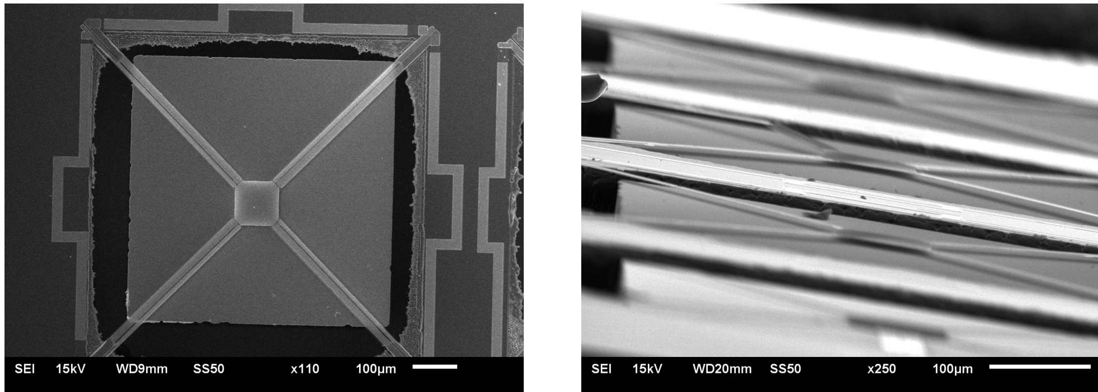

FIGURE 6.22: SEM micrograph of micromirror and detector dies assembled into an optical cavity from normal incidence (left) and high angle incidence (right).

and detector dies assembled into a $\lambda/2$ cavity from normal and high angle incidence can be seen in Figure 6.22.

The microaperture is attached to the top of the device die in the same manner as the mirror is attached to the detector. A confocal microscope image of the detector as seen through the microaperture can be seen in Figure 7.25. After the three dies are assembled, they are placed into a dual inline package and wire bonded for testing. A microscope image of the packaged and wire bonded dies can be seen in Figure 6.24.

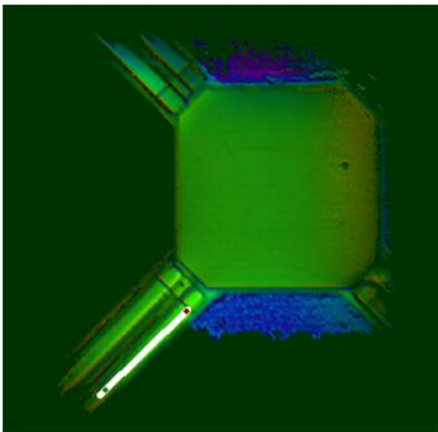

FIGURE 6.23: Confocal microscope image of the detector as seen through the aligned and attached microaperture. Image courtesy of Anand Gawarikar.

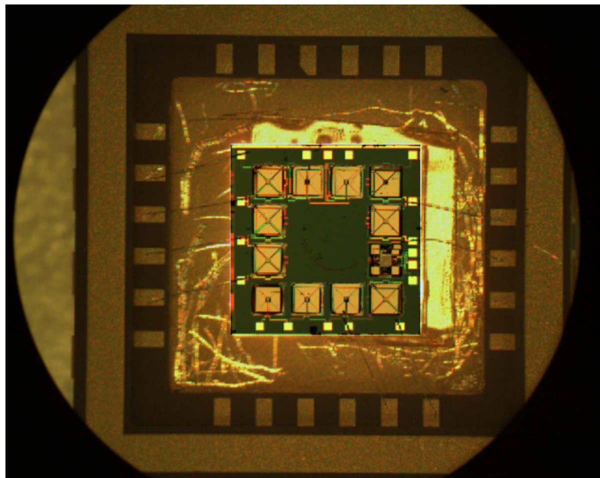

FIGURE 6.24: Optical microscope image of packaged and wire bonded die including micromirror and detector. Image courtesy of Anand Gawarikar.

Chapter 7

Characterization

7.1 Introduction

This section outlines the various characterization techniques and results for both the materials used in detector fabrication and the detectors themselves. These measurements include the characterization of the stoichiometric, structural, electrical, and optical properties of films as well as the nessesary device performance metrics such as responsivity and detectivity. References to the '1B' device geometry refer to the device design presented in Chapter 3.

7.2 Thermoelectric Characterization

Many properties of our thermoelectric and structural films must be investigated in order to estimate device performance and intelligently engineer devices. Properties measured include the temperature coefficient of resistance of the Ti/Pt resistors as well as the film composition, carrier concentration, intrinsic stress, resistivity, Seebeck coefficient, and thermal conductivity of the thermoelectric films. The section concludes with the calculation of the thermoelectric figure of merit of our films.

7.2.1 Temperature Coefficient of Resistance

The temperature coefficient of resistance (TCR) of the Ti/Pt interconnect layer must be known in order to measure the temperature of released microsctructures like those used to characterize the Seebeck coefficient and thermal conductivity. Metals typically have a positive TCR due to increases in phonon scattering at increased temperatures.

An image of the experimental setup used to measure TCR can be seen in Figure 7.1. The setup relies on a thermoelectric element to change the temperature of the device while its resistance is measured. The thermoelectric element is attached on one side to a heat sink and to a copper plate on the other using a thermally conductive tape. The copper plate will serve as the test surface due to its high thermal conductivity. The temperature of the copper plate is monitored using a thermistor which is both clamped in place and immersed in a thermally conductive paste to ensure it is accurately measuring the temperature of the plate. The device is placed on this plate and contacted electrically using probe tips which are aligned with a microscope.

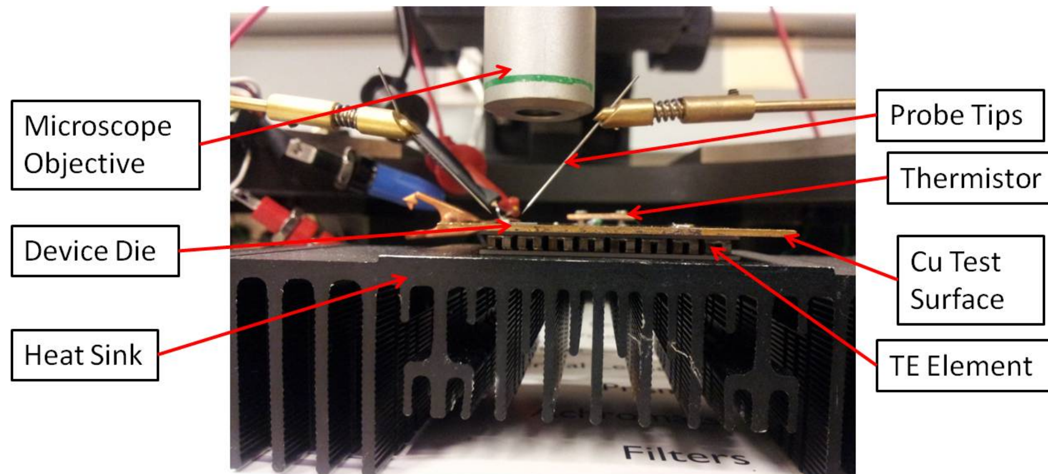

FIGURE 7.1: Image of the TCR measurement setup.

The TCR has been measured in three different ways in order to find the most accurate measurement scheme. Unreleased devices offer the best thermal contact between the Ti/Pt resistors and the copper plate. However, these measurements are suspsect due to changes in resistance during etch release. Typically, released devices will have approximately 25% lower resistance than their unreleased counterparts, possibly due to annealing effects during etch release. It is then reasonable to suspect that the TCR of this material will also change during etch release. Released devices are measured first by simply placing the device on the copper plate and taking the standard measurement. Since these devices are highly thermally isolated, a measurement is also taken after immersing the devices in electrically non-conducting oil in order to increase the thermal contact between the device and the copper plate. Standard vacuum pump oil is used for this purpose and is applied with a syringe. The measured TCR data for all three scenarios can be seen in Figure 7.2. For ease of comparison, data from shorter length resistors is shown for the unreleased devices since unreleased devices have higher resistivity. The average TCR of the unreleased devices was .195%/K, while the released devices had a TCR of .156 %/K in air and .165%/K in oil. We feel that the measurement done in

oil offers the most accurate TCR estimate, so this value is used when calculating the temperature of released structures.

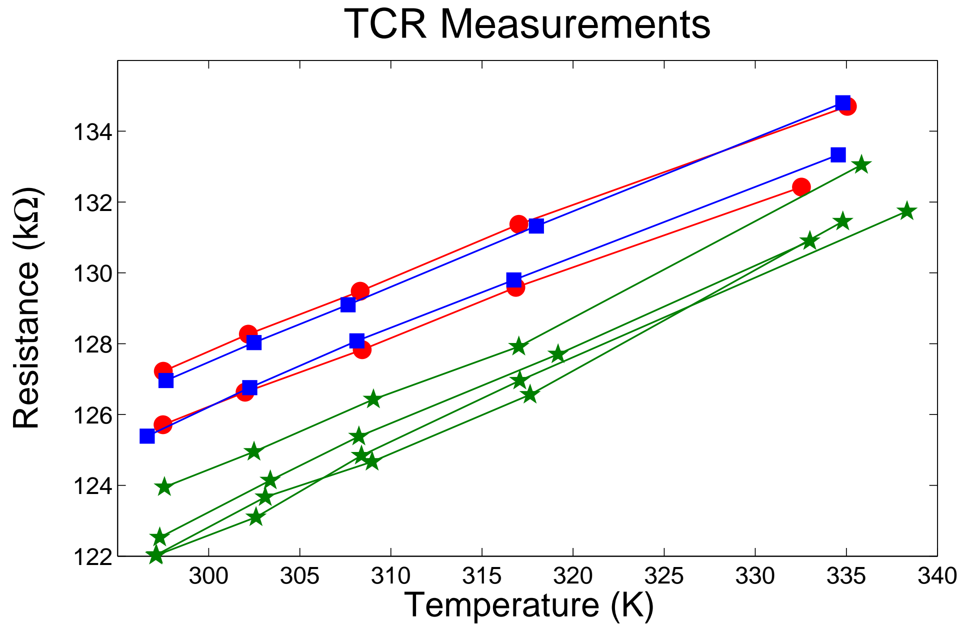

FIGURE 7.2: TCR data for unreleased devices (green), released devices in air (red), and released devices in oil (blue).

7.2.2 Film Composition

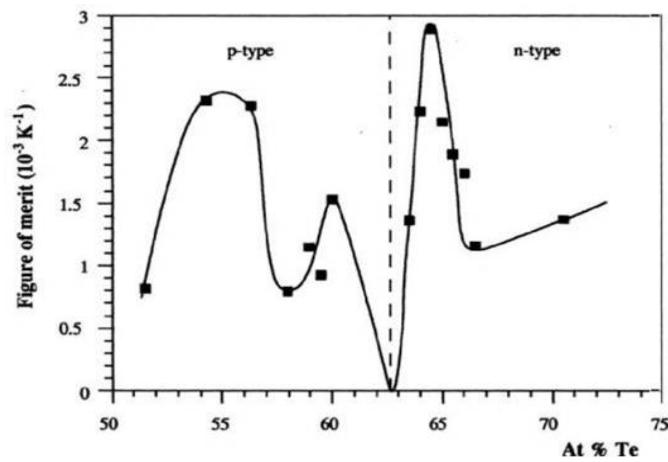

FIGURE 7.3: Thermoelectric figure of merit vs Te composition plot for Bi_2Te_3 from the CRC handbook of thermoelectrics [86].

The thermoelectric figure of merit, Z, of thermoelectric thin films depends strongly on their composition [85, 86]. In the case of V/VI semiconductors such as Bi_2Te_3 and Sb_2Te_3 the doping type and density is determined by the relative concentration of the

two elements as seen in Figure 7.3. The preferred method of measurement for film composition is Energy-dispersive X-ray spectroscopy (EDS). EDS is a tool attached to a scanning electron microscope (SEM) in which the sample is bombarded with an electron beam which knocks lower shell electrons out of the atoms of the sample. As higher shell electrons fill the gaps created in this manner they give off x-rays of a unique energy, which allows for the identification of elements. This measurement technique is often considered semi-quantitative so the measurements for Bi_2Te_3 has previously been verified using Rutherford Backscattering (RBS) which bombards a sample with He ions and monitors the energy of the backscattered ions. However, Sb_2Te_3 cannot be measured in this way since the energy of backscattered ions is dependent on the atomic number of the elements present so Sb and Te cannot be differentiated as they are adjacent on the periodic table. The EDS spectrum for Bi_2Te_3 can be seen in Figure 7.4 and the spectrum for Sb_2Te_3 can be seen in Figure 7.5. The compositions were measured over 4 samples deposited in the method described in Section 6.3.7 and the average composition of Bi_2Te_3 was found to be 45.4% Bi and 54.6% Te while the average composition of Sb_2Te_3 was found to be 38.1% Sb and 61.9% Te.

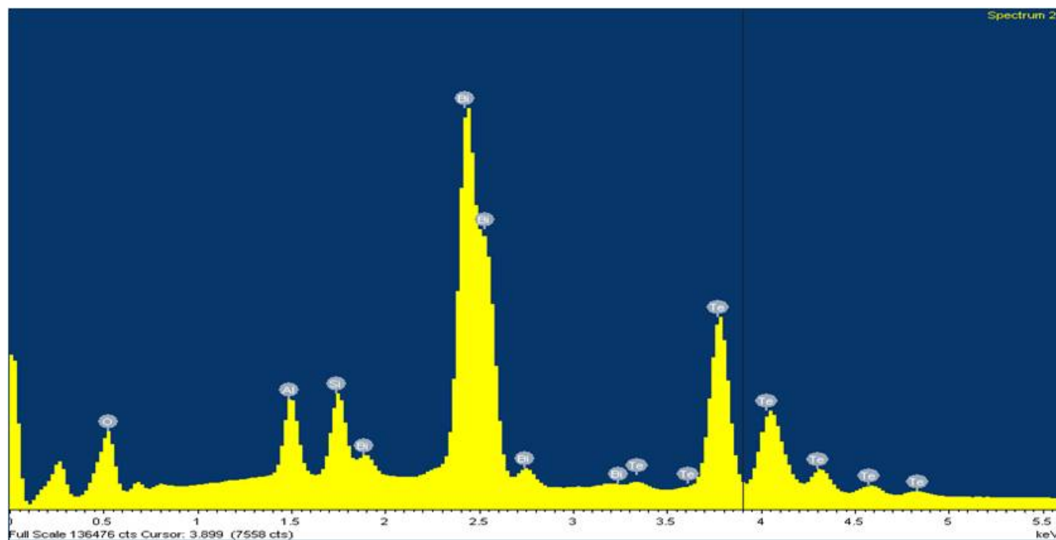

Figure 7.4: EDS spectrum of Bi_2Te_3.

7.2.3 Carrier Concentration

The thermoelectric properties of thin films also depend heavily on carrier concentration as seen in Figure 7.6 from the CRC handbook of thermoelectrics [86]. Carrier concentration is measured using the Hall effect test structure shown in Figure 7.7. The structure is wire bonded and placed in a Quantum Design Physical Property Measurement System (PPMS). A current is sourced in the X direction while the PPMS sweeps

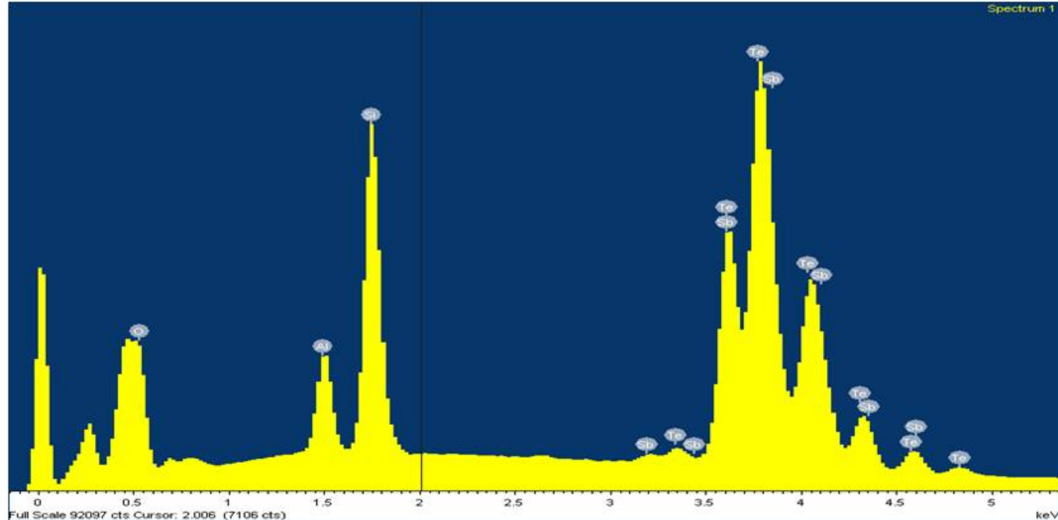

FIGURE 7.5: EDS spectrum of Sb_2Te_3.

a magnetic field in the Z direction, which induces a Hall voltage in the Y direction. The Hall voltage vs magnetic field data for both materials can be seen in Figrure 7.8. We can calculate the carrier concentration of the films using Equation 7.1,

$$N_c = \frac{-B}{V_H} * \frac{I}{et} \tag{7.1}$$

where N_c is the carrier concentration, B is the magnetic field, V_H is the Hall voltage, I is the current, e is the electron charge, and t is the thickness of the film. The slope of Figure 7.8 is used to calculate B/V_H while film thickness is measured with profilometry, I is a controlled source current, and q is a known constant. Opposite signed slopes indicate opposite doping types. From this we can calculate a carrier concentration of $6.96*10^{20}$cm^{-3} electrons in Bi_2Te_3 and $1.35*10^{20}$cm^{-3} holes in Sb_2Te_3. These values are significantly higher than the optimized thermoelectric power factor for degenerately doped semiconductors as shown in Figure 2.7, but we must keep in mind that these are different semiconductors with different deposition conditions so direct comparison is difficult. Also, our preliminary work tested many sputtering recipes that likely investigated many doping concentrations (though carrier concentration was not measured) and these recipes had the best overall thermoelectric properties.

7.2.4 Intrinsic Stress

Intrinsic stress is measured using a Frontier Semiconductor FSM 900TC film stress measurement system. Using this system, the radius of curvature of <100> Si wafers

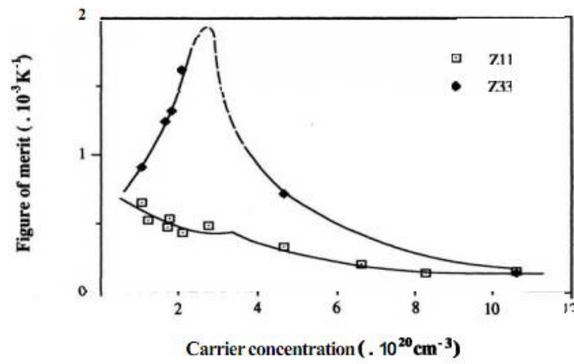

FIGURE 7.6: Thermoelectric figure of merit vs carrier concentration plot for Sb_2Te_3 from CRC handbook of thermoelectrics [86].

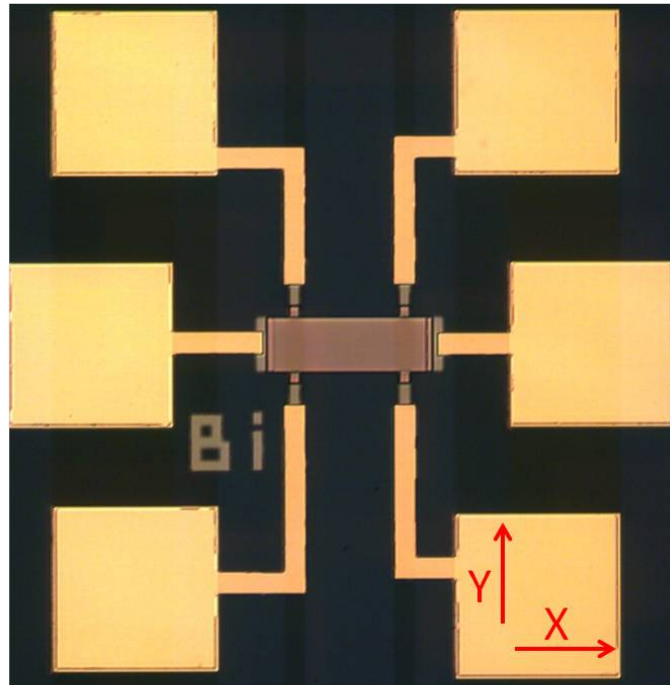

FIGURE 7.7: Hall effect test structure for carrier concentration measurements.

is measured on multiple axes before deposition. The thermoelectric films are then deposited on the wafers using the same deposition parameters described in Section 6.3.7. After deposition the radius of curvature is once again measured. Intrinisic stress can then be calculated using Stoney's equation shown in Equation 7.2,

$$Stress = \frac{Et_w^2(\Gamma_i - \Gamma_f)}{6(1-v)t\Gamma_i\Gamma_f} \tag{7.2}$$

where E is the Young's Modulus of the substrate, assumed to be 130 GPA, t_w is the

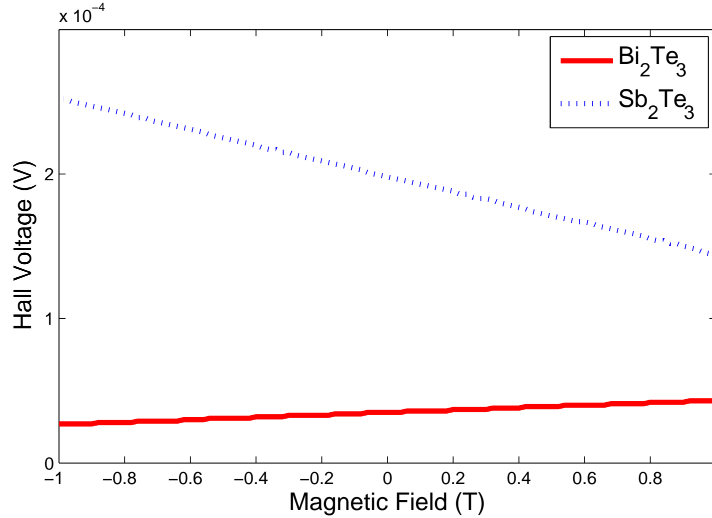

FIGURE 7.8: Hall voltage vs magnetic field data for carrier concentration measurements.

thickness of the substrate, Γ_i and Γ_f are the initial and final radius of curvature of the wafer, v is the Poisson's Ratio of the substrate assumed to be .279, and t is the thickness of the film. The average measured stress over 3 axes was 41 MPa tensile for Bi_2Te_3 and 51 MPa tensile for Sb_2Te_3. All measurements are taken at room temperature.

7.2.5 Resistivity

The resistivity of the thermoelectric films determines the overall device resistance and therefore the Johnson noise of the device. The test structure used to measure the resistivity can be seen in Figure 7.9. This structure essentially gives us a resistor of well defined volume. We can then use Equation 7.3 to calculate the resistivity ρ,

$$\rho = \frac{Rwt}{L} \tag{7.3}$$

where R is the resistance measured with probe station and source meter, t is the film thickness measured with profilometry, and w and L are the width and length of the structure which are defined lithographically. The average resistivity values measured over many structures was 7.6$\mu\Omega$-m for Bi_2Te_3 and 17.4$\mu\Omega$-m for Sb_2Te_3. If we apply these values to the 1B device design we find a device resistance of 14200Ω.

FIGURE 7.9: Test structure for resistivity measurements.

7.2.6 Contact Resistance

Connections between the thermoelectric materials and the interconnect metals are a significant source of contact resistance which directly degrades device performance by adding to the device's Johnson noise. Eight different metals, Pt, W, Sn, Ni, Cu, Ti, Cr, and Ag, were tested and Pt was found to have the lowest contact resistance to Bi_2Te_3 and Sb_2Te_3. Contact resistance was measured using the test structure shown in Figure 7.10. This structure consists of a resistor of varying length with well defined contact area. We measure the resistance of the device at each length interval over several devices to create the plot seen in Figure 7.11. The y-intercept of this plot then represents a resistor of zero length, so this value can be attributed solely to contact resistance. We then normalize this value to the contact area to find a contract resistance of 60.5 $\mu\Omega$-cm^2 for Bi_2Te_3 and 81.5$\mu\Omega$-cm^2 for Sb_2Te_3. If we apply these values to the 1B device design, we calculate a contact resistance of 808Ω or 5.4% of the total device resistance.

7.2.7 Seebeck Coefficient

The Seebeck coefficient of the thermoelectric films contributes directly to the responsivity and therefore detectivity of the detector. The Seebeck coefficient was measured using the test structure shown in Figure 7.12. This structure is essentially a micro-heater sharing a thermal isolation structure with the hot side of a thermoelectric junction. The cold side of the thermoelectric junction rests on the substrate which serves as a heat sink and is assumed to be at room temperature. This allows us to source a current through the micro-heater while measuring the resistance in order to calculate the temperature using Equation 7.4.

FIGURE 7.10: Test structure for contact resistance measurements.

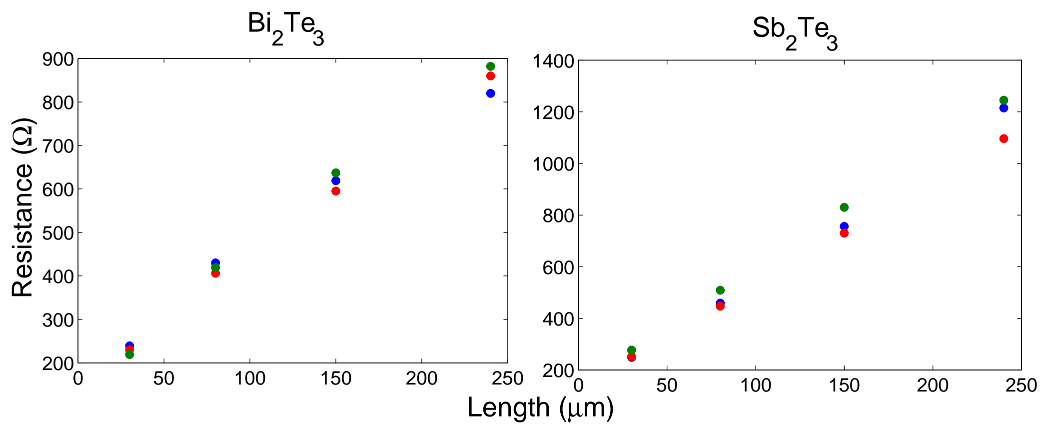

FIGURE 7.11: Contact resistance data for both materials.

$$\Delta T(R) = \frac{\frac{R}{R_0} - 1}{\alpha} \tag{7.4}$$

Equation 7.4 is derived from the definition of the TCR where $\Delta T(R)$ is the change in absolute temperature at a measured resistance R, R_0 is the initial resistance, and α is the TCR of the resistor. By sweeping the current and measuring the voltage generated in the thermoelectric junction we are able to measure the slope of the Seebeck voltage vs ΔT plot seen in Figure 7.13 to calculate the Seebeck coefficient of each material. The measurements shown in Figure 7.13 are taken using junctions formed between a single thermoelectric material and a Pt reference. The results are also verified using test structures with thermoelectric junctions formed between the two materials. Using these

test structures we measure a Seebeck coefficient of -45μV/K for Bi_2Te_3 and 105μV/K for Sb_2Te_3 with a combined system value of 150μV/K.

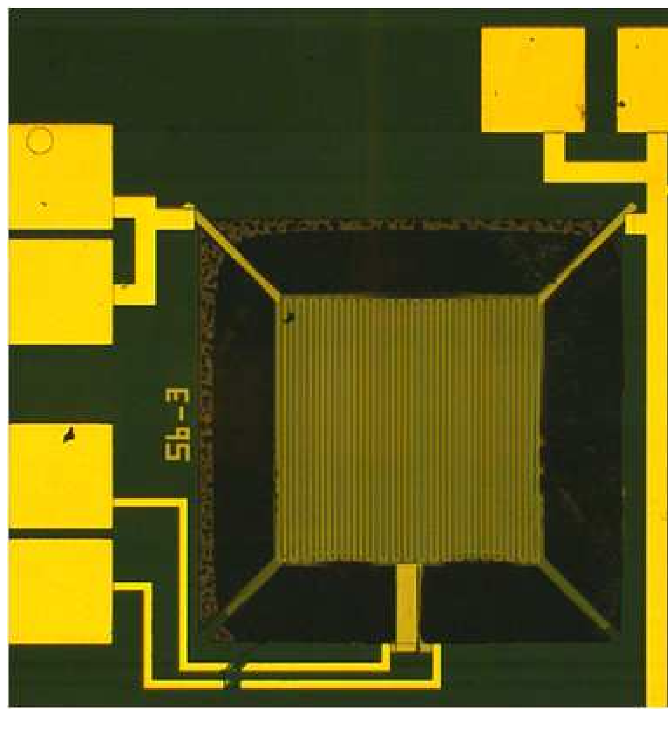

FIGURE 7.12: Microscope image of Seebeck coefficient test structure

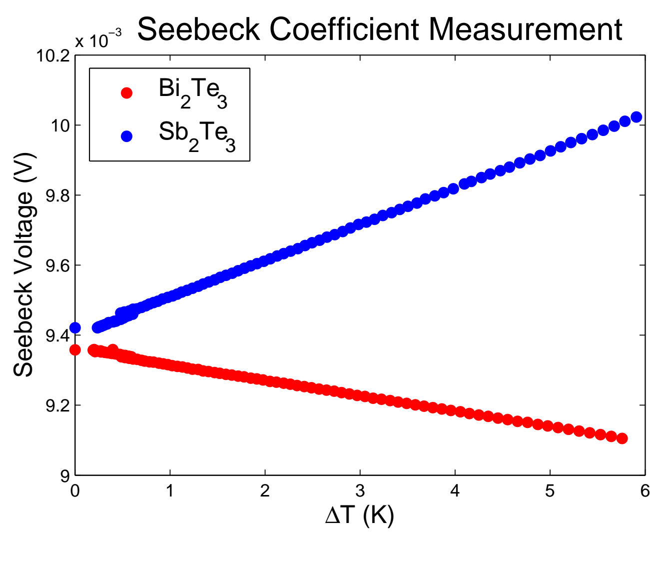

FIGURE 7.13: Seebeck voltage vs temperature change data from test structures like those seen in Figure 7.12

7.3 Thermal Conductivity

The thermal conductivity of the thermoelectric films and the supporting Al_2O_3 contributes directly to the thermal conductance of the device. The thermal conductivity of these films was measured using test structures like those seen in Figure 7.14. These test structures are simply micro-heaters with broad and short supports of the material being studied. The purpose of this structure is to ensure that the thermal conductance of the device is dominated by the film under test. The drawback of this approach is that with large enough legs the device could act more like a membrane than a thermally isolated plate, which can cause temperature non-uniformity in the center plate. To calculate the respective contributions of radiation and film thermal conduction, we employ the method described in Chapter 5. In this method a current can be sourced through the micro-heater while the resistance is measured to calculate the temperature of the device using Equation 7.4 and measure the temperature response to input power of the structure. The degree of non-linearity of this response is measured using fitting coefficients for the linear and fourth order temperature dependent components as descibed in Chapter 5. These fitting coefficients can then be applied to the derivative of the power balance equation to calculate the thermal conductance through the supports and through radiation at room temperature. As can be seen in Figure 7.14, there is significant misalignment in the structure, which complicates modeling. In order to account for this, the film thermal conduction of the device is modeled as 100 parallel heat pipes. Microscope images were taken of the back side of the wafer in order to measure the length of each heat pipe.

We use devices containing no thermoelectric materials like those seen in Figure 7.14 (a) to calculate the thermal conductivity of the ALD Al_2O_3 films to be 1.75W/mK which is lower than the value reported by Gabriel [56]. This is not unexpected since this method measures thermal conductance in the plane parallel to the wafer surface while the 3ω method measures thermal conductance perpendicular to the wafer surface. Our films are also thinner and deposited in three different deposition steps, which could increase interfacial scattering. Using this value we can then measure the thermal conductivity of the thermoelectric films. After accounting for radiation thermal conductance effects and thermal conductance through the Al_2O_3 we calculate thermal conductivity values of .34W/m-K for Bi_2Te_3 and .30W/m-K for Sb_2Te_3.

7.3.1 Figure of Merit

The thermoelectric figure of merit of the junctions can be calculated using Equation 7.5,

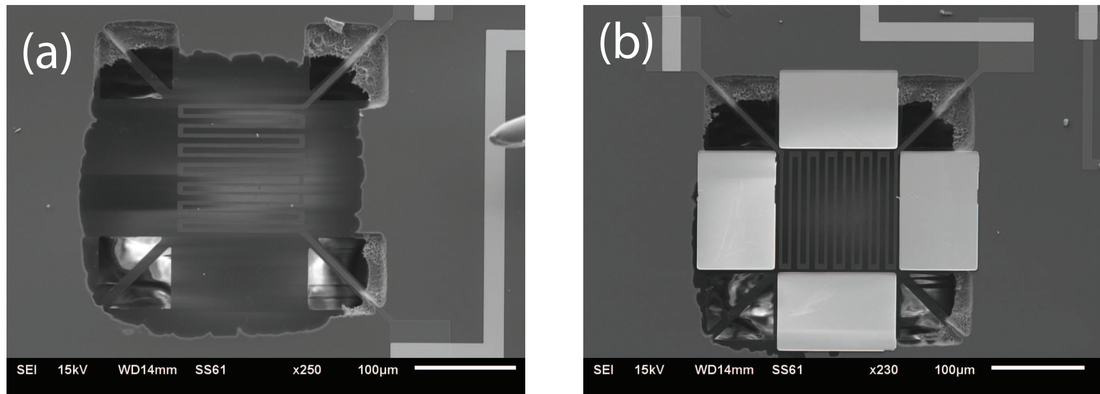

FIGURE 7.14: SEM images of the thermal conductivity test structures for (a) Al_2O_3 and (b) thermoelectric film measurements.

$$Z = \frac{(S_1 - S_2)^2}{(\sqrt{\rho_1 * \kappa_1} + \sqrt{\rho_2 * \kappa_2})^2} \tag{7.5}$$

where S_1 and S_2 are the Seebeck coefficients, ρ_1 and ρ_2 are the resistivities, and κ_1 and κ_2 are the thermal conductivities of Sb_2Te_3 and Bi_2Te_3 respectively. We calculate a value of Z=.00145 K^{-1} or at room temperature we calculate the unitless ZT=.43. For single materials Equation 7.5 simplifies to Z=$S/(\rho\kappa)$ and we can calculate a unitless room temperature figure of merit ZT of .266 for Bi_2Te_3 and .552 for Sb_2Te_3.

7.4 Device Characterization

While characterization of material parameters gives us a starting point for estimating device performance, the properties of the devices themselves must also be measured to fully characterize the device. Measurements presented include micromirror reflectance, cavity spacing, thermal conductance, responsivity, thermal time constant, detector noise, and specific detectivity. The majority of the work presented in this section was performed by Anand Gawarikar and more details can be found in his thesis [87].

7.4.1 Micropillar Reflectance

To form a Fabry Perot cavity with our detector, we must ensure that the backing mirror has high reflectance in the wavelength region being studied. The reflectance of the micromirrors deposited on the micropillars is measured using a Fourier transform infrared (FTIR) microscope. The reflectance is measured relative to a gold mirror and normalized so the maximum reflectance is unity as these mirrors typically have a higher

reflectance than gold. The reflectance as a function of wavelength can be seen in Figure 7.15. In this spectrum we see reflectance greater than 90% from 6 to 12μm.

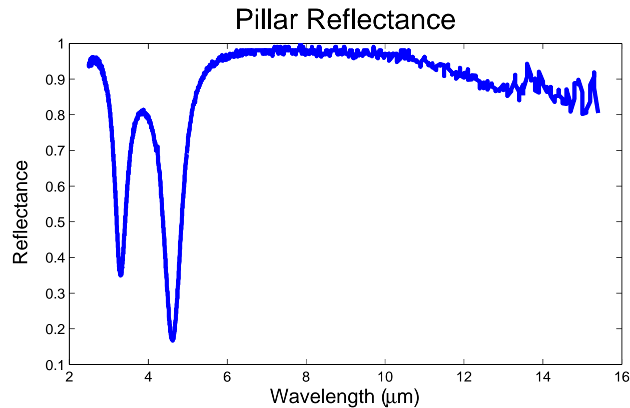

FIGURE 7.15: Micromirror reflectance spectrum measured with FTIR microscope.

7.4.2 Cavity Spacing

The gap spacing of assembled cavities determines the resonant absorption wavelength of the device. A typical Fabry-Perot configuration calls for a $\lambda/2$ air gap, but our devices will have a slight offset due to transmission through optically thick Ge and phase shifts from metallic reflectors and absorbers. The FTIR microscope can be used to measure the reflectance spectrum of assembled cavities as well as estimate the absorption spectrum. Since the backing mirror is highly reflecting from 6μm on, as seen in Figure 7.15, it can be assumed that transmission in this region is minimal and therefore absorption is simply 1-R. The measured reflectance spectrum of a low order assembled cavity can be seen in the red curve of Figure 7.16. A optical transfer matrix simulation as described by Yeh [57] of this device using the parameters given in Table 7.17 reveals a cavity spacing of 5.1μm.

7.4.3 Thermal Conductance

The thermal conductance of a thermal detector impacts its thermal time constant as well as its thermal conductance noise, responsivity, and detectivity. We estimate the thermal conductance of our devices using a method similar to that described by Foote [15]. This method operates in two distinct time steps. First, a current flows through the thermoelectric films to induce both Joule and Peltier heating in the center plate. Next, the current is removed and the voltage generated across the thermoelectric legs by the temperature difference between the center plate and the substrate which serves

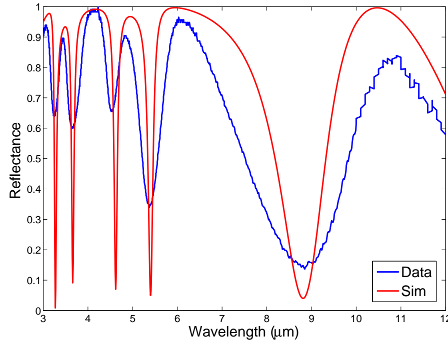

FIGURE 7.16: Measured (blue) and simulated (red) reflectance spectrum of a low order optical cavity.

Material	Thickness (nm)	Index
Al_2O_3	20	1.3
Ni	2	6.2+29.5i
Ge	280	4
Al_2O_3	20	1.3
Air	5100	1
Ge	500	4
NaF	1538	1.3
Cr	60	5.6+26.3i

FIGURE 7.17: Layer thickness and refractive index for cavity spacing simulation.

as a heat sink is measured. In this setup, the power into the thermally isolated center plate is given by equation 7.6,

$$P_{in} = \frac{I^2R}{2} + INST \tag{7.6}$$

where P_{in} is the total power, I is the current, R is the device resistance, N is the number of thermoelectric junctions, S is the Seebeck coefficient difference between the two materials of the junction, and T is the substrate temperature (assumed to be at room temperature). Note that the Joule heating term is halved. This is due to the assumption that half of the Joule heating power reaches the center plate while half goes to the substrate, a common assumption in microcooler and thermopile detector calculations [15, 24]. With the sourced power in and the measured voltage out, we can calculate the electrical responsivity R_E=V_{out}/P_{in}. The responsivity of a thermopile detector is given by Equation 7.7,

$$R_e = \frac{NS}{G} \tag{7.7}$$

where R_e is the electrical responsivity, G is the thermal conductance, and the other terms are defined following 7.6. We can now solve Equations 7.7 and 7.6 for G to calculate the thermal conductance at a given input power. The electrical responsivity and thermal conductance of a 1B device at each input power can be seen in Figures 7.18 and 7.19 respectively. It is difficult to say precisely what the true thermal conductance is using this technique but we select a power at which Joule heating dominates the Peltier heating around 40μW with a thermal conductance of 2.53 x 10^{-7}W/K. This is

likely an overestimate due to radiation thermal conductance effects at the elevated plate temperatures caused by the sourced current.

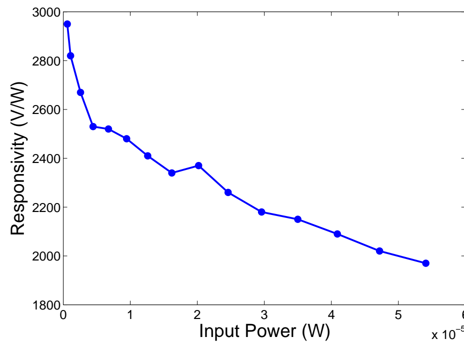

FIGURE 7.18: Electrical responsivity vs input power for a thermopile detector of 1B geometry.

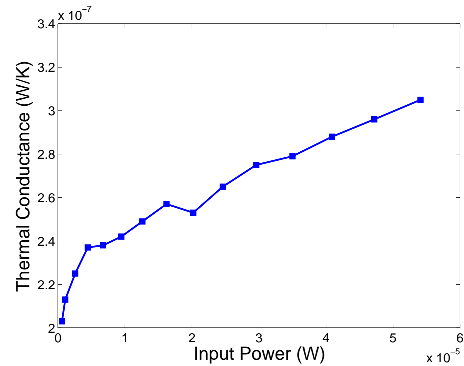

FIGURE 7.19: Thermal conductance vs input power for a thermopile detector of 1B geometry.

Another way to estimate the thermal condutance of the device is to look at the optical responsivity, which in DC exposure is defined as $\Re = \epsilon NS/G$, where ϵ is the emissivity, N is the number of thermoelectric juntions, S is the Seebeck coefficient difference, and G is the thermal conductance. If we assume our peak emissivity is unity, and apply the Seebeck coefficient difference measured in Section 7.2.7, we can apply the measured peak responsivity value from Section 7.4.4 to calculate a thermal conductance of 1.28x10^{-7} W/K, which is close to the low current values measured using the electrical responsivity measurement.

7.4.4 Responsivity

Responsivity is perhaps the most vital and most challenging measurement for thermopile detector performance estimates. We must illuminate the device with an infrared signal of known wavelength and power density and measure quite small voltage signals coming from the detector. A schematic of the Responsivity measurement can be seen in Figure 7.20. Infrared illumination is generated by an Oriel Apex IR element 6575 ceramic blackbody light source. This light is then passed through a 7.5μm long-pass order sorting filter and to a Oriel Cornerstone 260, model 74100 monochromater with a 100 line/mm 9μm blazed grating which reflects light through a slit allowing for the selection of a specific packet of wavelenths. This light is then passed through a shutter and reflected off a gold off-axis parabolic mirror which collimates the light. After reflecting off a gold mirror the light is passed through a ZnSe focusing lens and a anti-reflectance coated ZnSe window onto the device under test, which rests in a vacuum chamber. The voltage generated by the detector fed through a 1000x low noise amplifier

and to a Fluke 45 voltmeter. The amplifier was custom built in-house, more details can be found in [87]. To measure the incident power density, a calibrated Electro-optical Systems MCT10-0100 HgCdTe photoconductive detector is placed in the position of the detector and incident power can be measured in W/mm^2.

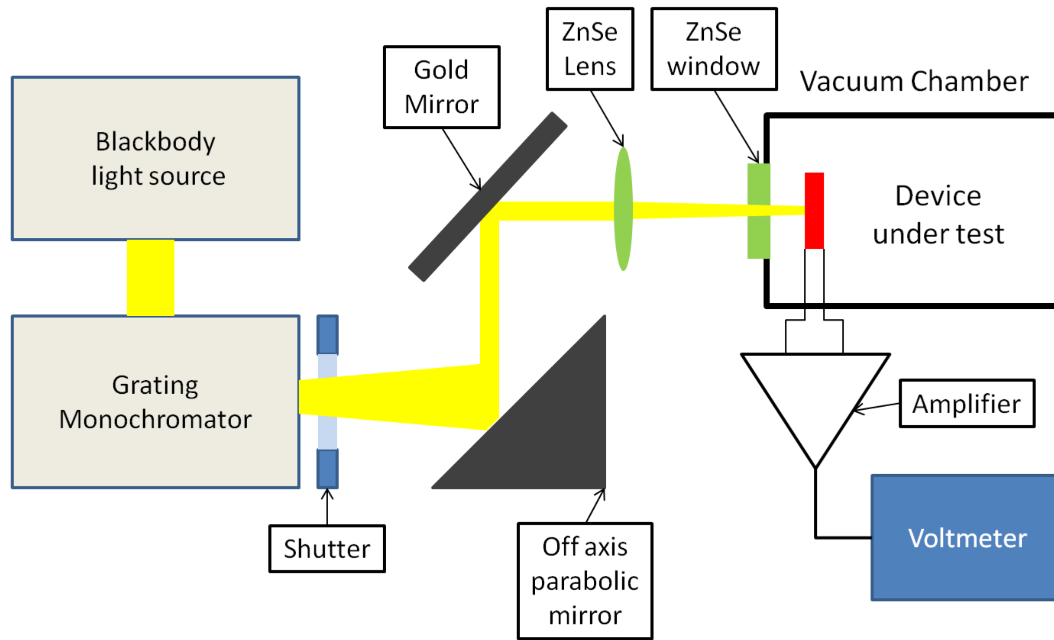

FIGURE 7.20: Schematic of the measurement setup for responsivity measurements.

To measure the responsivity, the device is illuminated for five seconds while 25 signal data points are collected. The shutter is then closed and 25 background data points are collected over five seconds. The background is then subtracted from the signal to determine the actual voltage response of the detector. This is repeated every 50nm while the illumination wavelength is swept from 7.5 to 11 μm. The incident power density is also measured at each wavelength, so given the measured power in and voltage out, we can calculate the responsivity at each measured wavelength as $R = V_{out}/P_{in}$.

Three responsivity measurements are presented for two different devices each giving unique insight into detector performance. The first is the device shown in Figure 7.21 which is a 150μm x 150μm device over a micropillar of similar size to the entire device. As can be seen in Figure 7.22, this yields a peak responsivity of 3630 V/W at 9.6μm with a peak full width half maximum (FWHM) of approximately 1.6μm. We also see a 4.4x enhancement of responsivity on resonance vs off resonance.

The next device presented is a 1B geometry device, a 100μm x 100μm detector over a 200μm x 200μm mirror as seen in Figure 7.23. This geometry causes some interesting optical effects as shown in Figure 7.24. The primary resonance, between the detector and the micromirror causes the broad resonance peak seen in Figure 7.24. However, there

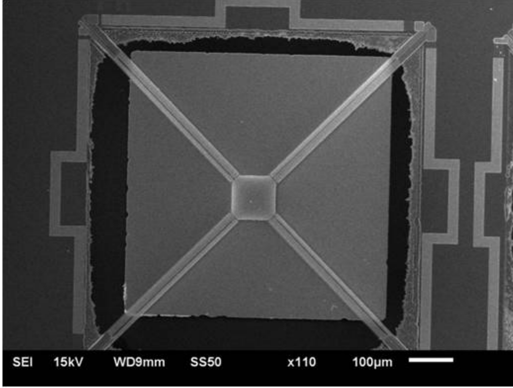

FIGURE 7.21: SEM micrograph of 150μm device over large pillar.

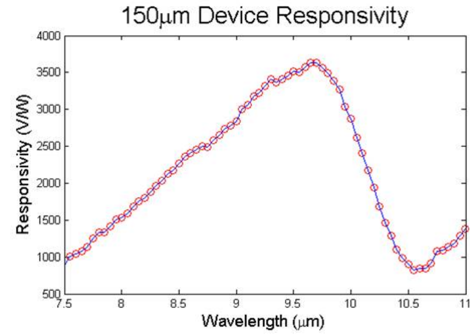

FIGURE 7.22: Responsivity spectrum of 150μm device over large pillar.

is also a series of secondary resonances between the thermoelectric legs and the mirror surface below, which causes the superimposed small magnitude peaks. To validate this theory we look at the free spectral range (FSR) of these superimposed peaks. The FSR of a Fabry Perot interferometer is given by Equation 7.8,

$$\Delta f = \frac{c}{2nlcos\theta} \tag{7.8}$$

where Δf is the FSR, c is the speed of light, n is the refractive index of the material in the cavity, and θ is the angle of incidence of incident radiation. Our measured FSR of 5.47 x 10^{11} Hz corresponds to an air gap of 274μm which is approximately the thickness of the device wafer and validates our theory. The device has a peak responsivity of 6960 V/W at 9.75μm with a FWHM of around 2μm. The important thing to take away from this measurement is that this device has significant absorption in the thermoelectric legs. This is an undesired effect since this added absorption calls into question the emissive area of the device, which will complicate detectivity calculations.

Because of the absorption in the thermoelectric legs, we add a 200μm x 200μm microaperature to block their illumination. A confocal microscope image of the device through the aperture showing the illuminated area can be seen in Figure 7.25. The responsivity spectrum of the 1B device shown in Figure 7.23 with attached aperture can be seen in Figure 7.26. Here we see that the secondary resonance has been greatly suppressed and the device has a peak responsivity of 4700 V/W at 9.35 μm with a peak FWHM of approximately 2 μm. We feel this is our most accurate performance estimate due to a more rigidly defined absorbing area, though possibly an underestimate due to shadowing effects.

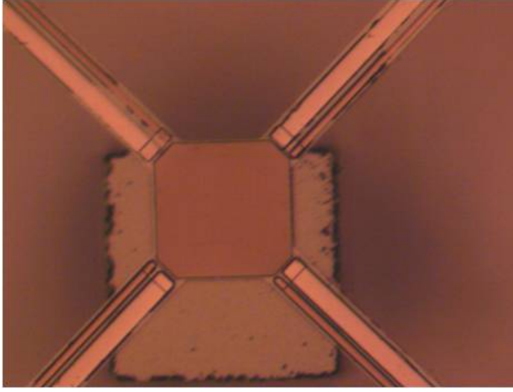

FIGURE 7.23: Optical microscope image of 100μm '1B' device over 200μm pillar.

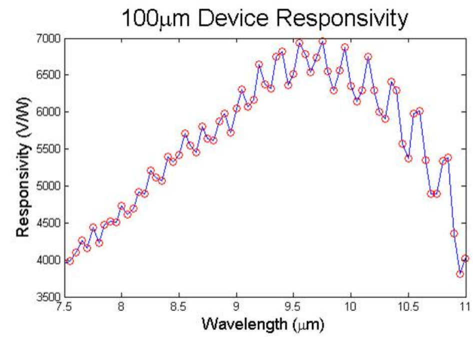

FIGURE 7.24: Responsivity spectrum of 100μm '1B' device over 200μm pillar.

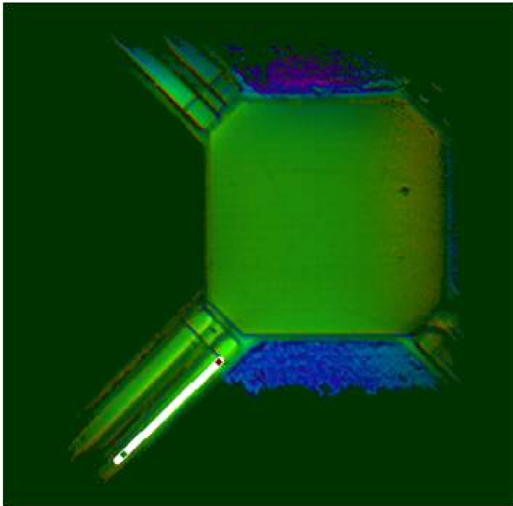

FIGURE 7.25: Confocal microscope image of the 1B device through a 200μm microaperture.

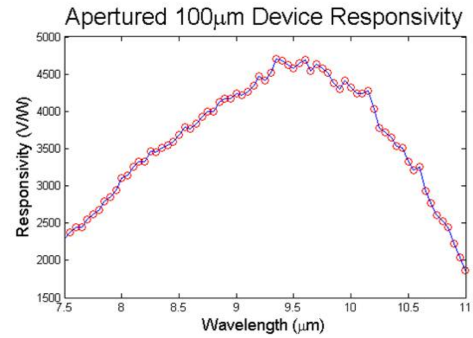

FIGURE 7.26: Responsivity spectrum of the 1B device through a 200μm microaperture.

7.4.5 Thermal Time Constant

The thermal time constant of a thermal detector is defined as $\tau = \mathrm{C/G}$, where τ is the thermal time constant, C is the thermal capacitance, and G is the thermal conductance. This value determines the sensitivity of the device when exposed to frequency modulated input signals as is common in thermal detector operation. Measurement of the thermal time constant exploits the dependence of responsivity on thermal time constant with a frequency modulated input signal as seen in Equation 7.9,

$$\Re = \frac{\nu NS}{G(1+\omega^2\tau^2)^{1/2}} \tag{7.9}$$

where R is the responsivity, ν is the fraction of incident radiation absorbed, N is the number of thermoelectric elements, S is the Seebeck coefficient, G is the thermal conductance, ω is the angular frequency of the input signal, and τ is the thermal time constant. The measurement setup is identical to the that described in Section 7.4.4 but with a chopper installed in the optical path and an EG&G 7260 lock-in amplifier used to measure the output signal of the detector. It can be seen in Equation 7.9 that by measuring the responsivity at various frequencies, we can fit a Lorentzian to the data and extract the thermal time constant as seen in Figure 7.27. For the 1B device geometry we measure a thermal time constant of 58ms.

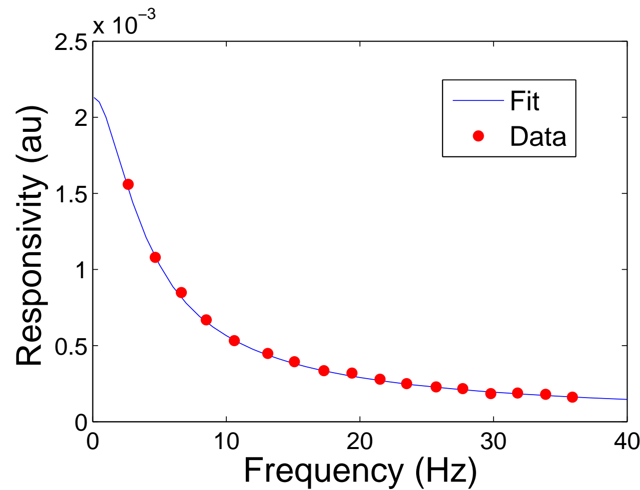

FIGURE 7.27: Thermal time constant measurement and fit.

7.4.6 Noise Measurement

The final measurement that must be made in order to calculate the detectivity of the device is the detector noise. In this measurement, the device under test is placed in a vacuum chamber while the voltage out of the device is passed through a Analog Devices AD4528-1 low noise op-amp and into an HP Model 35660 digital signal analyzer. This allows us to measure the power spectral density of the noise coming from the device. The total noise is measured before subtracting the current and voltage noise of the op-amp to measure the spectrum seen in Figure 7.28. The red line in this plot represents the Johnson noise at the device resistance of 15.1kΩ, which is 16nV/Hz$^{1/2}$. We can see in this plot that the devices are Johnson noise limited with no 1/f noise present down to 100mHz.

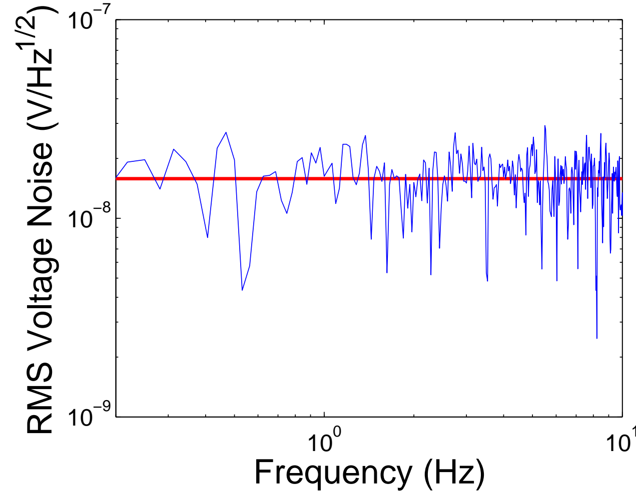

FIGURE 7.28: Noise power spectral density (blue) and fit (red) of 1B device geometry.

7.4.7 Detectivity

The specific detectivity of a thermal detector is the figure of merit for device performance. It is defined in Equation 7.10,

$$D^* = \frac{R\sqrt{A}}{V_{RMS}} \tag{7.10}$$

where D^* is the specific detectivity, R is the responsivity, A is the detector area, and V_{RMS} is the root mean squared noise voltage of the detector, in our case the Johnson noise of the detector. The detectivity spectra of the three devices presented in Section 7.4.4 can be seen in Figures 7.29, 7.30, and 7.31. As previously mentioned, we feel that the apertured 1B device is our most accurate performance estimate due to a more rigidly defined absrobing area, though possibly an underestimate due to shadowing effects.

7.5 Conclusion

In conclusion we will compare our results to the design parameters described in Chapter 3 in Table 7.1. First we see that significant improvements have been made in resistivity, ρ, especially in the resistivity of Sb_2Te_3. This value is a 42% improvement over the design value and a 33.6% improvement over the values published in [55]. It is difficult to hypothesize the reason for this improvement since the sputtering recipe has not changed and the carrier concentration was not measured on previous samples. The improvement in resistivity has lowered the overall device resistance by over 25% which

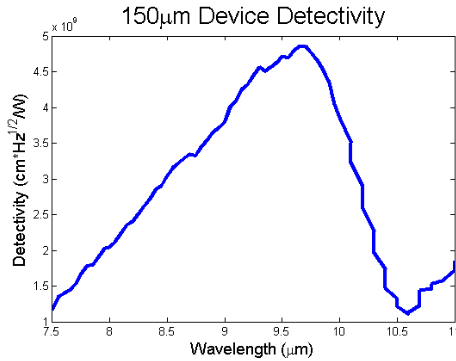

FIGURE 7.29: Detectivity spectrum of 150μm device over large pillar.

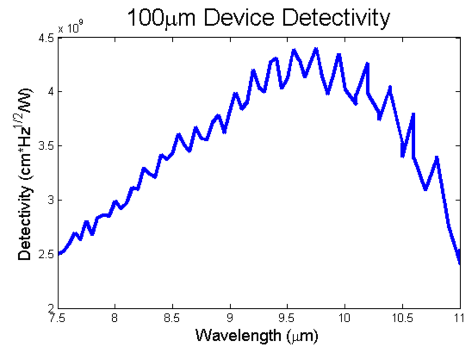

FIGURE 7.30: Detectivity spectrum of 100μm device over 200μm pillar.

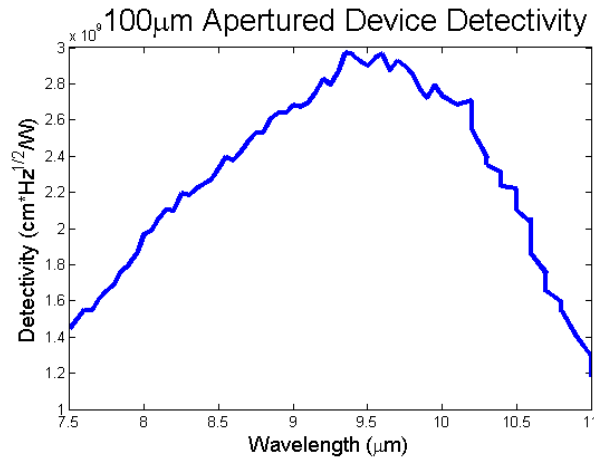

FIGURE 7.31: Detectivity spectrum of the 1B device through a 200μm microaperture.

reduces the Johnson noise accordingly. The Seebeck coefficient values measured were lower than expected and lower than the values published in [55]. We suspect that the values were not actually lower but instead measured more accurately. The previously published values were calculated with a TCR value measured on unreleased devices. If we apply the TCR value of unreleased devices for this processing run, the Seebeck coefficient values are in line with expectations. The reduction in Seebeck coefficient difference causes a reduction to responsivity. The thermal conductivity values measured were significantly lower than the design estimates and previously published values. We believe this could be due to a combination of factors. It is likely that the values published in [55] were overestimates as they did not account for radiation thermal conductance and used a test structure with thermal conductance much less dominated by the films being studied than the latest design. There could also be some measurement error due to membrane-like thermal conduction as discussed in Section 7.3. The thermal conductance of the device is significantly higher than the device design. Poorer than

Table 7.1: Comparison of design parameters and actual results.

Parameter	Unit	Design	Measured
ρ_{Bi2Te3}	$\mu\Omega$-m	10	7.6
ρ_{Sb2Te3}	$\mu\Omega$-m	30	17.4
R	kΩ	20.2	15.1
κ_{Bi2Te3}	W/m-K	1	.34
κ_{Sb2Te3}	W/m-K	1	.30
κ_{Al2O3}	W/m-K	2.6	1.75
Seebeck Difference	μV/K	170	150
Thermal Conductance	W/K	1.2x10^{-7}	2.4x10^{-7}
Responsivity	V/W	5620	4700
Noise	nV/$\sqrt{Hz}$	20	16
Detectivity	cm$\sqrt{Hz}$/W	2.74x10^{9}	3.0x10^{9}
Time Constant	ms	57	58

expected cavity coupling is likely to blame as seen in Figure 7.16. This leads to increased thermal conductance due to radiation. However, if we look at the thermal conductance value calculated using the optical responsivity instead of the electrical responsivity, we see it is in line with expectation, but still higher than expected given the low thermal conductivity values measured. With slightly higher responsivity than expected, but significantly lower Johnson noise, we see that the detectivity exceeds expectations by about 10%. The calculated detectivity exceeds all other published works [16, 19, 20, 22].

Chapter 8

Conclusion and Future Work

8.1 Summary of Results

Long range infrared atmospheric spectroscopy will require uncooled thermal infrared detectors with sensitivity previously unseen in the field. To this end, we have presented multiple approaches to reduce the noise floor of such devices using various optical schemes to minimize unwanted radiation thermal conductance noise without sacrificing signal absorption in the desired sensing range. We have also shown how 1/f noise can be negated using a thermoelectric readout scheme and how state-of-the-art detectors can be made from non-state-of-the-art thermoelectric materials. We have also presented a new method for the analysis of radiation thermal conductance in ultrasmall microcoolers which is applicable to any thermally isolated structure.

Chapter 2 discused the basics of thermoelectric behavior and materials. An analysis of the performance of a thermoelectric device led to the derivation of the thermoelectric figure of merit and a discussion of its application to thermoelectric coolers. A discussion was provided of the optimization of the thermoelectric power factor in semiconductors. The decoupling of the electrical and thermal conductivity was discussed with an emphasis on the selection and engineering of materials. Finally, the state of the art for thermoelectric thin films with an emphasis on films integrated into MEMS devices was covered.

Chapter 3 outlined a basic understanding of thermal infrared detector operation which was vital for the understanding of ensuing chapters. This analysis began with the power balance of thermally isolated structures and progressed through the analysis to detector figures of merit such as responsivity and detectivity. The significant noise sources present in thermal infrared detectors were discussed with particular attention

paid to radiation noise. Chapter 3 then progressed to the design of thermopile infrared detectors with detectivity exceeding all other published works and applied the analysis and modeling presented earlier in the chapter to a practical design.

Theoretical analysis of mid wave infrared (MWIR) detectors with spectrally selective absorption was presented in Chapter 4. These devices employ the natural spectral selectivity of a narrow bandgap semiconductor, PbSe in our case, to absorb MWIR signal while transmitting radiation in the peak room temperature thermal emission band, thus greatly reducing the radiation thermal conductance of the device. The simulated devices use a 1/8th wave optical cavity to further improve broadband coupling in the MWIR. A theoretical analysis of the incorporation of this design into resistive microbolometer produced a theoretical peak detectivity of 4.37x10^{10}cm$\sqrt{Hz}$/W.

In Chapter 5 we presented a new method for the analysis of radiation thermal conductance in extremely isolated microstructures. This method investigated the non-linearity of the temperature response to input power of thermally isolated devices including microheaters. In this case, the film contribution to thermal conductance will have a linear dependence with temperature while the radiation contribution will have a fourth order dependence. We have used the temperature response to match fitting coefficients and applied them to the derivative of the power balance equation to estimate the relative radiation and film thermal conductance at a given temperature. To demonstrate this theory we fabricated thermoelectric microcoolers with integrated microheaters and test their performance relative to radiation thermal conductance limitations.

Chapter 6 outlined the fabrication process used to produce state of the art uncooled thermopile infrared detectors. It addressed many of the unique engineering challenges faced in the process development for such devices. Of particular focus was the deposition, patterning, and electrical contact of the co-sputtered Bi_2Te_3 and Sb_2Te_3 thin films, which have not been previously integrated into MEMS devices using this deposition technique. Fabrication steps have been provided for the detectors themselves, as well as the micropillar with micromirror and microaperture dies concluding with the assembly of these three pieces into a finished detector.

The characterization of the detectors fabricated using the method described in Chapter 6 was presented in Chapter 7. The chapter began with the characterization of material properties such as film composition, carrier concentration, and intrinsic stress as well as thermoelectric properties such as Seebeck coefficient, resistivity, and thermal conductivity of the Bi_2Te_3 and Sb_2Te_3 thin films. Next, the finished devices were characterized to measure cavity spacing, thermal conductivity, thermal time constant, responsivity, and detectivity. The presented devices exhibited peak specific detectivity of at least 3x10^9cm$\sqrt{Hz}$/W which exceeds all other published works.

8.2 Future Work

The ultimate goal of this project is to create uncooled infrared detectors with detectivity exceeding the blackbody radiation limit of 1.81x10^{10}cm$\sqrt{Hz}$/W at 300K. This value was once considered the fundamental limit for thermal detector performance, but this limitation applies only to blackbody absorbing devices. It has been shown in [61] and in Chapter 4 that with proper optical engineering this value can be exceeded. Many possible methods for improving device performance will be discussed in this section, some requiring minor changes to layer dimensions while others may require total design overhaul.

8.2.1 Al_2O_3 Thickness

The Al_2O_3 film in our final devices was perhaps unnecessarily thick. This film was thickened over time due to the degradation of film quality in our ALD system. In the past, resistive microbolometers have been released with Al_2O_3 thickness as low as 8.8nm. If we use the '1B' device design from Chapter 3 and use the thermoelectric parameters measured in Chapter 7 but reduce the total Al_2O_3 thickness from 55nm to 20nm, we can simulate a responsivity of 10200 V/W and a peak detectivity of 5.8x10^{9}cm$\sqrt{Hz}$/W.

8.2.2 Thermoelectric Film Thickness

The thickness of the thermoelectric films was limited to about 500nm due to processing issues such as difficulty lifting off thicker films and low deposition rates. If thicker films are able to be deposited and patterned we can reduce the resistance of the device with a small increase in thermal conductance. More importantly, however, we could use thicker films to reduce the width of the thermoelectric films and therefore reduce their emissive area which could minimize the secondary resonance issue described in Chapter 7. If we increase the thermoelectric film thickness to 1.5μm, we can reduce the width of the Bi_2Te_3 and Sb_2Te_3 films from 5μm and 15μm to 2μm and 6μm respectively while maintaining a similar resistance. Keeping all other design parameters the same as the the '1B' device design from Chapter 3 and using the thermoelectric parameters measured in Chapter 7 we simulate a responsivity of 9470 V/W and a peak detectivity of 5.95x10^{9}cm$\sqrt{Hz}$/W.

8.2.3 Thermoelectric Film Performance

Our thermoelectric thin films, while sufficient to achieve our goals, will need to be improved in order to exceed the blackbody radiation limit. Our films have a unitless thermoelectric figure of merit, ZT, of .43, while state of the art room temperature thermoelectric thin films have ZT values of up to 1. An example of high performance thermoelectric thin films integrated into MEMS devices is presented by Goncalves [83]. In this work Bi_2Te_3 and Sb_2Te_3 films are presented with Seebeck coefficients of -248μV/K and 188μV/K respectively. Both materials had a resistivity of 12.6$\mu\Omega$-m and an assumed thermal conductivity of 1.7 W/m-K. From these values we can calculate a unitless figure of merit of ZT=.67. Since the resistivity of the films is equal, the width of the two films is made equal in the design. The size of the absorbing plate is increased to 200μm x 200μm and all other parameters are kept the same. In this case we simulate responsivity of 6800 V/W with a detectivity 7.26x10^9cm$\sqrt{Hz}$/W.

8.2.4 Three Die Cavity Coupling

Detection beyond the blackbody radiation limit will require a redesign of the optical cavity. The cavity full width half maximum (FWHM) of our devices which exceeds 2μm is not sufficient for ultra high performance devices. Our original optical device design presented in Chapter 3 reduces radiation thermal conductance by 75% compared to a blackbody detector. Ideally we desire a device design for which radiation thermal conductance is essentially negligible with emissivity equal to zero at all wavelengths besides a narrow band at the target wavelength. In order to fabricate a narrowband cavity we must go from a two die optical cavity to a three die optical cavity like that seen in Figure 8.1. This setup will create a Fabry-Perot cavity using two distributed Bragg reflector (DBR) mirrors. Between the two mirrors is a Al_2O_3 absorbing layer. This absorbing layer has a low index and extinction coefficient near 10μm which will ensure the absorber is exposed to many photon round trips. If we simulate the layer structure from Table 8.1 we arrive at the absorption vs wavelength plot seen in Figure 8.2.

In Figure 8.2 we can see that the simulated device has a narrow resonance peak with FWHM of 60nm centered at 10μm. This reduces the radiation thermal conductance of a 100μm x 100μm detector at room temperature from 3.27x10^{-8} W/K to 8.79x10^{-10} W/K which reduces the overall thermal conductance and increases the responsivity accordingly. If we use the '1B' device design from Chapter 3 and use the thermoelectric parameters measured in Chapter 7 we simulate a responsivity of 15300 V/W and a peak detectivity of 9.0x10^9cm$\sqrt{Hz}$/W. If we combine this design change with the thickness

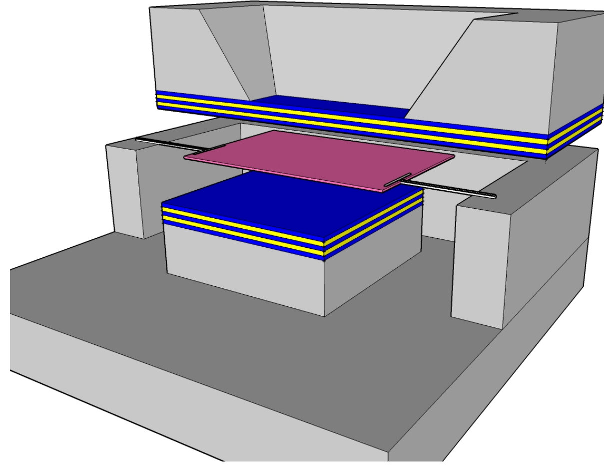

FIGURE 8.1: Model of the three die configuration of the narrowband device.

TABLE 8.1: Layer structure for simulated narrowband device design.

Material	Thickness (nm)	Index (10μm)
Vacuum		1
Ge	625	4
NaF	2016	1.24
Ge	625	4
NaF	2016	1.24
Vacuum	1400	1
Al_2O_3	200	.88+.053i
Vacuum	1400	1
Ge	625	4
NaF	2016	1.24
4 more alternating Ge/NaF pairs		

reduction of the Al_2O_3 from Section 8.2.1 we simulate a responsivity 22100 V/W and a detectivity of 1.29x10^{10}cm$\sqrt{Hz}$/W.

8.2.5 MWIR Spectrally Selective Absorption

The Midwave Infrared (MWIR) spectrally selective device model presented in Chapter 4 can also be used to improve the thermopile detectors. This device uses a PbSe absorber, which is a narrow bandgap semiconductor that absorbs well below 5μm. The absorber is separated from a Ge/NaF DBR by a 500nm air gap. If we simulate the layer structure shown in Table 8.2, we see the absorption spectrum seen in Figure 8.3. In Figure 8.3 we

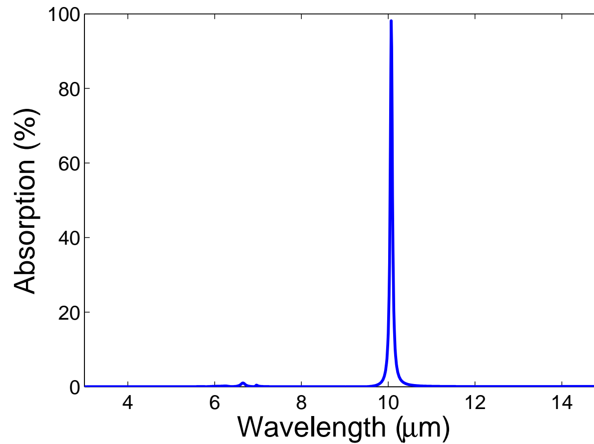

FIGURE 8.2: Simulated absorption spectrum of the narrowband device with layer structure seen in Table 8.1.

TABLE 8.2: Layer structure for simulated MWIR spectrally selective device design.

Material	Thickness (nm)	Index (4μm)
Al_2O_3	20	1.68
PbSe	45	4.52+.80i
Al_2O_3	20	1.68
Vacuum	500	1
Ge	250	4.0
NaF	714	1.30
2 more alternating Ge/NaF pairs		

see a broadband resonance from 3-5μm with very low absorption in the primary thermal emission band. This leads to a radiation thermal conductance of 2.95x10^{-9} W/K for a 100μm x 100μm detector at room temperature. If we use the '1B' device design from Chapter 3 and use the thermoelectric parameters measured in Chapter 7 we calculate a responsivity of 12500V/W and a peak detectivity of 6.24x10^9cm$\sqrt{Hz}$/W. This performance is significantly hindered by the absorption of the device being limited to 86%. If we reduce the Al_2O_3 thickness to 20nm and increase the size of the detector to 300μm x 300μm the peak detectivity increases to 1.8x10^{10}cm$\sqrt{Hz}$/W, which is equivalent to the blackbody radiation limit of a room temperature hemispherical detector. Thermal capacitance of the PbSe film was taken from [60].

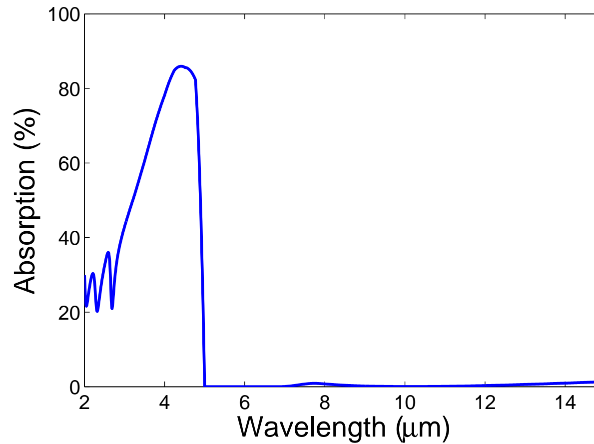

FIGURE 8.3: Simulated absorption spectrum of the MWIR spectrally selective device with layer structure seen in Table 8.2.

8.2.6 Optimized Design

This section has outlined some of the paths available to improve the performance of our devices. For LWIR devices, the best option is the three die cavity coupling scheme outlined in Section 8.2.4. This design can be coupled with thinner Al_2O_3 supports and a redesign of the geometric layout of the device to simulate a device with peak specific detectivity of $3.67\text{x}10^{10}\text{cm}\sqrt{Hz}/\text{W}$, nearly twice the blackbody radiation limit. Thermoelectric properties from Chapter 7 are used. The design parameters used as well as the simulated device parameters can be seen in Table 8.3. Any design parameter not mentioned in this table is unchanged from those laid out in the '1B' design in Chapter 3. Where the plate dimensions refers to the linear dimension of the optical absorber, pit dimension is the linear dimension of the etch pit defining the dimension of the entire device, t refers to film thicknesses, w refers to film widths, C is the thermal capacitance, G is the thermal conductance, τ is the thermal time constant, $\Re$ is the responsivity, and V refers to the various voltage noise sources.

Table 8.3: Design parameters for optimized device design.

Parameter	Value	Unit
Plate Dimension	200	μm
Pit Dimension	1100	μm
$t_{Al_2O_3}$	20	nm
$t_{Thermoelectric}$	350	nm
$w_{Al_2O_3}$	12	μm
$w_{Bi_2Te_3}$	2	μm
$w_{Sb_2Te_3}$	6	μm
C	2.74×10^{-8}	J/K
G	1.14×10^{-8}	W/K
τ	2.4	s
$\Re$	52600	V/W
$V_{Johnson}$	28.4	nV/$\sqrt{Hz}$
V_{TC}	4.0	nV/$\sqrt{Hz}$
V_{Total}	28.7	nV/$\sqrt{Hz}$
Detectivity	3.67×10^{10}	cm$\sqrt{Hz}$/W

Bibliography

[1] L.S. Rothman, D. Jacquemart, A. Barbe, D. Chris Benner, M. Birk, L.R. Brown, M.R. Carleer, C. Chackerian Jr., K. Chance, L.H. Coudert, V. Dana, V.M. Devi, J.-M. Flaud, R.R. Gamache, A. Goldman, J.-M. Hartmann, K.W. Jucks, A.G. Maki, J.-Y. Mandin, S.T. Massie, J. Orphal, A. Perrin, C.P. Rinsland, M.A.H. Smith, J. Tennyson, R.N. Tolchenov, R.A. Toth, J. Vander Auwera, P. Varanasi, and G. Wagner. The {HITRAN} 2004 molecular spectroscopic database. *Journal of Quantitative Spectroscopy and Radiative Transfer*, 96(2):139 – 204, 2005. ISSN 0022-4073. doi: 10.1016/j.jqsrt.2004.10.008. URL http://www.sciencedirect.com/science/article/pii/S0022407305001081.

[2] Paul G. Lucey, Keith A. Horton, and Tim Williams. Performance of a long-wave infrared hyperspectral imager using a sagnac interferometer and an uncooled microbolometer array. *Appl. Opt.*, 47(28):F107–F113, Oct 2008. doi: 10.1364/AO.47.00F107. URL http://ao.osa.org/abstract.cfm?URI=ao-47-28-F107.

[3] M. Fendler, D. Dumas, F. Chemla, M. Cohen, P. Laporte, K. Tekaya, E. Le Coarer, J. Primot, and H. Ribot. Hemispherical infrared focal plane arrays: a new design parameter for the instruments. pages 84531P–84531P–12, 2012. doi: 10.1117/12.925379. URL +http://dx.doi.org/10.1117/12.925379.

[4] Paul W. Kruse. Photon effects in hg$_{1-x}$cd$_x$te. *Appl. Opt.*, 4(6):687–692, Jun 1965. doi: 10.1364/AO.4.000687. URL http://ao.osa.org/abstract.cfm?URI=ao-4-6-687.

[5] Kaoru Yamashita, Akishi Murata, and Masanori Okuyama. Miniaturized infrared sensor using silicon diaphragm based on golay cell. *Sensors and Actuators A: Physical*, 66(13):29 – 32, 1998. ISSN 0924-4247. doi: 10.1016/S0924-4247(97)01702-0. URL http://www.sciencedirect.com/science/article/pii/S0924424797017020.

[6] R. Andrew Wood. Uncooled thermal imaging with monolithic silicon focal planes. pages 322–329, 1993. doi: 10.1117/12.160553. URL +http://dx.doi.org/10.1117/12.160553.

[7] R. A. Wood, C.J. Han, and P.W. Kruse. Integrated uncooled infrared detector imaging arrays. In *Solid-State Sensor and Actuator Workshop, 1992. 5th Technical Digest., IEEE*, pages 132–135, 1992. doi: 10.1109/SOLSEN.1992.228308.

[8] Chuan Li, George Skidmore, Christopher Howard, Elwood Clarke, and C. J. Han. Advancement in 17-micron pixel pitch uncooled focal plane arrays. pages 72980S–72980S–11, 2009. doi: 10.1117/12.818189. URL +http://dx.doi.org/10.1117/12.818189.

[9] William A. Radford, Richard Wyles, Jessica Wyles, John B. Varesi, Michael Ray, Daniel F. Murphy, Adam Kennedy, A. Finch, Edgar A. Moody, F. Cheung, R. Coda, and Stefan T. Baur. Microbolometer uncooled infrared camera with 20-mk netd. pages 636–646, 1998. doi: 10.1117/12.328064. URL +http://dx.doi.org/10.1117/12.328064.

[10] Charles M. Hanson, Sameer K. Ajmera, John Brady, Thomas Fagan, William McCardel, Diane Morgan, Tom Schimert, A. J. Syllaios, and Michael F. Taylor. <title>Small pixel a-si/a-SiGe bolometer focal plane array technology at l-3 communications</title>. pages 76600R–76600R–9, April 2010. doi: 10.1117/12.852511. URL http://spie.org/x648.html?product_id=852511.

[11] George D. Skidmore and Christopher G. Howard. Pixel structure having an umbrella type absorber with one or more recesses ..., November 2009. URL http://www.google.com/patents?id=IJfKAAAAEBAJ. U.S. Classification: 250/338.1.

[12] Seiji Kurashina and Shigeru Tohyama. Thermal-type infra-red ray solid-state image sensor and method of fabricating the same, October 2007. International Classification: G01T1/24; G01T1/00; H01L37/00; G01J5/20; G01J5/00; H01L27/14 U.S. Classification: G01J5/20.

[13] Toshio Kanno, Minoru Saga, Shouhei Matsumoto, Makoto Uchida, Nanao Tsukamoto, Akio Tanaka, Shigeyuki Itoh, Akihiro Nakazato, Tsutomu Endoh, Shigeru Tohyama, Yuuichi Yamamoto, Susumu Murashima, Nahoya Fujimoto, and Nobukazu Teranishi. Uncooled infrared focal plane array having 128 x 128 thermopile detector elements. pages 450–459, 1994. doi: 10.1117/12.188660. URL +http://dx.doi.org/10.1117/12.188660.

[14] Bodo FORG, Frank Herrmann, Wilhelm Leneke, Joerg Schieferdecker, Mischa Schulze, Marion Simon, and Karlheinz Storck. Thermopile infrared sensor by monolithic silicon micromachining, July 2011. International Classification: G01J5/08; G01J5/20 U.S. Classification: G01J 5/08; G01J 5/10; G01J 5/12; G01J 5/04; G01J 5/02.

[15] M.C. Foote, E.W. Jones, and T. Caillat. Uncooled thermopile infrared detector linear arrays with detectivity greater than 109 cmHz1/2/W. *IEEE Transactions on Electron Devices*, 45(9):1896–1902, 1998. ISSN 0018-9383. doi: 10.1109/16.711353.

[16] Frank Haenschke, Ernst Kessler, Ulrich Dillner, Andreas Ihring, Uwe Schinkel, and Hans-Georg Meyer. New high detectivity linear array for analytical measurement in the room temperature range. pages 83531L–83531L, May 2012. doi: 10.1117/12.919851. URL http://dx.doi.org/10.1117/12.919851.

[17] F. Vlklein, A. Wiegand, and V. Baier. High-sensitivity radiation thermopiles made of BiSbTe films. *Sensors and Actuators A: Physical*, 29(2):87–91, November 1991. ISSN 0924-4247. doi: 10.1016/0924-4247(91)87109-G. URL http://www.sciencedirect.com/science/article/pii/092442479187109G.

[18] M. Almasri, Bai Xu, and J. Castracane. Amorphous silicon two-color microbolometer for uncooled IR detection. *IEEE Sensors Journal*, 6(2):293–300, 2006. ISSN 1530-437X. doi: 10.1109/JSEN.2006.870139.

[19] D.S. Tezcan, S. Eminoglu, and T. Akin. A low-cost uncooled infrared microbolometer detector in standard CMOS technology. *IEEE Transactions on Electron Devices*, 50(2):494–502, 2003. ISSN 0018-9383. doi: 10.1109/TED.2002.807453.

[20] S. Sedky, P. Fiorini, K. Baert, L. Hermans, and Robert Mertens. Characterization and optimization of infrared poly SiGe bolometers. *IEEE Transactions on Electron Devices*, 46(4):675–682, 1999. ISSN 0018-9383. doi: 10.1109/16.753700.

[21] Sherif Sedky, Paolo Fiorini, Matty Caymax, Agnes Verbist, and Chris Baert. IR bolometers made of polycrystalline silicon germanium. *Sensors and Actuators A: Physical*, 66(13):193–199, April 1998. ISSN 0924-4247. doi: 10.1016/S0924-4247(98)00007-7. URL http://www.sciencedirect.com/science/article/pii/S0924424798000077.

[22] Pauline Renoux, Sigurdur gir Jnsson, Levente J. Klein, Hendrik F. Hamann, and Snorri Ingvarsson. Sub-wavelength bolometers: Uncooled platinum wires as infrared sensors. *Optics Express*, 19(9):8721–8727, April 2011. doi: 10.1364/OE.19.008721. URL http://www.opticsexpress.org/abstract.cfm?URI=oe-19-9-8721.

[23] Nobukazu Teranishi. Chapter 6 thermoelectric uncooled infrared focal plane arrays. In Paul W. Kruse and David D. Skatrud, editor, *Semiconductors and Semimetals*, volume Volume 47, pages 203–218. Elsevier, 1997. ISBN 0080-8784. URL http://www.sciencedirect.com/science/article/pii/S0080878408626927.

[24] HJ Goldsmid. Conversion efficiency and figure-of-merit. *CRC Handbook of Thermoelectrics*, pages 19–25, 1995.

[25] Shyh Wang. *Fundamentals of semiconductor theory and device physics.* Prentice Hall Englewood Cliffs, NJ, 1989.

[26] Donald A Neamen and Boris Pevzner. *Semiconductor physics and devices: basic principles*, volume 3. McGraw-Hill New York, 2003.

[27] B Zeghbroeck. *Principles of semiconductor devices and heterojunctions*, volume 25. Paperback-Nov, 2008.

[28] Hiroshi Julian Goldsmid and Bernard Lister Worsnop. *Applications of thermoelectricity*, volume 960. Methuen London, 1960.

[29] H. J. Goldsmid, A. R. Sheard, and D. A. Wright. The performance of bismuth telluride thermojunctions. *British Journal of Applied Physics*, 9(9):365, September 1958. ISSN 0508-3443. doi: 10.1088/0508-3443/9/9/306. URL http://iopscience.iop.org/0508-3443/9/9/306.

[30] Theodore S. Shilliday. Performance of composite peltier junctions of Bi2Te3. *Journal of Applied Physics*, 28(9):1035–1042, September 1957. ISSN 00218979. doi: doi:10.1063/1.1722903. URL http://jap.aip.org/resource/1/japiau/v28/i9/p1035_s1.

[31] SV Airapetyants and BA Efimova. Thermoeleetric properties and the nature of bonds in the system bi 2 te 3+ sb 2 te 3. *Zh. Tekh. Fiz.*, 28(8):1768–1774, 1958.

[32] S. K. Mishra, S. Satpathy, and O. Jepsen. Electronic structure and thermoelectric properties of bismuth telluride and bismuth selenide. *Journal of Physics: Condensed Matter*, 9(2):461, January 1997. ISSN 0953-8984. doi: 10.1088/0953-8984/9/2/014. URL http://iopscience.iop.org/0953-8984/9/2/014.

[33] G. Jeffrey Snyder and Eric S. Toberer. Complex thermoelectric materials. *Nature Materials*, 7(2):105–114, February 2008. ISSN 1476-1122. doi: 10.1038/nmat2090. URL http://www.nature.com/nmat/journal/v7/n2/full/nmat2090.html.

[34] AF Ioffe, SV Airapetyants, AV Ioffe, NV Kolomoets, and LS Stil'bans. On improving the efficiency of semiconductor thermoelements. In *Dokl. Akad. Nauk SSSR*, volume 106, page 981, 1956.

[35] D. A. Wright. Thermoelectric properties of bismuth telluride and its alloys. *Nature*, 181(4612):834–834, March 1958. doi: 10.1038/181834a0. URL http://www.nature.com/nature/journal/v181/n4612/abs/181834a0.html.

[36] H.J. Goldsmid and A.W. Penn. Boundary scattering of phonons in solid solutions. *Physics Letters A*, 27(8):523–524, September 1968. ISSN 0375-9601. doi: 10.1016/

0375-9601(68)90898-0. URL http://www.sciencedirect.com/science/article/pii/0375960168908980.

[37] T. Caillat, M. Carle, P. Pierrat, H. Scherrer, and S. Scherrer. Thermoelectric properties of (BixSb1x)2Te3 single crystal solid solutions grown by the T.H.M. method. *Journal of Physics and Chemistry of Solids*, 53(8):1121–1129, August 1992. ISSN 0022-3697. doi: 10.1016/0022-3697(92)90087-T. URL http://www.sciencedirect.com/science/article/pii/002236979290087T.

[38] H. Noro, K. Sato, and H. Kagechika. The thermoelectric properties and crystallography of BiSbTeSe thin films grown by ion beam sputtering. *Journal of Applied Physics*, 73(3):1252–1260, February 1993. ISSN 00218979. doi: doi:10.1063/1.353266. URL http://jap.aip.org/resource/1/japiau/v73/i3/p1252_s1.

[39] J. P Fleurial, A. Borshchevsky, T. Caillat, and R. Ewell. New materials and devices for thermoelectric applications. In *Energy Conversion Engineering Conference, 1997. IECEC-97., Proceedings of the 32nd Intersociety*, pages 1080–1085 vol.2, 1997. doi: 10.1109/IECEC.1997.661920.

[40] B. C. Sales, D. Mandrus, and R. K. Williams. Filled skutterudite antimonides: A new class of thermoelectric materials. *Science*, 272(5266):1325–1328, May 1996. ISSN 0036-8075, 1095-9203. doi: 10.1126/science.272.5266.1325. URL http://www.sciencemag.org/content/272/5266/1325. PMID: 8662465.

[41] Ctirad Uher. Skutterudites: prospective novel thermoelectrics. *Semiconductors and semimetals*, 69:139–253, 2001.

[42] Rama Venkatasubramanian, Edward Siivola, Thomas Colpitts, and Brooks O'Quinn. Thin-film thermoelectric devices with high room-temperature figures of merit. *Nature*, 413(6856):597–602, October 2001. ISSN 0028-0836. doi: 10.1038/35098012. URL http://dx.doi.org/10.1038/35098012.

[43] L. D. Hicks and M. S. Dresselhaus. Effect of quantum-well structures on the thermoelectric figure of merit. *Phys. Rev. B*, 47:12727–12731, May 1993. doi: 10.1103/PhysRevB.47.12727. URL http://link.aps.org/doi/10.1103/PhysRevB.47.12727.

[44] D. Dragoman and M. Dragoman. Giant thermoelectric effect in graphene. *Applied Physics Letters*, 91(20):203116–203116–3, November 2007. ISSN 00036951. doi: doi:10.1063/1.2814080. URL http://apl.aip.org/resource/1/applab/v91/i20/p203116_s1.

[45] Su-Kyum Lim, Min-Young Kim, and Tae-Sung Oh. Thermoelectric properties of the bismuthantimonytelluride and the antimonytelluride films processed by electrodeposition for micro-device applications. *Thin Solid Films*, 517(14):4199 – 4203, 2009. ISSN 0040-6090. doi: 10.1016/j.tsf.2009.02.005. URL http://www.sciencedirect.com/science/article/pii/S0040609009002685. ¡ce:title¿The proceedings of the 1st International Conference on Microelectronics and Plasma Technology (ICMAP 2008)¡/ce:title¿.

[46] A Giani, A Boulouz, B Aboulfarah, F Pascal-Delannoy, A Foucaran, A Boyer, and A Mzerd. Effect of antimony concentration on the electrical and thermoelectrical properties of (bi1xsbx)2te3 thin films grown by metal organic chemical vapour deposition (mocvd) technique. *Journal of Crystal Growth*, 204(12): 91 – 96, 1999. ISSN 0022-0248. doi: 10.1016/S0022-0248(99)00159-1. URL http://www.sciencedirect.com/science/article/pii/S0022024899001591.

[47] Hu Huang, Wei ling Luan, and Shan tung Tu. Influence of annealing on thermoelectric properties of bismuth telluride films grown via radio frequency magnetron sputtering. *Thin Solid Films*, 517(13):3731 – 3734, 2009. ISSN 0040-6090. doi: 10.1016/j.tsf.2009.01.015. URL http://www.sciencedirect.com/science/article/pii/S0040609009000054.

[48] Helin Zou, DM Rowe, and Gao Min. Preparation and characterization of p-type sbte and n-type bite thin films grown by coevaporation. *Journal of Vacuum Science & Technology A: Vacuum, Surfaces, and Films*, 19:899, 2001.

[49] A. Gross, G. Hwang, B. Huang, H. Yang, N. Ghafouri, H. Kim, C. Uher, M. Kaviany, and K. Najafi. High-performance micro scale thermoelectric cooler: An optimized 6-stage cooler. In *Solid-State Sensors, Actuators and Microsystems Conference, 2009. TRANSDUCERS 2009. International*, pages 2413–2416, 2009. doi: 10.1109/SENSOR.2009.5285431.

[50] Min-Young Kim and Tae-Sung Oh. Electrodeposition and thermoelectric characteristics of Bi2Te3 and Sb2Te3 films for thermopile sensor applications. *Journal of Electronic Materials*, 38(7):1176–1181, July 2009. ISSN 0361-5235, 1543-186X. doi: 10.1007/s11664-008-0653-7. URL http://link.springer.com/article/10.1007/s11664-008-0653-7.

[51] Paul W Kruse, Laurence D McGlauchlin, and Richmond B McQuistan. Elements of infrared technology: Generation, transmission and detection. *New York: Wiley, 1962*, 1, 1962.

[52] RA Wood. Monolithic silicon microbolometer arrays. *Semiconductors and semimetals*, 47:43–121d, 1997.

[53] P. L. Richards. Bolometers for infrared and millimeter waves. *Journal of Applied Physics*, 76(1):1–24, July 1994. ISSN 00218979. doi: doi:10.1063/1.357128. URL http://jap.aip.org/resource/1/japiau/v76/i1/p1_s1.

[54] Joseph J. Talghader, Anand S. Gawarikar, and Ryan P. Shea. Spectral selectivity in infrared thermal detection. *Light: Science & Applications*, 1(8):e24, 2012. ISSN false. doi: 10.1038/lsa.2012.24. URL http://www.nature.com/lsa/journal/v1/n8/abs/lsa201224a.html.

[55] Ryan P. Shea, Anand S. Gawarikar, and Joseph J. Talghader. High-performance sputtered thermoelectric junctions for micromechanical devices. In *Solid-State Sensors, Actuators and Microsystems Conference, 2012.*, pages 258–261, 2012.

[56] Nicholas T. Gabriel and J.J. Talghader. Thermal conductivity and refractive index of hafnia-alumina nanolaminates. *Journal of Applied Physics*, 110(4):043526–043526–8, 2011. ISSN 0021-8979. doi: 10.1063/1.3626462.

[57] Pochi Yeh. *Optical waves in layered media*, volume 95. Wiley New York, 1988.

[58] Edward D Palik. *Handbook of Optical Constants of Solids: Index*, volume 3. Academic press, 1998.

[59] Aleksandar D. Rakic, Aleksandra B. Djurišic, Jovan M. Elazar, and Marian L. Majewski. Optical properties of metallic films for vertical-cavity optoelectronic devices. *Appl. Opt.*, 37(22):5271–5283, Aug 1998. doi: 10.1364/AO.37.005271. URL http://ao.osa.org/abstract.cfm?URI=ao-37-22-5271.

[60] David R Lide and Thomas J Bruno. *CRC handbook of chemistry and physics*. CRC PressI Llc, 2012.

[61] Ryan P. Shea, Anand S. Gawarikar, and Joseph J. Talghader. Midwave thermal infrared detection using semiconductor selective absorption. *Opt. Express*, 18(22):22833–22841, Oct 2010. doi: 10.1364/OE.18.022833. URL http://www.opticsexpress.org/abstract.cfm?URI=oe-18-22-22833.

[62] R. CLARK JONES. The ultimate sensitivity of radiation detectors. *J. Opt. Soc. Am.*, 37(11):879–888, Nov 1947. doi: 10.1364/JOSA.37.000879. URL http://www.opticsinfobase.org/abstract.cfm?URI=josa-37-11-879.

[63] P. B. FELLGETT. On the ultimate sensitivity and practical performance of radiation detectors. *J. Opt. Soc. Am.*, 39(11):970–976, Nov 1949. doi: 10.1364/JOSA.39.000970. URL http://www.opticsinfobase.org/abstract.cfm?URI=josa-39-11-970.

[64] Larry J Hornbeck. Infrared detector, June 4 1991. US Patent 5,021,663.

[65] R Andrew Wood. Use of vanadium oxide in microbolometer sensors, March 14 2000. US Patent RE36,615.

[66] K. M. van Vliet. Noise limitations in solid state photodetectors. *Appl. Opt.*, 6 (7):1145–1169, Jul 1967. doi: 10.1364/AO.6.001145. URL http://ao.osa.org/abstract.cfm?URI=ao-6-7-1145.

[67] A. Muoz, J. Melndez, M.C. Torquemada, M.T. Rodrigo, J. Cebrin, A.J. de Castro, J. Meneses, M. Ugarte, F. Lpez, G. Vergara, J.L. Hernndez, J.M. Martn, L. Adell, and M.T. Montojo. Pbse photodetector arrays for {IR} sensors. *Thin Solid Films*, 317(12):425 – 428, 1998. ISSN 0040-6090. doi: 10.1016/S0040-6090(97)00576-2. URL http://www.sciencedirect.com/science/article/pii/S0040609097005762.

[68] Jaime M. Martin, Jose Luis Hernndez, Luca Adell, Acacio Rodriguez, and F. Lpez. Arrays of thermally evaporated PbSe infrared photodetectors deposited on si substrates operating at room temperature. *Semiconductor Science and Technology*, 11 (11):1740, November 1996. ISSN 0268-1242. doi: 10.1088/0268-1242/11/11/017. URL http://iopscience.iop.org/0268-1242/11/11/017.

[69] Christopher L Kauffman, Sung-Shik Yoo, Timothy R Beystrum, et al. Photoconductive bolometer infrared detector, August 28 2007. US Patent 7,262,413.

[70] Anand S Gawarikar, Ryan P Shea, Alexandre Mehdaoui, and Joseph J Talghader. Radiation heat transfer dominated microbolometers. In *Optical MEMs and Nanophotonics, 2008 IEEE/LEOS Internationall Conference on*, pages 178–179. IEEE, 2008.

[71] Yu-Wei Jiang, Lawrence D. Tzuang, Yi-Han Ye, Yi-Ting Wu, Ming-Wei Tsai, Chia-Yi Chen, and Si-Chen Lee. Effect of wood's anomalies on the profile of extraordinary transmission spectra through metal periodic arrays of rectangular subwavelength holes with different aspect ratio. *Opt. Express*, 17(4):2631–2637, Feb 2009. doi: 10.1364/OE.17.002631. URL http://www.opticsexpress.org/abstract.cfm?URI=oe-17-4-2631.

[72] Aleksandar D. Rakic, Aleksandra B. Djurišic, Jovan M. Elazar, and Marian L. Majewski. Optical properties of metallic films for vertical-cavity optoelectronic devices. *Appl. Opt.*, 37(22):5271–5283, Aug 1998. doi: 10.1364/AO.37.005271. URL http://ao.osa.org/abstract.cfm?URI=ao-37-22-5271.

[73] Ryan P. Shea, Anand S. Gawarikar, and Joseph J. Talghader. Impact of thermal radiation on the performance of ultrasmall microcoolers. *Journal of Electronic*

Materials, pages 1–7. ISSN 0361-5235, 1543-186X. doi: 10.1007/s11664-012-2453-3. URL http://link.springer.com/article/10.1007/s11664-012-2453-3.

[74] Gao Min and D.M. Rowe. Cooling performance of integrated thermoelectric microcooler. *Solid-State Electronics*, 43(5):923–929, May 1999. ISSN 0038-1101. doi: 10.1016/S0038-1101(99)00045-3. URL http://www.sciencedirect.com/science/article/pii/S0038110199000453.

[75] Luciana W. da Silva and Massoud Kaviany. Micro-thermoelectric cooler: interfacial effects on thermal and electrical transport. *International Journal of Heat and Mass Transfer*, 47(1011):2417 – 2435, 2004. ISSN 0017-9310. doi: 10.1016/j.ijheatmasstransfer.2003.11.024. URL http://www.sciencedirect.com/science/article/pii/S0017931003006574.

[76] G.S. Hwang, A.J. Gross, H. Kim, S.W. Lee, N. Ghafouri, B.L. Huang, C. Lawrence, C. Uher, K. Najafi, and M. Kaviany. Micro thermoelectric cooler: Planar multistage. *International Journal of Heat and Mass Transfer*, 52(78):1843–1852, March 2009. ISSN 0017-9310. doi: 10.1016/j.ijheatmasstransfer.2008.10.014. URL http://www.sciencedirect.com/science/article/pii/S0017931008005930.

[77] Da-Jeng Yao, Gang Chen, and Chang-Jin Kim. Design and analysis of an inplane thermoelectric microcooler. *Nanoscale and Microscale Thermophysical Engineering*, 14(2):95–109, 2010. doi: 10.1080/15567265.2010.484008. URL http://www.tandfonline.com/doi/abs/10.1080/15567265.2010.484008.

[78] Luciana W. da Silva, Massoud Kaviany, and Mehdi Asheghi. Measured performance of a micro thermoelectric cooler. pages 415–422, January 2004. doi: 10.1115/HT-FED2004-56412. URL http://dx.doi.org/10.1115/HT-FED2004-56412.

[79] L.M. Goncalves, C. Couto, P. Alpuim, D.M. Rowe, and J.H. Correia. Thermoelectric microstructures of bi2te3/sb2te3 for a self-calibrated micro-pyrometer. *Sensors and Actuators A: Physical*, 130131(0):346 – 351, 2006. ISSN 0924-4247. doi: 10.1016/j.sna.2005.10.014. URL http://www.sciencedirect.com/science/article/pii/S0924424705005753. ¡ce:title¿Selected Papers from {TRANSDUCERS} '05¡/ce:title¿ ¡ce:subtitle¿The 13th International Conference on Solid-State Sensors, Actuators and Microsystems - Seoul, Korea, 5-9 June 2005¡/ce:subtitle¿.

[80] S.-M. Lee, David G. Cahill, and Thomas H. Allen. Thermal conductivity of sputtered oxide films. *Phys. Rev. B*, 52:253–257, Jul 1995. doi: 10.1103/PhysRevB.52.253. URL http://link.aps.org/doi/10.1103/PhysRevB.52.253.

[81] Bed Poudel, Qing Hao, Yi Ma, Yucheng Lan, Austin Minnich, Bo Yu, Xiao Yan, Dezhi Wang, Andrew Muto, Daryoosh Vashaee, Xiaoyuan Chen, Junming Liu, Mildred S. Dresselhaus, Gang Chen, and Zhifeng Ren. High-thermoelectric performance of nanostructured bismuth antimony telluride bulk alloys. *Science*, 320(5876):634–638, 2008. doi: 10.1126/science.1156446. URL http://www.sciencemag.org/content/320/5876/634.abstract.

[82] Helin Zou, D.M. Rowe, and S.G.K. Williams. Peltier effect in a co-evaporated sb2te3(p)-bi2te3(n) thin film thermocouple. *Thin Solid Films*, 408(12):270 – 274, 2002. ISSN 0040-6090. doi: 10.1016/S0040-6090(02)00077-9. URL http://www.sciencedirect.com/science/article/pii/S0040609002000779.

[83] L. M. Goncalves, J. G. Rocha, C. Couto, P. Alpuim, Gao Min, D. M. Rowe, and J. H. Correia. Fabrication of flexible thermoelectric microcoolers using planar thin-film technologies. *Journal of Micromechanics and Microengineering*, 17(7):S168, July 2007. ISSN 0960-1317. doi: 10.1088/0960-1317/17/7/S14. URL http://iopscience.iop.org/0960-1317/17/7/S14.

[84] Z.H. Zheng, P. Fan, T.B. Chen, Z.K. Cai, P.J. Liu, G.X. Liang, D.P. Zhang, and X.M. Cai. Optimization in fabricating bismuth telluride thin films by ion beam sputtering deposition. *Thin Solid Films*, 520(16):5245–5248, June 2012. ISSN 0040-6090. doi: 10.1016/j.tsf.2012.03.086. URL http://www.sciencedirect.com/science/article/pii/S0040609012003732.

[85] Fan Ping, Zheng Zhuang-Hao, Liang Guang-Xing, Cai Xing-Min, and Zhang Dong-Ping. Composition-dependent characterization of Sb2Te3 thin films prepared by ion beam sputtering deposition. *Chinese Physics Letters*, 27(8):087201, August 2010. ISSN 0256-307X. doi: 10.1088/0256-307X/27/8/087201. URL http://iopscience.iop.org/0256-307X/27/8/087201.

[86] H Scherrer and S Scherrer. Bismuth telluride, antimony telluride, and their solid solutions. crc handbook of thermoelectrics; rowe, dm, ed, 1995.

[87] Anand S Gawarikar. Spectrally selective high detectivity uncooled detectors for the long wave infrared, Publication Forthcoming.